

**EXPERIMENTAL INVESTIGATION AND MODELING
OF THE ELECTROSTRICTIVE RELAXOR FERROELECTRIC
LEAD MAGNESIUM NIOBATE-LEAD TITANATE**

by

Chettoor G. Namboodri, Jr.

Thesis submitted to the Faculty of the
Virginia Polytechnic Institute and State University
in partial fulfillment of the requirements for the degree of
Master of Science
in
Mechanical Engineering

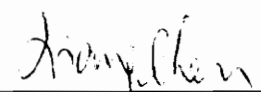
APPROVED:



Dr. Craig A. Rogers, Chair



Dr. Harry H. Robertshaw



Dr. Chen Liang

November, 1992

Blacksburg, Virginia

C.2

LD
5655
V855
1992
N362
C.2

Experimental Investigation and Modeling of the Electrostrictive Relaxor Ferroelectric Lead Magnesium Niobate-Lead Titanate

by

Chettoor G. Namboodri, Jr.

Committee Chair: Dr. Craig A. Rogers

Mechanical Engineering

Abstract

Fundamental to the design of intelligent material systems and structures are the realization of attributes of the constitutive transducer materials—the sensors and actuators—and the ability to model the characteristics of these transducers. In this thesis, electromechanical behaviors of the electrostrictive relaxor ferroelectric lead magnesium niobate-lead titanate (PMN-PT) are experimentally characterized and phenomenologically modeled. The dependencies of PMN-PT electromechanical transduction on temperature and frequency, characteristics of relaxor ferroelectrics, and on applied direct-current electric field, an attribute of electrostrictors which enables tunable transduction sensitivities, are investigated and modeled with respect to electrical, sensing, and actuation properties. A general procedure for using the developed constitutive models to quantitatively describe the behavior of PMN-PT is introduced for sensing and for the three types of actuation—servo, on/off, and alternating current.

Contents

| | |
|---|-----------|
| Chapter 1 Introduction and Literature Review | 1 |
| 1.1 Introduction | 1 |
| 1.2 Intelligent Material Systems and Structures | 6 |
| 1.3 Applications of PMN-PT | 9 |
| 1.4 Introduction to PMN-PT | 17 |
| 1.4.1 History | 17 |
| 1.4.2 Structure and Relaxor Ferroelectricity | 18 |
| 1.4.3 Dielectric Behavior | 26 |
| 1.4.4 Electrostrictive Responses | 38 |
| 1.5 Review of Constitutive Modeling for PMN-PT | 45 |
| 1.5.1 Landau-Ginzburg-Devonshire Thermodynamic Phenomenology for Electrostriction | 47 |
| 1.5.2 A Phenomenological Formulation for Ferroelectricity | 49 |
| 1.5.3 Compositional Variation and Grain Size Models for Relaxor Ferroelectric Behavior | 51 |
| 1.6 Summary | 58 |
| Chapter 2 Experimental Design and Procedure | 60 |
| 2.1 PMN-PT Specimen History | 60 |

| | | |
|------------------|--|------------|
| 2.2 | Actuation Property Experiments | 61 |
| 2.2 | Sensing Property Experiments | 69 |
| 2.3 | Dielectric Property Investigations | 75 |
| 2.4 | Grain Size Studies | 77 |
| Chapter 3 | Experimental Results and Discussion | 78 |
| 3.1 | Dielectric Results | 78 |
| 3.2 | Actuation Results | 82 |
| 3.3 | Sensing Results | 94 |
| 3.4 | Grain Size Results | 98 |
| Chapter 4 | Analysis and Modeling | 102 |
| 4.1 | Grain Size and Phase-dependent Dielectric Behavior | 102 |
| 4.2 | Frequency Dispersion of Dielectric Properties | 108 |
| 4.3 | Bias Field Considerations | 112 |
| 4.4 | Electrostrictive Coefficient Relations | 116 |
| 4.5 | Dielectric and Actuator Transduction Responses | 117 |
| 4.6 | Sensor Transduction Response | 131 |
| 4.7 | Summary: A Constitutive Model for PMN-PT | 134 |
| 4.7.1 | Sensing with PMN-PT | 134 |
| 4.7.2 | Servo Actuation with PMN-PT | 135 |
| 4.7.3 | DC Dielectric Susceptibility | 135 |

| | |
|---|-----|
| 4.7.4 AC Dielectric Susceptibility | 135 |
| 4.7.5 Dynamic Actuation with PMN-PT | 137 |
| Chapter 5 Conclusions and Recommendations | 138 |
| Glossary | 142 |
| References | 146 |
| Vita | 152 |

List of Figures

| | | |
|-------------|---|----|
| Figure 1.1 | Typical bimorph bending configuration with electrostrictive plates . . . | 10 |
| Figure 1.2 | (a) Design of a PMN-based deformable mirror and (b) example interferometric pattern results for such a mirror | 12 |
| Figure 1.3 | Typical electroceramic, linear-displacement stack actuator | 13 |
| Figure 1.4 | (a) Design of an electroceramic printer head and (b) PMN-based magnification mechanism used to control each wire | 14 |
| Figure 1.5 | Experimental apparatus for testing pulse-echo medical probe, composed of a PMN-PT/polyurethane composite | 16 |
| Figure 1.6 | Classes of crystalline materials based on symmetry and polar behavior | 20 |
| Figure 1.7 | Characteristic features of a relaxor ferroelectric: (a) dielectric dispersion in PMN as a function of temperature and frequency and (b) dielectric hysteresis of PMN as a function of temperature | 22 |
| Figure 1.8 | Weak-field (1.5 kV/m, 1 kHz) dielectric response of the ferroelectric barium titanate (BaTiO ₃) ceramic | 23 |
| Figure 1.9 | Unit cell of a simple perovskite | 25 |
| Figure 1.10 | Various polarization processes | 27 |
| Figure 1.11 | A parallel-plate capacitor filled with a dielectric medium | 28 |
| Figure 1.12 | Complex capacitive components of the total current | 31 |

| | |
|---|----|
| Figure 1.13 Dielectric response of PMN-PT at various frequencies through the ferroelectric-paraelectric phase transition | 34 |
| Figure 1.14 Spontaneous polarization of PMN-PT through its ferroelectric-paraelectric phase transition | 35 |
| Figure 1.15 Weak-field relative permittivity of PMN-PT with respect to applied DC electric field at various frequencies | 37 |
| Figure 1.16 Hydrostatic pressure dependence of the reciprocal permittivity of PMN at various temperatures | 39 |
| Figure 1.17 Grain size effects on the relative permittivity and permittivity ratio of PMN through its phase transition | 40 |
| Figure 1.18 (a) Field-induced transverse strain of PMN-PT versus the square of electric polarization and (b) transverse strain in PMN-PT and a typical PZT under slowly varying electric fields | 42 |
| Figure 1.19 Cartesian directions and physical origins of electrostrictive coefficients in a cubic perovskite | 43 |
| Figure 1.20 Electrostrictive coefficients for PMN-PT, for an electric field amplitude of 190 V/cm at 400 Hz, as a function of temperature | 44 |
| Figure 1.21 Field-amplitude dependence of electrostrictive coefficient parallel to applied field and effective relative permittivity for PMN-PT at (a) 25°C, (b) 42.5°C, (c) 87.5°C and (d) 108.5°C at 200 Hz | 46 |
| Figure 1.22 Hyperbolic tangent model fits of typical hysteresis loops for polycrystalline electrostrictive ceramics of (a) PMN, (b) 0.9PMN-0.1PT, | |

| | |
|---|----|
| (c) 0.93PMN-0.07PT and (d) $\text{La}_{0.01}[\text{0.93PMN-0.07PT}]_{0.99}$ | 50 |
| Figure 1.23 Temperature of the dielectric maximum as a function of the measurement frequency | 57 |
| Figure 2.1 Strain-gage technique for observing the transverse direct electrostrictive effect in PMN-PT. | 63 |
| Figure 2.2 Experimental apparatus for (a) static and (b) dynamic measurement of the transverse direct electrostrictive effect with PMN-PT. | 65 |
| Figure 2.3 Strain-gage technique for observing transverse electrostrictive sensing properties of PMN-PT with respect to applied bias field. | 70 |
| Figure 2.4 Experimental apparatus for measurement of transverse electrostrictive sensing properties of PMN-PT. | 72 |
| Figure 3.1 Dielectric results versus temperature for various frequencies | 80 |
| Figure 3.2 Dielectric frequency responses at various temperatures | 81 |
| Figure 3.3 Actuator transduction sensitivity versus temperature for various frequencies | 84 |
| Figure 3.4 Frequency response of actuator transduction sensitivity for various temperatures at constant bias field | 86 |
| Figure 3.5 Frequency response of actuator transduction sensitivity for various bias fields at constant temperature | 87 |
| Figure 3.6 Actuator transduction sensitivity versus bias field for various frequencies at constant temperature | 89 |
| Figure 3.7 Actuator transduction sensitivity versus bias field for various | |

| | |
|--|-----|
| temperatures at constant frequency | 91 |
| Figure 3.8 Actuator transduction sensitivity versus temperature for various bias fields at constant frequency | 92 |
| Figure 3.9 Free-induced strain resulting from the application of DC electric fields at various temperatures | 93 |
| Figure 3.10 Frequency response of sensor transduction sensitivity at various temperatures | 95 |
| Figure 3.11 Sensor transduction sensitivity versus bias field for various frequencies | 96 |
| Figure 3.12 SEM micrograph of fractured PMN-PT surface | 99 |
| Figure 4.1 Comparison of models with 0.93PMN-0.07PT data for (a) Curie maximum temperatures and (b) maximum permittivities versus grain size and for (c) Shroul's diffuseness coefficient versus maximum permittivity | 105 |
| Figure 4.2 Comparison of Shroul's dielectric phase transition model with experimental data | 107 |
| Figure 4.3 Comparison of frequency-dispersive, dielectric phase transition model with experimental data | 111 |
| Figure 4.4 Comparison of hyperbolic tangent polarization model with DC free- induced strain experimental data | 115 |
| Figure 4.5 Comparison of DC relative susceptibility model results with reduced data from DC free-induced strain response experiments versus | |

| | |
|---|-----|
| temperature | 119 |
| Figure 4.6 Comparison of AC relative susceptibility model results with reduced data from permittivity response experiments versus temperature at various frequencies | 121 |
| Figure 4.7 Comparison of electrostrictive constitutive model results with data from AC actuator response experiments versus temperature at various frequencies | 122 |
| Figure 4.8 Comparison of AC relative susceptibility model results with reduced data from permittivity response experiments versus frequency at various bias fields | 124 |
| Figure 4.9 Comparison of electrostrictive constitutive model results with data from AC actuator response experiments versus frequency at various bias fields | 125 |
| Figure 4.10 Comparison of DC relative susceptibility model results with reduced data from DC free-induced strain response experiments versus bias field . | 127 |
| Figure 4.11 Comparison of AC relative susceptibility model results with reduced data from permittivity response experiments versus bias field at various temperatures | 128 |
| Figure 4.12 Comparison of electrostrictive constitutive model results with data from AC actuator response experiments versus bias field at various temperatures | 130 |
| Figure 4.13 Comparison of electrostrictive constitutive model results with data | |

from AC sensor response experiments versus frequency at various bias
fields 133

List of Tables

Table 1.1 Experimental processing results for 0.93PMN-0.07PT 54

Table 2.1 Specifications for PMN-PT transverse actuation experiments 67

Table 2.2 Text matrix for PMN-PT transverse actuation experiments 68

Table 2.3 Specifications for PMN-PT transverse sensing experiments 73

Table 2.4 Text matrix for PMN-PT transverse sensing experiments 74

Table 2.5 Text matrix for PMN-PT dielectric experiments 76

Table 3.1 Macro compositional effects on some properties of PMN-PT fired at
1300°C 101

Nomenclature

| | |
|-----------------|---|
| A | Surface area of a parallel-plate capacitor electrode (m^2) |
| a | Representative dimension for cubic perovskite cell |
| C | Capacitance of a parallel-plate capacitor (F) |
| C_0 | Capacitance of free space for a parallel-plate geometry (F) |
| c | Constant for Viehland's susceptibility loss model scaling variable |
| D | Dielectric displacement vector (C/m^2) |
| d | Piezoelectric strain coefficient, for actuation (m/V) |
| d^o | Electrostrictive piezoelectric strain coefficient (m/V) |
| E, \mathbf{E} | Electric field, vector (V/m) |
| E_{AC} | Dynamic (AC) contribution to electric field (V/m) |
| E_{DC} | Static (DC) contribution to electric field (V/m) |
| E^c | Coercivity electric field (V/m) |
| δE | Incremental electric field (V/m) |
| F | Gibb's free energy density (J/m^3) |
| f_D | Debye frequency (Hz) |
| g | Piezoelectric voltage coefficient, for sensing ($\text{V}\cdot\text{m}/\text{N}$) |
| g^o | Electrostrictive piezoelectric voltage coefficient ($\text{V}\cdot\text{m}/\text{N}$) |
| h | Thickness of a dielectric in a parallel-plate capacitor (m) |
| I, \mathbf{I} | Current, vector (A) |

| | |
|-----------------|--|
| j | Complex identity, $\sqrt{-1}$ |
| L_i | Maximum permittivity-diffuseness model coefficients (K) |
| k, k' | Constants in hyperbolic tangent polarization model (m/V) |
| k_i | Polarization model temperature coefficients (m/V-K ⁱ) |
| k_{VF} | Constant in Vogel-Fulcher relations |
| P, \mathbf{P} | Polarization, vector (C/m ²) |
| P | Saturation polarization (C/m ²) |
| Q | Electrostrictive coefficients (m ⁴ /C ²) |
| Q_T | Total charge along a parallel-plate capacitor electrode (C) |
| q | Electrostrictive frequency model coefficient (m ⁴ /C ²) |
| R | Dynamic coefficient in the spin-glass susceptibility loss model |
| r | Frozen coefficient in the spin-glass susceptibility loss model |
| s | Applied mechanical strain (m/m) |
| T | Temperature (°C, K) |
| T_C | Curie temperature, ferroelectric transition to paraelectric phase (°C, K) |
| T_f | Vogel-Fulcher freezing temperature for relaxor ferroelectrics (°C, K) |
| T_{max} | Curie temperature of a relaxor ferroelectric, temperature of maximum permittivity in the ferroelectric-paraelectric phase transition (°C, K) |
| t | Time (sec) |
| U, \mathbf{U} | Electric potential or voltage, vector (V) |
| U_o | Amplitude of a sinusoidal voltage (V) |
| u | Scaling variable in the spin-glass susceptibility loss model |

| | |
|-----------|---|
| W | Curie-Weiss constant |
| X | Susceptibility temperature-frequency model coefficient |
| X_{AC} | Susceptibility paraelectric temperature-frequency model coefficient |
| X_E | Susceptibility temperature-frequency-bias model coefficient (V/m) |
| X_i | Susceptibility grain-size model coefficients (μm^{-1}) |
| X_{max} | Maximum susceptibility temperature-frequency model coefficient |
| Y | Young's modulus of elasticity (N/m^2) |

Greek

| | |
|--------------------------------|--|
| α | Activation energy for Vogel-Fulcher relations (eV) |
| β | Reciprocal dielectric susceptibility |
| γ | Grain size number (μm) |
| $\tan\delta$ | Electric permittivity ratio, dielectric loss, dissipation factor |
| ϵ' | Relative electric permittivity |
| ϵ'' | Relative electric permittivity loss |
| ϵ^* | Complex relative permittivity |
| ϵ_C, κ_C | Relative permittivity at Curie temperature |
| ϵ_m, κ_m | Integral mean relative permittivity for relaxor phase transition |
| $\epsilon_{max}, \kappa_{max}$ | Maximum relative permittivity of ferroelectrics |
| ϵ_o | Electric permittivity of free space, 8.85×10^{-12} F/m |
| ζ | Cutoff energy for spin-glass model relations (eV) |
| Θ_C | Curie-Weiss temperature ($^{\circ}\text{C}$, K) |

| | |
|--------------|---|
| κ | Dielectric constant, same as relative electric permittivity |
| Λ | Free-induced strain (m/m) |
| λ | Level of diffuseness of relaxor phase transition ($^{\circ}\text{C}$, K) |
| ρ | Density (g/cm^3) |
| σ | Applied mechanical stress (N/m^2) |
| σ^P | Polarization charge density of a dielectric between parallel plates (C/m^2) |
| σ^T | Total charge density along electrodes of a parallel-plate capacitor (C/m^2) |
| τ_i | Maximum Curie temperature-grain size model coefficients ($\text{K}/\mu\text{m}^i$) |
| τ_{max} | Maximum Curie temperature-frequency model coefficient ($^{\circ}\text{C}$, K) |
| χ | Relative dielectric susceptibility |
| χ'' | Relative dielectric susceptibility loss |
| χ_m | Integral mean relative susceptibility for relaxor phase transition |
| χ_{max} | Maximum relative susceptibility of ferroelectrics |
| ω | Frequency (Hz) |

Chapter 1

Introduction and Literature Review

1.1 Introduction

In the past decade, interest in electroceramic transducers has been renewed by the conceptual advent of intelligent material systems and structures. Intelligent, or smart, material systems and structures are designed, via control capabilities and architected mechanics, to autonomously and judiciously sense and respond to their environments using transducer materials, i.e., sensors and actuators. Much progress has been made in the development of applications with electroceramic transducers and their integration into these systems; consequently, the need for appropriate mechanical characterization and useful, quantitative constitutive modeling for design applications has arisen.

Although electronic ceramics comprise a tremendous variety of sensors and actuators, the most common and pertinent to intelligent material systems and structures are those containing an electromechanical relationship. Application of these electroceramics are found in the areas of mechanical transduction, vibration, and acoustics. Piezoelectric and electrostrictive materials are used almost exclusively in these fields. Although piezoelectric ceramics have received more attention, the development of electroceramics, such as the lead magnesium niobate systems, over the past decade has led to increased

interest in electrostrictors for electromechanical transduction.

Lead magnesium niobate doped with lead titanate ($\text{Pb}[\text{Mg}_{1/3}\text{Nb}_{2/3}]\text{O}_3\text{-PbTiO}_3$, or PMN-PT) is a ceramic which exhibits a strong electrostrictive effect. Electrostriction involves a nonlinear electromechanical coupling for which the material develops a strain proportional to the square of the polarization. Polarization in a dielectric is induced by the alignment of dipoles with an applied electric field. Free-induced strains in PMN-PT as high as $4\text{-}5 \times 10^{-4}$ have been achieved for realizable fields on the order of 10^3 V/mm (Ealey and Davis, 1990). For comparison, a piezoceramic develops strain *proportional* to the electric-field-induced polarization. Strain levels for the best piezoelectrics are comparable to the best electrostrictors (Damjanovic and Newnham, 1992). When compared with a typical piezoceramic such as lead zirconate titanate ($\text{Pb}[\text{ZrTi}]\text{O}_3$, or PZT), PMN-PT distinguishes itself not only in the nonlinearity of its coupling but also in its electromechanical and thermal stability, its negligible dielectric aging, its repeatability under cyclic driving fields, and its dynamic response (Cieminski and Beige, 1991; Cross et al., 1980).

The advantageous characteristic of an anhysteretic, nonlinear electromechanical coupling with PMN-PT has been used to develop transducers with tunable sensitivities (Newnham and Ruschau, 1991). Because the slope of the repeatable electric field-to-strain relationship varies, the transduction sensitivity, whether the ceramic is used as an actuator or sensor, can be controlled by adjusting the DC bias electric field about which

the electrostrictive transducer operates. The capability for tunable transduction, i.e., adjustable sensitivity, differentiates PMN-PT from typical electroceramic transducers like PZT, whose electromechanical coupling coefficients are fixed, and enables a 'learning' capacity, where the property coefficients can be altered in response to the environment.

A description of the advantages of PMN-PT, however, would be remiss without relating its disadvantages, especially considering materials research, since investigation of disadvantages can lead through processing and synthesis to significant improvements or to new materials and applications. Because the response of PMN-PT is nonlinear, quadratic with respect to polarization, the useful actuator authority for AC applications is limited. Furthermore, the electromechanical response is highly frequency-dependent and is restricted to a temperature range in which the dielectric permittivity is large. Finally, deformation for low applied electric fields is small (quadratic behavior), so that electrostrictors such as PMN-PT somewhat exacerbate the desire for low-voltage devices.

Although much research into the constitutive behavior of PMN-PT has been reported, emphasis has been placed on material processing and dielectric behavior, due to attractive high permittivity values. The bridge of understanding from processing, composition, and dielectric properties to the mechanical domain has been qualitatively described and at best phenomenologically formulated. The electromechanical response of PMN-PT requires thorough investigation from an engineering perspective and sound, practical constitutive modeling for use in design and integration into intelligent material systems and

structures. Macroscopic models for electrostriction are derived from thermodynamic phenomenology based on Landau-Ginzburg-Devonshire (LGD) theory (Grindlay, 1970). These models describe the behavior of PMN-PT adequately; however, their utility in engineering design is curtailed by the nonlinearity and multi-parameter polarization relations of relaxor ferroelectrics. Zhang and Rogers (1992) recently introduced an intriguing macroscopic formulation for ferroelectricity, based on phenomenological relations for polarization reversal, and for piezoelectricity, based on thermodynamic relations for the material equations of state and statistical relations for state properties. Aspects of this model show promise for use in engineering design and can be readily applied to the description of PMN systems.

Microscopic models for polar behavior fundamentally contribute to material science and understanding but prove difficult to translate into engineering design. Such models are introduced in this manuscript to lend credence to empirical constitutive relations derived from the experimentation herein described and, in some occurrences, are supported for direct use in engineering design. In the case of PMN-PT and its class of materials, there has been much interest in the effect of submicroscopic compositional fluctuations on the dielectric behavior as the material passes through a broad thermal phase transition, pertinent since it incorporates the useful temperature range for electrostrictors such as PMN-PT. The effect of compositional fluctuations was qualitatively introduced by Smolenskii (1961), statistically modeled by Rolov (1965), and qualitatively refined by the superparaelectric model proposed by Cross (1987). The superparaelectric

model—analogue to the superparamagnetic state of small, unstable ordered spin clusters in magnetism, as evidenced by nanoscale short-range chemical ordering (Hilton et al., 1990)—has further been used to describe the frequency-dependent behavior of this class of materials (Viehland et al., 1990, 1991a, and 1991b). Grain size has been shown to affect primarily the magnitude of the permittivity during the broad, frequency dispersive phase transition (Swartz et al., 1984; Papet et al., 1990). Both a grain boundary model (Shrout et al., 1987) and a microdomain perturbation model, based on the superparaelectric theory, have been used to relate this phenomenon.

The objectives of this research are to characterize and model the electromechanical behaviors of PMN-PT, with an emphasis on engineering design utility. Investigations of the electrostrictive properties of PMN-PT have been performed with respect to temperature, frequency, and DC electric field. Experimentation with this electroceramic has included macroscopic mechanical studies of the material as both a sensor and an actuator and investigations into its dielectric behavior. Furthermore, grain size and compositional studies have been correlated with previously reported findings. These investigations, LGD phenomenology, and formulations similar to those introduced by Zhang and Rogers lead to a constitutive model with empirical embellishments for the electrostrictive behavior of PMN-PT. These empirical relations are based on qualitative microscopic theory and results.

In this chapter, the electrostrictive lead magnesium niobate-lead titanate is first described

within the perspective of intelligent material systems, and examples of its application are introduced. Next, the development of PMN-PT is recounted historically, its behavior is related to the class of electroceramic materials known as relaxor ferroelectrics, and its dielectric and electrostrictive properties are discussed. Finally, a review of constitutive modeling related to PMN-PT is provided.

1.2 Intelligent Material Systems and Structures

Typically, intelligent material systems have evolved from humankind's efforts to create more efficient, less massive kinetic designs. Not surprisingly, this evolution parallels and draws from biological systems, both in organization and components. For example, intelligent material systems used for structural control can readily be compared to the most complex and adaptive organism known, human beings. Like our muscles, they have distributed actuators to impart motion; like our nervous systems, distributed sensors for feedback information; like our brains, adaptive controllers such as artificial neural networks to coordinate feedback and motion; and like our skeletons, host structures to provide support and to contain and enhance implementation of the other components (Rogers and Stein, 1992).

Since intelligent material systems require interaction between and integration of sensors, actuators, structures, and controllers, understanding the individual, interdependent behavior of each of these constituents is vital for their effective use together. Among intelligent material system components are the transducers, the actuators and sensors.

Such transducers include piezoelectrics, electrostrictors, magnetostrictors, fiber optics, shape memory alloys, and electrorheological fluids. Fundamental to the study of these materials are the innate phenomena that enable them to be utilized.

For example, with piezoelectrics and electrostrictors, the electromechanical couplings of PMN-PT and PZT provide a useful means of transforming energy. In this case, an electric field applied across parallel-plate electrodes on the ceramics can induce strain in many tensor directions. A reciprocal effect, in which a dynamically strained electroceramic generates a corresponding electric field also occurs. With shape memory alloys, like Nitinol—a nickel-titanium alloy, a plastically strained specimen undergoes a phase transformation from martensite to austenite, during which it recovers its original shape or induces stress if restrained. Another useful effect, in which the elastic modulus for Nitinol increases by as much as 300%, occurs during the phase transformation. With magnetostrictors such as rare-earth ferrous alloys, strain is induced with magnetic field.

In the analogy to man, these phenomena parallel our many types of sensors—employed for visual, audio, olfactory, tactual, and epithelial feedback about our environments—and emulate our muscles—used for reaction to our environments. Within the field of intelligent material systems and structures, electroceramics comprise a collective majority of materials having been and currently under development. Electroceramic hydrophones used for underwater surveillance are similar in mechanism to the way in which fish sense vibrations and are analogous to our ears and our sense of touch (Newnham and Ruschau,

1991). Electroceramic actuators used for AC and on/off applications such as vibration controllers and micro motors mimic our fast-twitch muscles, while those used for DC servo applications like precision micropositioners imitate our slow-twitch muscles. Solid state electro-chemical sensors, such as zinc-oxide for humidity detection and tin-oxide for oxygen-deprived chemical species detection, simulate our senses of smell and taste (Newnham and Ruschau, 1991).

Among the many types of electroceramics, those which display an electromechanical coupling, typically piezoceramics and electrostrictors, currently dominate research and development efforts in areas of structural vibration, positioning, and deformation control pertinent to intelligent material systems. Biological analogies aside, these electroceramics have been used for active vibration control systems for structures in outer-space and for electrically-controlled automobile suspension systems (Newnham and Ruschau, 1991). They have been applied for structural positioning and deformation in recording device heads, precision tooling equipment, and adaptive optic systems.

As previously insinuated in the introduction of this chapter, the recent development of PMN-PT and related materials has alerted scientists and engineers to new possibilities with electrostrictive materials. The ability to adjust the electromechanical coupling coefficients by varying applied DC voltage has defined a class of *adaptive* transducers. Although this capability has not yet been widely utilized in practice, other features of PMN-PT have been exploited for many applications.

1.3 Applications of PMN-PT

Electrostrictive transducers such as PMN-PT have been used in three major capacities—servo, on/off, and AC—for applications ranging in industries from medicine to optics to manufacturing to computing to consumer products (Uchino, 1986). Servo and on/off applications harness the stable, anhysteretic, and repeatable responses of PMN-PT actuators. AC applications utilize the fast response time and the high, tunable sensitivity for both sensing and actuation. Three examples of each of these three types of applications are provided below.

In the optical communications industry, PMN-PT has been used to control the shape of so-called deformable mirrors, which can be used, for example, to correct a telescope image for distortions (Uchino, 1986). By deforming to a desired contour, the phase of incoming light waves can be appropriately compensated. In this application, the servo capabilities of PMN-PT are utilized through a bimorph-type configuration. Typical bimorph bending with electrostrictive plates is demonstrated in Figure 1.1.

As one PMN monomorph (thin electroceramic plate) tries to contract when an electric field is applied across its opposite electrodes, the other is inactive. Analogous to a thermally-activated bi-metal device, the force imbalance induced about the composite's neutral axis creates a bending moment, which can cause deformation of a bonded substrate, in this case, the mirror. For opposite bending, the other monomorph is activated. By incorporating multi-stacks of bimorphs, more degrees-of-freedom in the

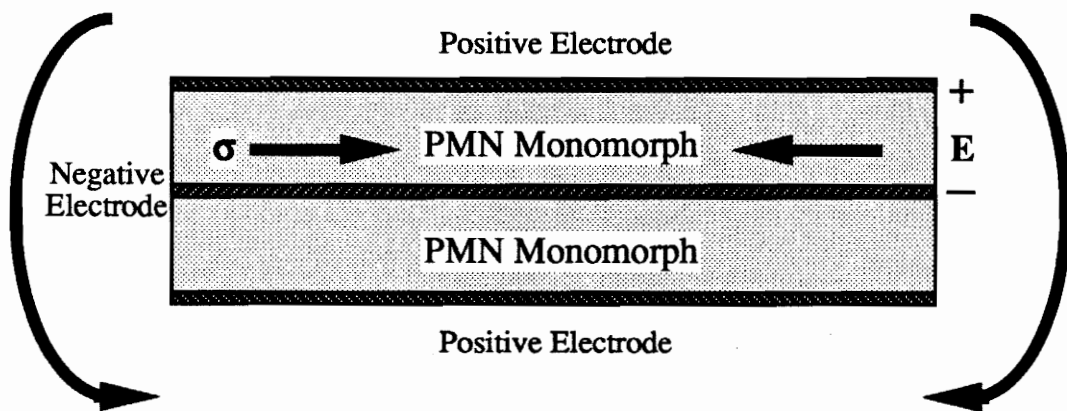
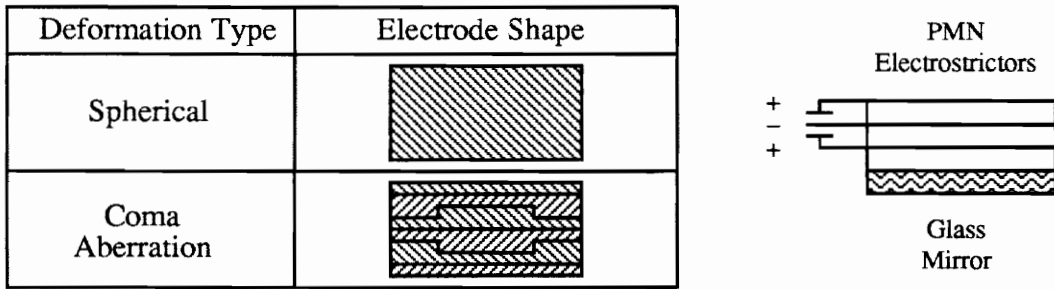


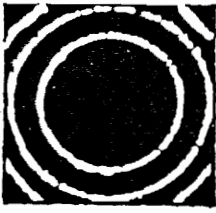
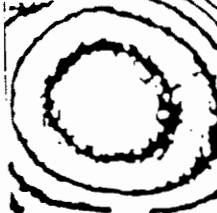




Figure 1.1 Typical bimorph bending configuration with electrostrictive plates (after Galvagni and Duprè, 1990).

deformation of the mirror along the surface of contact can be achieved. By patterning electrodes and thus designing the distribution of applied electric field, these degrees-of-freedom can be put to specific use. For example, as shown in Figure 1.2 (a), a uniform electrode pattern is used for spherical bending, or refocusing, and a 'six-divided pattern' is used for coma aberration correction, analogous to astigmatism correction in optometry. Results for such a configuration are demonstrated in Figure 1.2 (b), where desired and experimental interferometric fringe patterns generated by such a deformable mirror are displayed.

An on/off example for PMN-PT usage is evident in the computing industry, specifically for impact dot matrix printing (Uchino, 1986). In this application, PMN-PT is used in a stack configuration, as schematically described in Figure 1.3. In this geometry, an electrostrictive effect parallel to the direction of applied field is utilized; whereas, in the bimorph configuration, mechanical strain induced transverse to the direction of applied field is employed. Figures 1.4 (a) and (b) show the mechanism by which the PMN-PT on/off stack actuator operates the wire guides to impact the ribbon. With dot matrix printing, a seven-wire array, as in Figure 1.4 (a), is used to create 7x6-dot characters. The linear displacement of a stack actuator is amplified by the magnification mechanism of Figure 1.4 (b) to control each wire. Advantages over conventional electromagnetic actuators include an order-of-magnitude higher printing speeds, an order-of-magnitude lower energy consumption, and reduced noise emissions.



(a)

| Aberration | Interferogram of Desired Wavefront | Interferogram of Generated Wavefront |
|---------------------|---|--|
| Refocusing |  |  |
| Coma |  |  |
| Refocusing and Coma |  |  |

(b)

Figure 1.2 (a) Design of a PMN-based deformable mirror and (b) example interferometric pattern results for such a mirror (after Uchino, 1986).

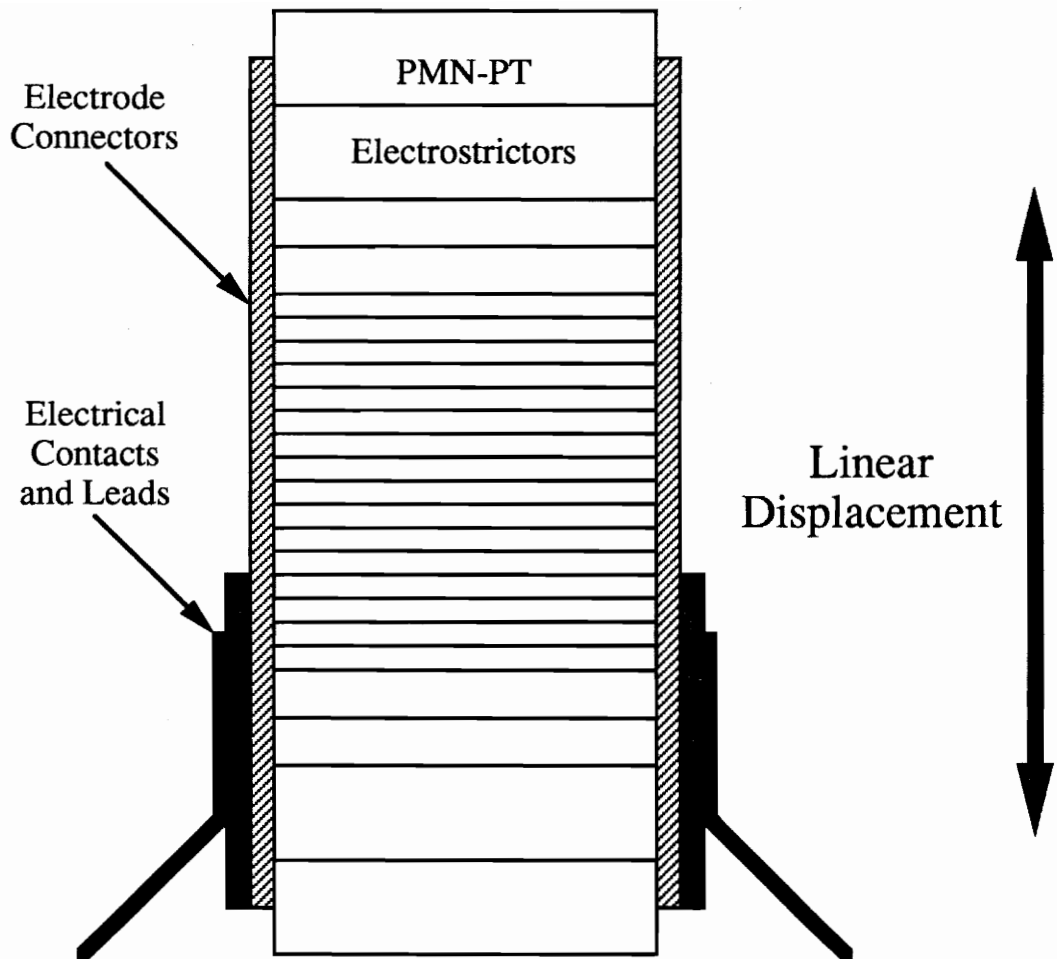
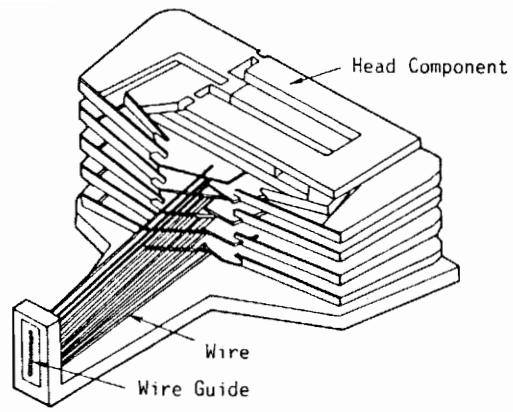
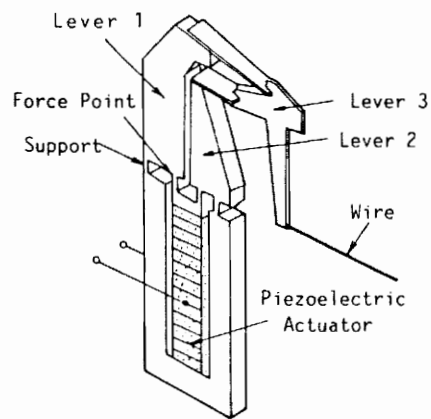


Figure 1.3 Typical electroceramic, linear-displacement stack actuator (after Galvagni and Duprè, 1990).



(a)



(b)

Figure 1.4 (a) Design of an electroceramic printer head and (b) PMN-based magnification mechanism used to control each wire (after Uchino, 1986).

A final example of a PMN-PT application really demonstrates the capabilities of this ceramic to both actuate and sense at high frequency (AC) and its adaptive capacity to adjust property coefficients and extend its applicability. Linear and phased array acoustic imaging systems are widely used in medicine; however, previously used transducers have had fixed electromechanical coupling, or electro-acoustic conversion efficiency. In this case, a tunable ultrasonic medical probe composed of an array of electrostrictors embedded in a polymer has been developed (Takeuchi et al., 1989).

As demonstrated in Figure 1.5, the array is capable of transmitting a pulse into an acoustic medium, and the reflection of this ultrasonic pulse from a subject of interest can be measured. A composite array is used for mechanical flexibility and toughness of the transducer. This technology is similar to the pulse-echo interrogation employed in submarine defense. The intriguing property of the PMN-PT medical probe is that by adjusting the DC bias voltage applied to the electrostrictors, the sensitivity of the probe can be adjusted. By taking advantage of DC-bias-controlled sensitivity, a PMN-based transducer with variable electro-acoustic efficiency can be used for both shallow and deep region diagnoses.

The three types of applications pertinent to PMN-PT transducers—servo and on/off actuation and AC actuation and sensing—require complete understanding and practical modeling for intelligent engineering design. The restrictions imposed by the limited temperature range associated with maximum electrostrictive response affect selection of

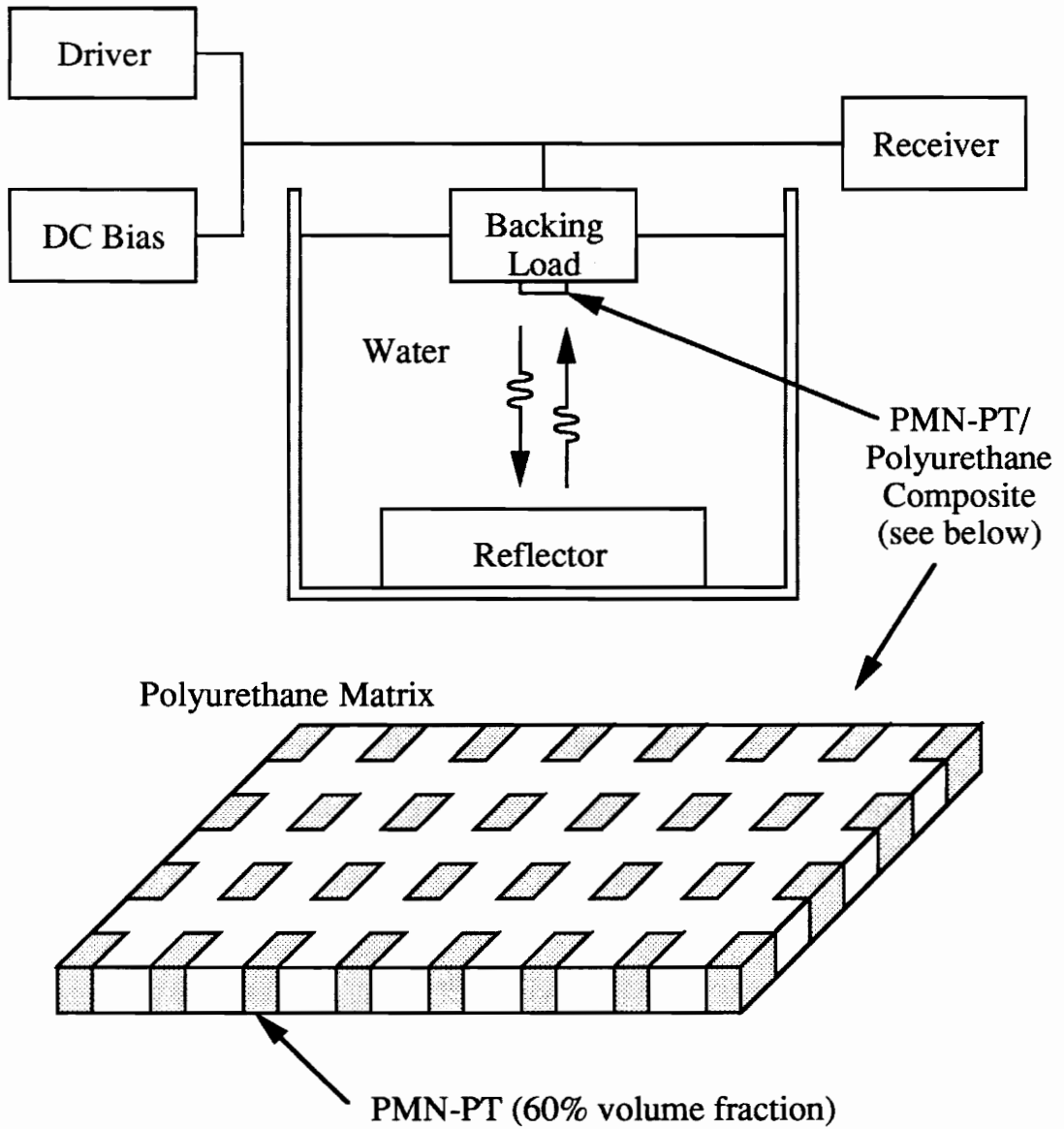


Figure 1.5 Experimental apparatus for testing pulse-echo medical probe, composed of a PMN-PT/polyurethane composite (after Takeuchi, 1989).

this transducer in smart material system design. For AC applications, the frequency response of PMN-PT is of utmost importance. The effects of bias field on electromechanical impedance can and have been exploited, but all of these characteristics need thorough investigation and quantitative constitutive relations. However, to understand the bases of these behaviors and to rationally model them for use in mechanical engineering design, we must first explore their affiliation to material sciences.

1.4 Introduction to PMN-PT

This introduction first provides a brief history of PMN-PT within the general context of electroceramics and then proceeds to relate its material characteristics to the class of electroceramics known as relaxor ferroelectrics. Within the framework of relaxor ferroelectrics, the dielectric attributes and their relation to chemical properties are addressed. Finally, electrostrictive behavior of the relaxor ferroelectric PMN-PT is discussed.

1.4.1 History

Lead magnesium niobate was introduced in 1957 by Soviet Ceramist G.A. Smolenskii (Smolenskii and Agranovskaya, 1959). By the 1950's, interest in high-permittivity dielectrics had peaked with the development of transistors and integrated circuits, requiring higher capacitance and smaller size dielectrics (Moulson and Herbert, 1990). Earlier, in the 1940's, the emergence of barium titanate had begun to meet these needs, and its discovery led to a flurry of researchers investigating newer and better dielectrics.

Concurrently, there was much interest in the piezoelectric properties of these materials. By the late 1940's, it was realized that high-permittivity and large piezoelectric effects were largely attributable to the *ferroelectric* character of barium titanate—likewise shared by other titanates, niobates, and tantalates of similar (perovskite) structure.

Smolenskii (1959) thus proposed and undertook a systematic investigation of such compounds, proceeding from those of simpler composition to more complex solid solutions. Compounds of complex composition mean those in which ions of different types occur in the same sublattice of the crystalline structure, e.g. $\text{Pb}[\text{Mg}_{1/3}\text{Nb}_{2/3}]\text{O}_3$. Although Smolenskii did not specifically investigate the PMN-PT compound, he laid the foundation for its development in the late 1970's. By the early 1980's, the large electrostrictive effect demonstrated by this high permittivity material was being utilized in such servo actuating capacities as the deformable mirror (Ealey and Davis, 1990).

1.4.2 Structure and Relaxor Ferroelectricity

Smolenskii's contributions encompassed not only the foundation for the development of PMN-PT but also a microscopic basis for describing the material behavior (Smolenskii et al., 1961). He suggested that the so-called 'degeneracy' of ferroelectric properties and diffuseness of the important phase transition from ferroelectricity to paraelectricity are caused by compositional fluctuations arising from a random distribution of cations in the sublattice and by departures from such a distribution into 'ion aggregates.' He further proposed that the relaxation polarization, for which the spontaneous polarization slowly

becomes zero during the phase transition, relates to motion of a boundary between stable and metastable domains. This diffuse phase transition has come to be known as the *relaxor phase transition*, and the type of ceramics exhibiting such behavior are called relaxor ferroelectrics. Smolenskii's contributions serve as an introduction to the material and to the terminology associated with characteristics of the ceramic PMN-PT.

Although the evolution from pottery to electronic components has broadened the meaning of ceramics in some cases to all inorganic, nonmetallic materials, an accepted, more confining definition includes polycrystalline, nonmetallic materials that obtain mechanical strength through firing or sintering (Moulson and Herbert, 1990). Crystalline materials may be categorized by their structural symmetry, as in Figure 1.6. Of the thirty-two crystalline symmetry point groups, or classes of single crystal materials, eleven have centrosymmetric structure, possess a center of symmetry, and are non-polar. Among the remaining twenty-one noncentrosymmetric groups, twenty are *piezoelectric*, meaning electric dipoles are directionally polarized under an applied stress. For the nonpolar, centrosymmetric crystals, applied stress results in symmetrical ionic displacements, so that there is no net change in dipole moment, thus no net charge.

Ten piezoelectric point groups are *pyroelectric*, spontaneously (thermally) polarized to reveal a preferred alignment of dipoles (Moulson and Herbert, 1990). By far, the most actively researched, developed, and applied class of electroceramics in the areas of mechanical transduction, vibrations, and acoustics belong to a subgroup of pyroelectrics

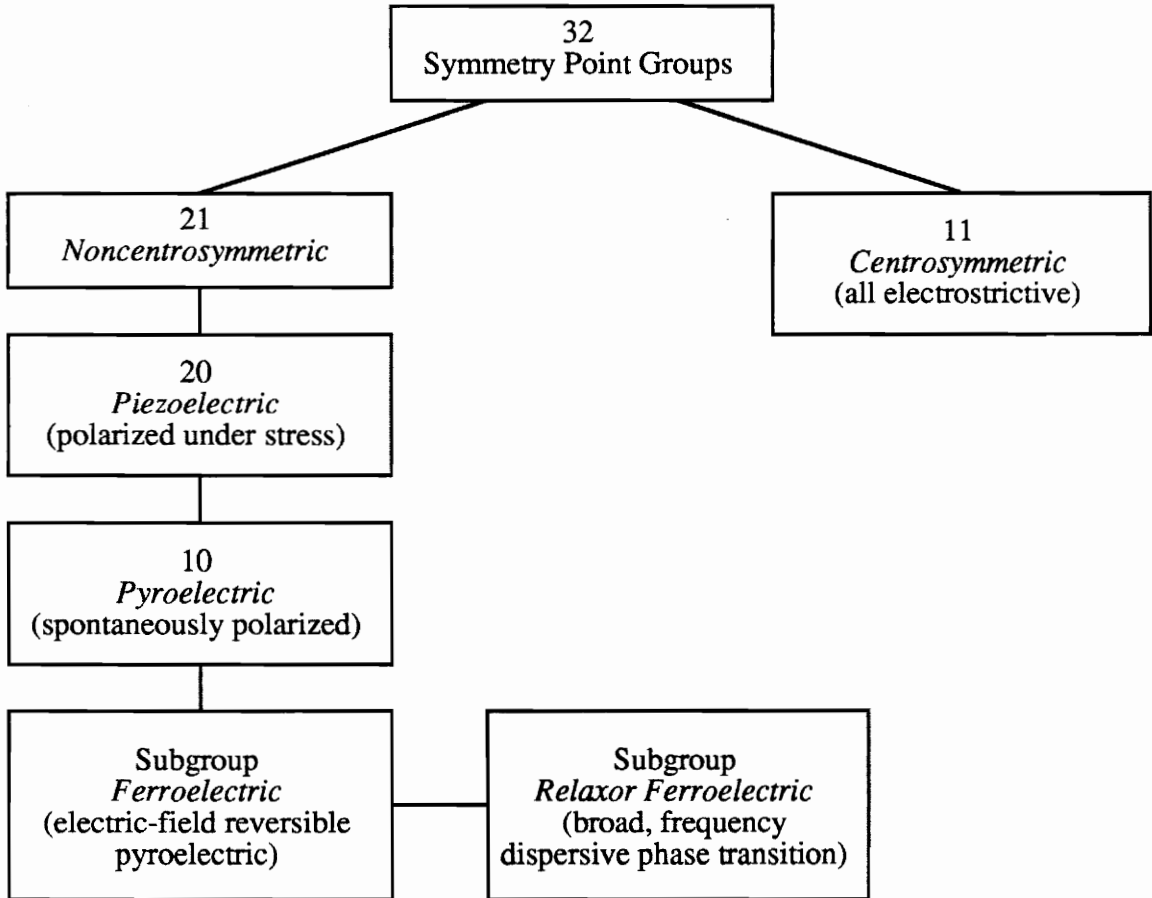


Figure 1.6 Classes of crystalline materials based on symmetry and polar behavior (after Haertling, 1986).

called *ferroelectrics*, which are dielectrics whose spontaneous polarization can be reversed in the presence of an electric field. Ferroelectrics, such as lead zirconate titanate (PZT), which can be permanently polarized (poled) by a strong electric field under appropriate thermal and temporal conditions are the most commonly used piezoelectrics. If crystallites of a polycrystalline ceramic belong to a piezoelectric class, such as the ferroelectrics, and if their polar axes can be appropriately aligned as described above, then a piezoelectric ceramic is feasible.

Relaxors are a type of ferroelectric distinguished by two characteristics featured in Figure 1.7, which indicates the behavior of PMN, described by Cross (1987) as a ‘typical relaxor composition.’ One property, illustrated in Figure 1.7 (a), is that although the weak-field relative dielectric permittivity, ϵ' (proportional to its capacitance as later described), reaches a maximum at a point corresponding to the ferroelectric Curie temperature, T_C , this dielectric maximum does not distinctly mark a phase change, since the T_{\max} varies with frequency. This strong frequency dispersion is also manifest in the dielectric loss, termed $\tan \delta$ in Figure 1.7 (a).

A second property distinguishing relaxors from normal ferroelectrics, namely the diffuse phase transition, is actually evident in both Figures 1.7 (a) and (b). In Figure 1.7 (a) the diffuseness is most apparent when compared to a typical ferroelectric response, as in Figure 1.8 for the prototypic ferroelectric, BaTiO_3 . Similarly, the polarization behavior in high alternating fields clearly shows that PMN is ferroelectric at temperatures much

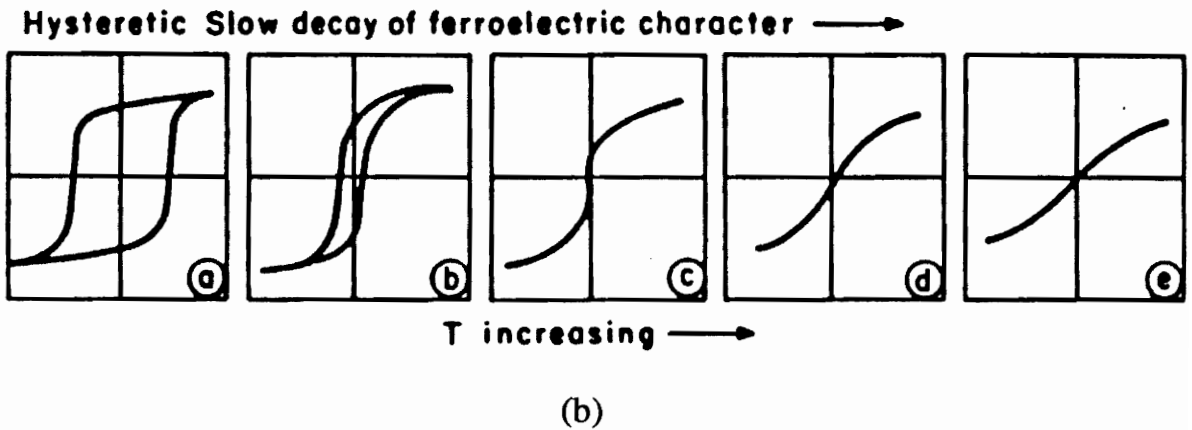
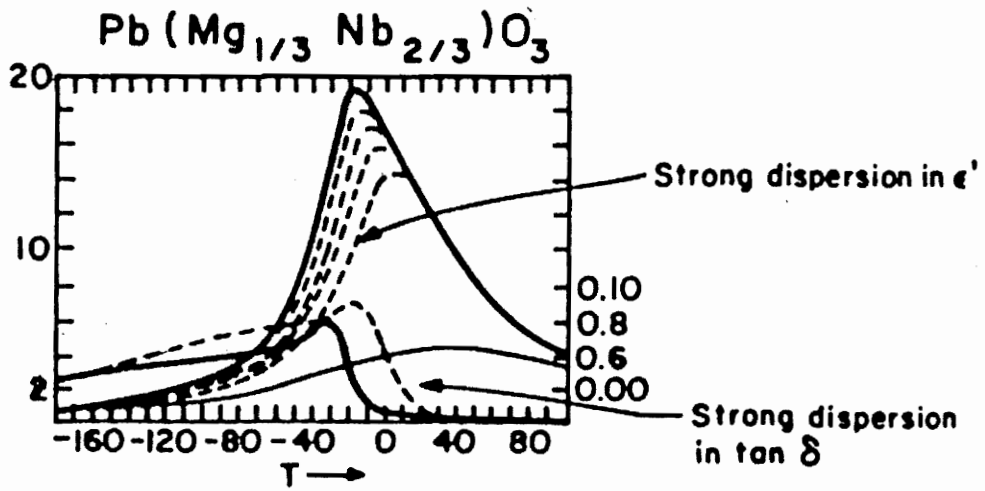


Figure 1.7 Characteristic features of a relaxor ferroelectric: (a) dielectric dispersion in PMN as a function of temperature and frequency and (b) dielectric hysteresis of PMN as a function of temperature (after Cross, 1987).

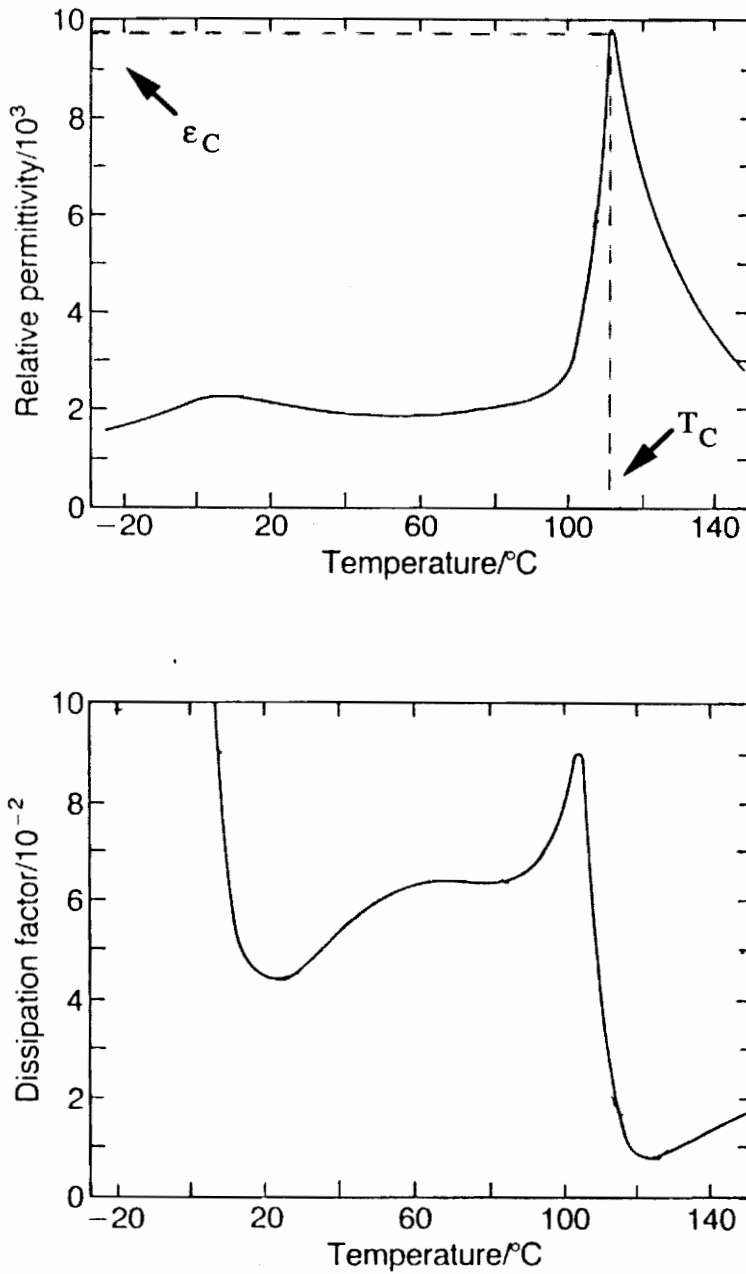


Figure 1.8 Weak-field (1.5 kV/m, 1 kHz) dielectric response of the ferroelectric barium titanate (BaTiO_3) ceramic (after Moulson and Herbert, 1990).

lower than the T_{max} ; however, unlike PZT or BaTiO₃, the hysteretic response slowly degenerates into simply a nonlinearity as the temperature increases. This hysteresis is associated with spontaneous polarization, which for normal ferroelectrics is suddenly lost at T_C with the onset of the paraelectric phase. Instead, the spontaneous polarization of relaxors gradually decays to zero as the paraelectric phase is introduced with increased temperatures. Furthermore, as an aside, electrostrictive relaxors do not exhibit dielectric aging pertinent to normal ferroelectrics, since they are not permanently polarized for transduction application (Pan et al., 1986).

The structure of PMN-PT is a solid solution of complex and simple perovskites. A solid solution refers to a stoichiometric mixture of solid phases. Perovskite is a crystalline symmetry typical of ferroelectric materials (Haertling, 1986). A simple perovskite, characteristic of ceramics having composition ABO₃, like PbTiO₃ (PT), is illustrated in Figure 1.9. For complex perovskites, such as Pb[Mg_{1/3}Nb_{2/3}] (PMN), the composition is classified as A(B'B'')O₃, and differs from that of Figure 1.9 in that B-site locations vary in the type of cation. The structure of PMN-PT is introduced here so that a better understanding of the models which describe dielectric behavior based on compositional fluctuations and grain size may be attained. In summary, PMN-PT is a relaxor ferroelectric—a piezoelectric whose spontaneous polarization can be redirected by the application of electric field and whose phase transition to a paraelectric state is both broad and frequency dispersive—which is a solid solution of perovskite ceramic phases.

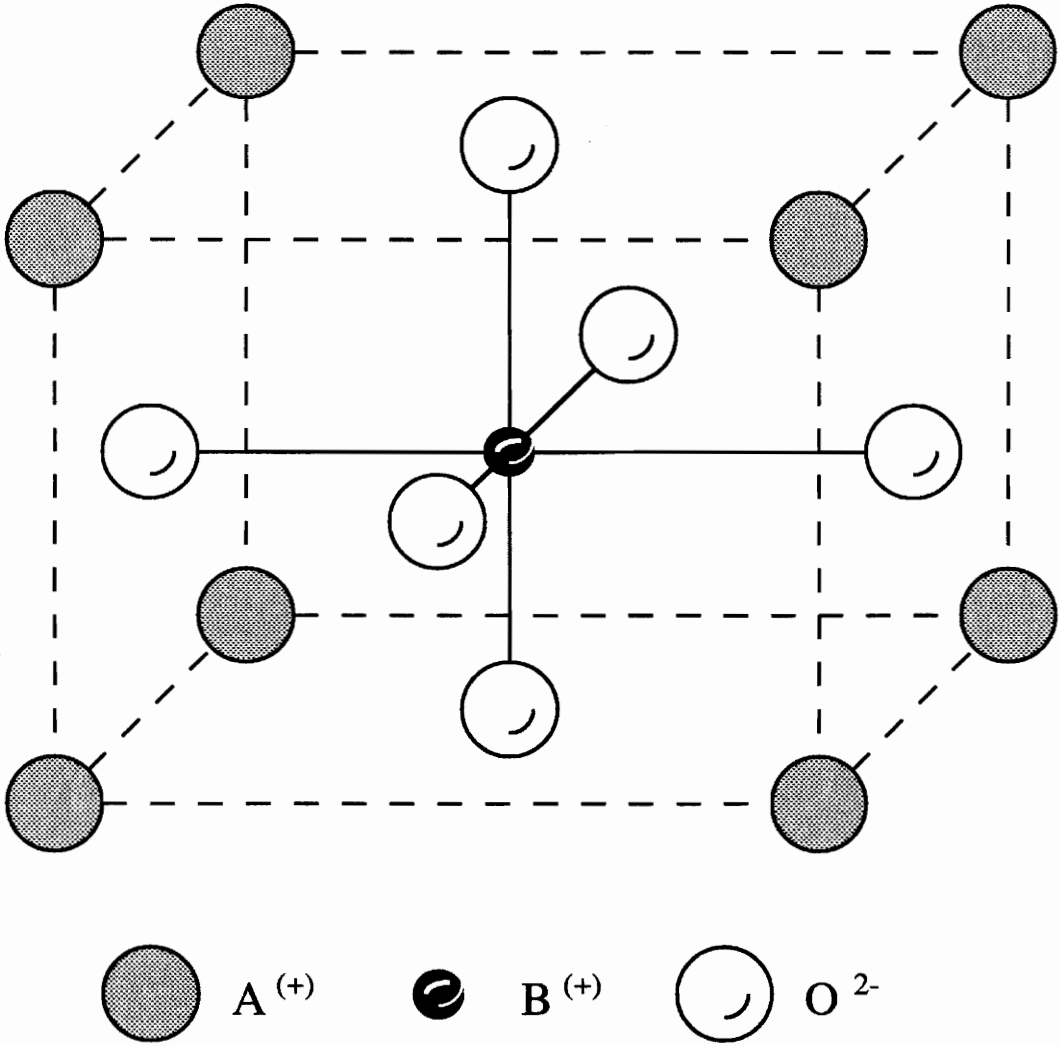


Figure 1.9 Unit cell of a simple perovskite (after Haertling, 1986).

1.4.3 Dielectric Behavior

Dielectrics in Static Fields

When an electric field is applied to an ideal dielectric, there is a limited rearrangement of charges in the material, instead of the long range transport of conductors, so that the dielectric develops a dipole moment and is polarized (Moulson and Herbert, 1990). In Figure 1.10, four of the various polarization processes are schematically demonstrated. All materials undergo atomic polarization, which involves a small displacement of electrons from the nucleus in the presence of an electric field. With ionic materials, there is also a relative movement of cation and anion sublattices. A material is dipolar, like water, if an electric field reorients molecules. The fourth type shown in Figure 1.10, space charge polarization, entails a limited transport of charge carriers until they are stopped by a barrier, such as a grain or phase boundary. For the dielectric PMN-PT, ionic and space charge types dominate polarization.

For a parallel-plate capacitor as in Figure 1.11, according to Gauss's theorem the electric field between and normal to the two plates carrying the total charge density, σ^T , is compensated in part by the polarization charge density, σ^P , accumulating on the dielectric surfaces:

$$E = \frac{\sigma^T - \sigma^P}{\epsilon_0}. \quad (1.1)$$

The total charge density is equivalent to the magnitude of the dielectric displacement vector, D ,

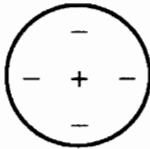
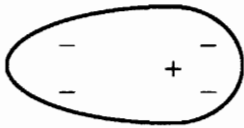
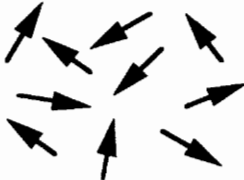
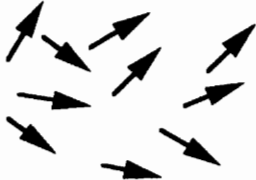

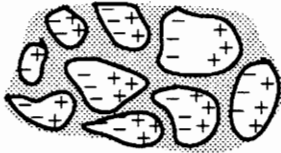
| Polarization Process | Unpolarized State | Polarized State |
|-----------------------------|---|--|
| | <i>Electric Field</i> → | |
| Atomic |  |  |
| Ionic | <pre> + - + - + - - + - + - + + - + - + - - + - + - + + - + - + - </pre> | <pre> +- +- +- - +- +- + +- +- +- - +- +- + +- +- +- </pre> |
| Dipolar |  |  |
| Space charge or diffusional |  |  |

Figure 1.10 Various polarization processes (after Moulson and Herbert, 1990).

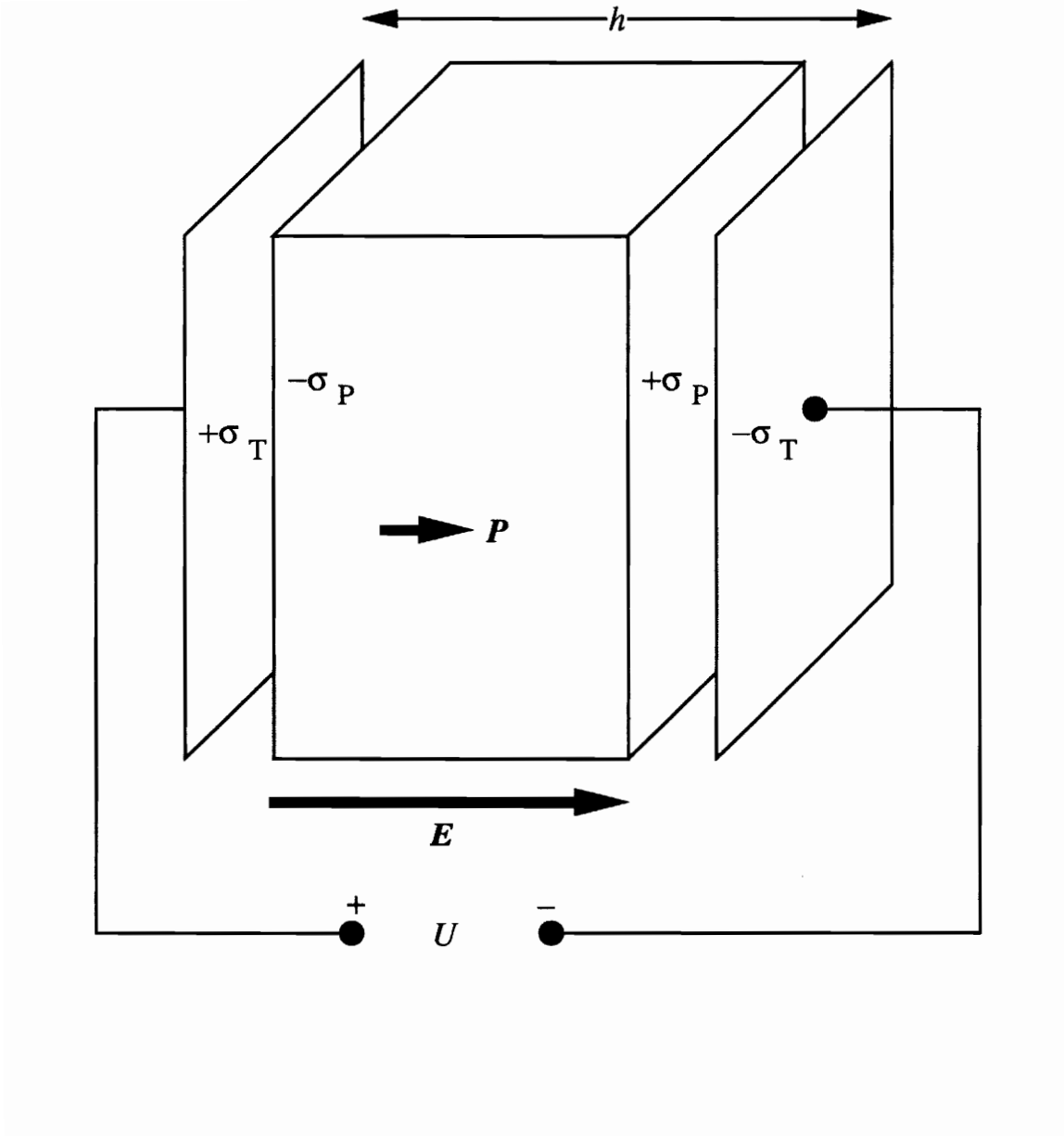


Figure 1.11 A parallel-plate capacitor filled with a dielectric medium (after Moulson and Herbert, 1990).

$$D = \epsilon_0 E + P. \quad (1.2)$$

For a linear dielectric, polarization is proportional to the applied electric field,

$$P = \chi \epsilon_0 E. \quad (1.3)$$

From equations (1.2) and (1.3), it follows that

$$D = (1 + \chi) \epsilon_0 E. \quad (1.4)$$

By substituting the electric displacement with σ_T and the electric field with U/h in equation (1.4),

$$\sigma_T = \frac{Q_T}{A} = (1 + \chi) \epsilon_0 \frac{U}{h}, \quad (1.5)$$

such that the capacitance

$$C = \frac{Q_T}{U} = (1 + \chi) \epsilon_0 \frac{A}{h} = (1 + \chi) C_0. \quad (1.6)$$

Relative permittivity, also known as the dielectric constant, is defined by

$$\epsilon' = 1 + \chi. \quad (1.7)$$

For high-permittivity solids, the relative permittivity and dielectric susceptibility are practically identical.

Dielectrics in Alternating Fields

By utilizing complex quantities to analyze AC circuits and by employing Euler's identity, a sinusoidal voltage, for example, may be expressed as follows:

$$U = U_0 \exp(j\omega t) = U_0 [\cos(\omega t) + j\sin(\omega t)]. \quad (1.8)$$

Therefore, the time derivative of the sinusoidal voltage of equation (1.8),

$$\dot{U} = j\omega U_0 \exp(j\omega t) = j\omega U. \quad (1.9)$$

For a capacitor filled with a dielectric and subjected to an AC voltage, the instantaneous charge $Q = U C$, so that the current, or instantaneous time derivative of charge,

$$I = \dot{Q} = \dot{U} C = j\omega C U. \quad (1.10)$$

The capacitive effect of a real dielectric is not perfect. This imperfection is termed dielectric loss and results in power dissipation. Mathematically, the consequences of a real, 'lossy' dielectric can be taken into account by introducing a complex relative permittivity, ϵ_r^* , composed of real and imaginary parts. From equations (1.6), (1.7) and (1.10), it follows that

$$I = j\omega \epsilon^* C_0 U = j[\epsilon' - j\epsilon''] \omega C_0 U = [j\epsilon' + \epsilon''] \omega C_0 U. \quad (1.11)$$

As indicated in the phasor diagram (or complex domain) of Figure 1.12 and apparent in equation (1.11), the alternating current across a dielectric material is composed of two components—one capacitive, thus requiring only reactive power, and the other real, thus dissipating energy. The dissipative component is in phase with the voltage U and can be viewed as 'capacitive resistance'; however, the analogy to resistance differs in the frequency dependence of dielectric power loss. As illustrated in Figure 1.12, the *permittivity ratio*,

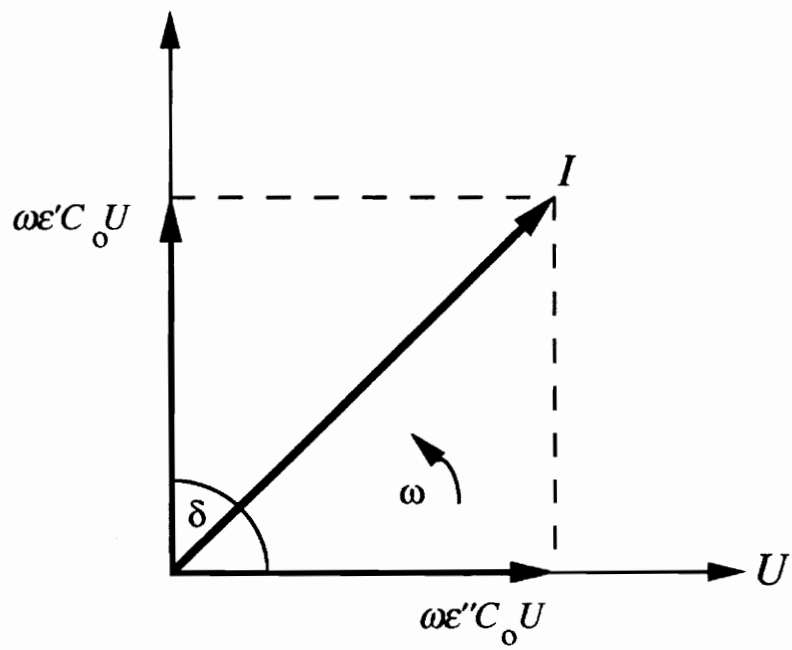


Figure 1.12 Complex capacitive components of the total current (after Moulson and Herbert, 1990).

$$\frac{\epsilon''}{\epsilon'} = \tan\delta, \quad (1.12)$$

describes the proportion of real-to-reactive power, whose inverse is a measure of the quality or efficiency of the dielectric. The permittivity ratio is also called '*dielectric loss*' or '*dissipation factor*.'

Temperature Dependence of Dielectric Properties

The spontaneous polarization characteristic of ferroelectrics arises from local fields that control the individual atoms and/or ions. Under certain thermal conditions, the lattice polarization can produce local fields which tend to stabilize the polarization, in a feedback-like mechanism, so that the material is spontaneously polarized (Moulson and Herbert, 1990). With respect to temperature, ferroelectric behavior is limited to a thermal range (material phase) above which the spontaneous polarization drops to zero and properties become paraelectric (normal dielectric). Close to this phase transition, the permittivity of normal ferroelectrics reaches a peak at the Curie point, T_C , and decreases in agreement with the Curie-Weiss law,

$$\epsilon' = \frac{W}{T - \theta_C}, \quad (1.13)$$

where θ_C is a temperature near the Curie point, as in Figure 1.8. Unfortunately, relaxors do not follow this thermal behavior; however, the Curie Weiss law provides useful insight into the thermal effects on permittivity of ferroelectrics, a class to which relaxors belong.

Dielectric Properties of PMN-PT

High-permittivity dielectrics, whose relative permittivities exceed 1,000, are generally ferroelectric and are more sensitive to temperature, field strength, and frequency than lower permittivity materials (Moulson and Herbert, 1990). PMN-PT is no exception. The relaxor ferroelectric character of PMN-PT is readily evident in its broad and frequency dispersive weak-field dielectric response, shown in Figure 1.13. The diffuse nature of the thermal phase change from ferroelectric to paraelectric states is apparent in the plots of both components of the relative permittivity. This broad phase change, occurring over a wide range of temperatures, does not follow the Curie-Weiss behavior common to normal ferroelectrics; furthermore, the maximum relative permittivity of PMN-PT can be much higher than other ferroelectrics, up to 34,000 (Swartz et al., 1984), and lends well to applications for capacitors or electrostrictors used in the ϵ_{\max} temperature range. In fact, PMN-PT is preferred to other compositions of PMN because its dielectric maximum is not only very large but also occurs near room temperature.

With respect to increased temperature, the spontaneous polarization of PMN-PT drops to zero near the T_{\max} , just as a ferroelectric loses spontaneous polarization at the Curie temperature, T_C . As in Figure 1.14, the spontaneous polarization steadily decays until it reaches the region in which permittivity begins to increase. At this point, it begins to drop abruptly, and then exponentially decays to zero at the T_{\max} . In normal ferroelectrics like PZT, the spontaneous polarization is relatively constant until the phase change to paraelectric, where it abruptly falls to zero.

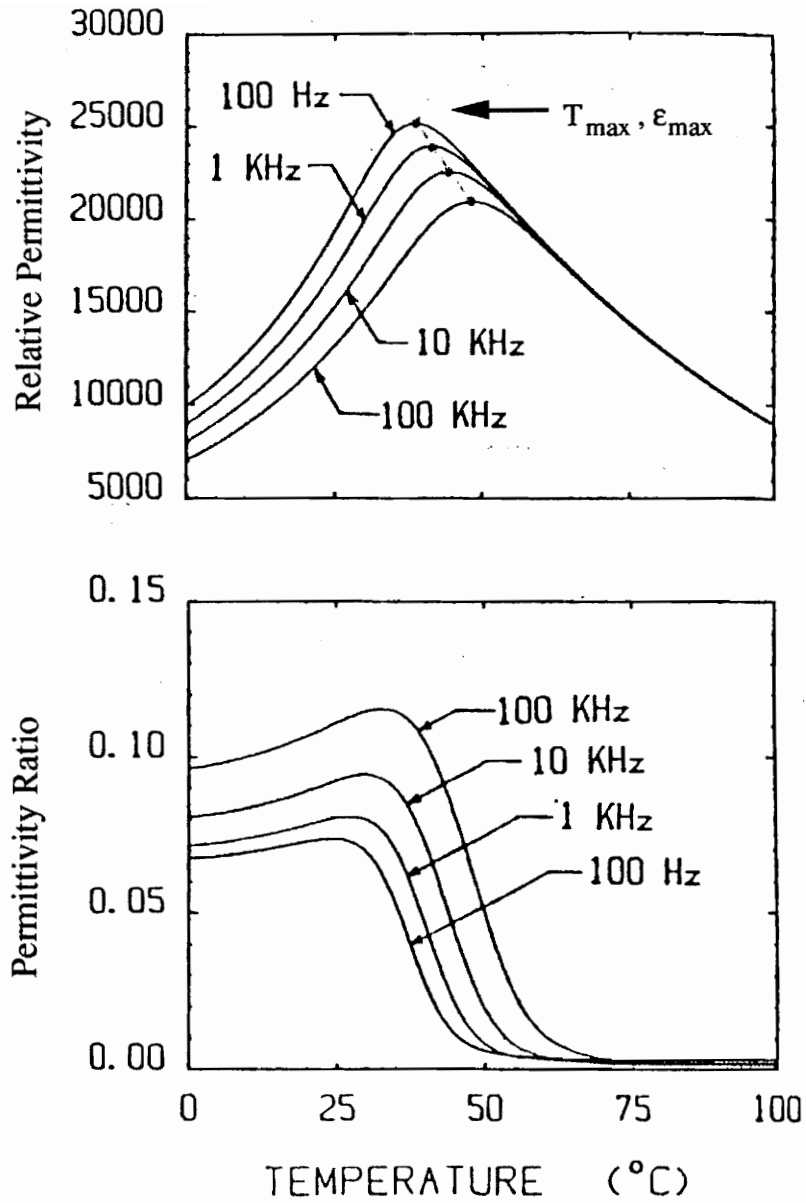


Figure 1.13 Dielectric response of PMN-PT at various frequencies through the ferroelectric-paraelectric phase transition (after Swartz et al., 1984).

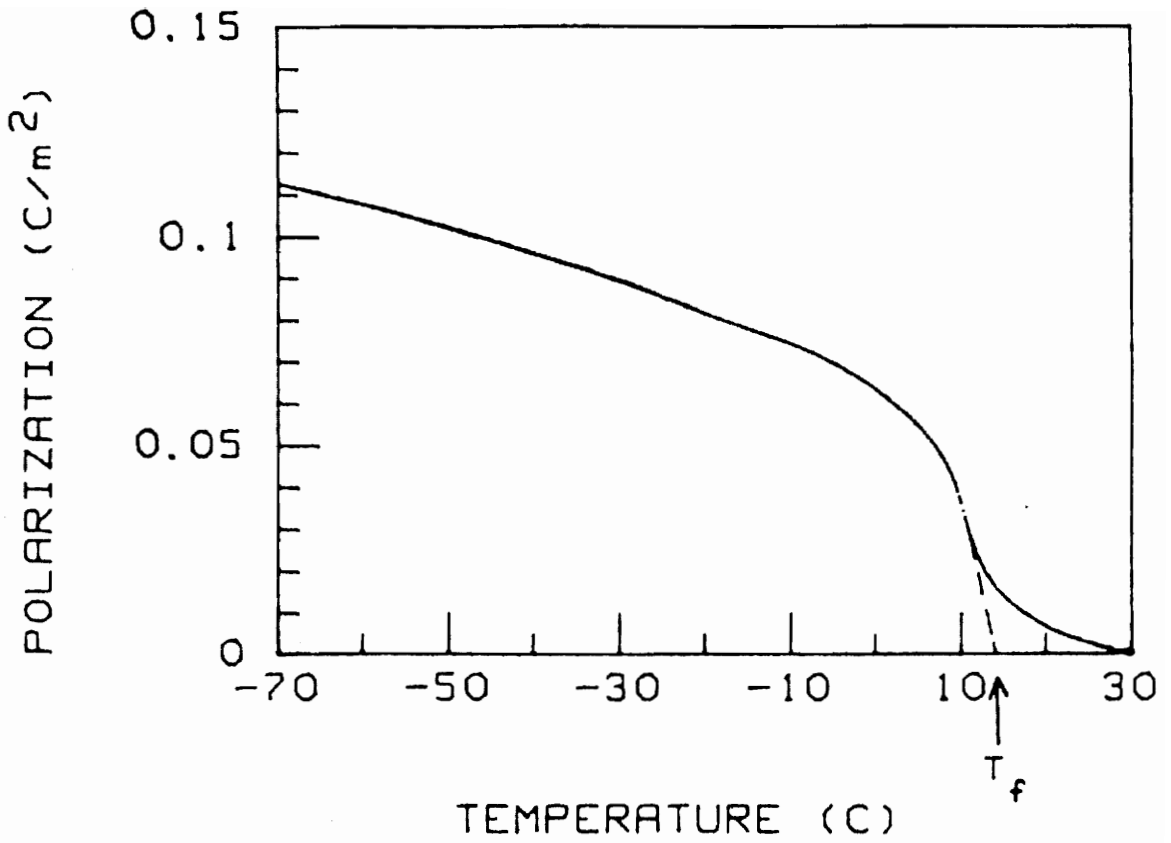


Figure 1.14 Spontaneous polarization of PMN-PT through its ferroelectric-paraelectric phase transition (after Viehland et al., 1990).

Frequency dependence is another characteristic of PMN-PT and other relaxors. The curves of Figure 1.13 demonstrate typical relaxor behavior, where the magnitude of the dielectric constant decreases with increasing frequency and where the maximum shifts to correspondingly higher temperatures (Viehland et al., 1990). In relaxor ferroelectrics, local energy barriers to the lattice polarization are distributed over a range in the structure (Pan et al. 1989). In the presence of a fixed, weak alternating field, frequency dispersion occurs because different times are necessary for polarization processes to overcome different energy barriers. This heuristic description is the basis for the superparaelectric model, which accounts for much of the relaxor dielectric behavior, as described in section 1.5.3.

Direct current (DC), or bias, electric field also affects dielectric properties of PMN-PT, as illustrated in Figure 1.15, which describes variation of weak-field relative permittivity with bias field. For these curves, the amplitude of the AC dielectric testing field is held constant for different fixed frequencies while DC fields applied to PMN-PT specimens are varied. While frequency variation of permittivity results from local polarization barriers, or clusters, having different time responses, higher DC bias fields may exclude contributions from more polarization processes manifest with energy barriers. As the bias field strength is increased, there are fewer energy barriers for the AC testing field to overcome (Pan et al., 1989). Consequently, both lattice permittivity and frequency dependence decrease.

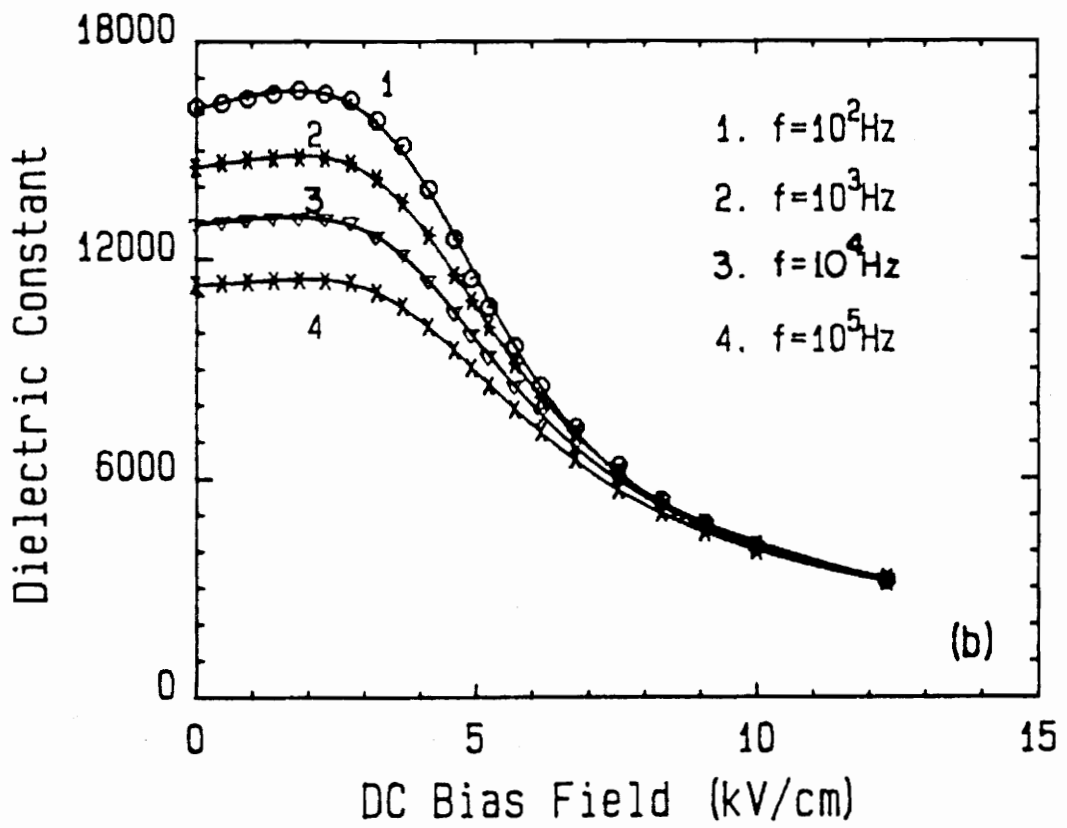


Figure 1.15 Weak-field relative permittivity of PMN-PT with respect to applied DC electric field at various frequencies (after Pan et al., 1989).

For electrostrictive relaxors such as PMN-PT, the permittivity also changes with stress, or pressure, as demonstrated in Figure 1.16. This linear relationship between pressure and dielectric properties is actually related to electrostrictive properties and can be described by Landau-Ginzburg-Devonshire thermodynamic phenomenology introduced later. The effect, however, is here introduced since it is dielectric in nature.

Finally, dielectric magnitudes are most notably affected by not only composition but also size of PMN-PT grains. Swartz et al. (1984) introduced forming processes which enhanced the dielectric permittivity of PMN-PT by as much as 50%. This increase was attributed entirely to increased grain size, as demonstrated for PMN in Figure 1.17. Studies of compositions for $(1-x)\text{Pb}[\text{Mg}_{1/3}\text{Nb}_{2/3}]\text{O}_3-(x)\text{PbTiO}_3$ have also indicated dielectric magnitude effects (Pan, et al., 1989); however, a 0.9PMN-0.1PT composition has been found to provide the best overall electrostrictive properties (Swartz et al., 1984). This composition is herein referred as PMN-PT unless otherwise noted.

1.4.4 Electrostrictive Responses

Motivation for the present study of PMN-PT relies on its capability for electromechanical transduction. Until now, electrical properties of the material have been considered. These dielectric properties are important to the overall electrostrictive effect, since the electromechanical response depends innately on the permittivity. However, there are other material parameters, or coefficients, which are important to the electrostrictive response and require further elaboration. All eleven centrosymmetric crystalline

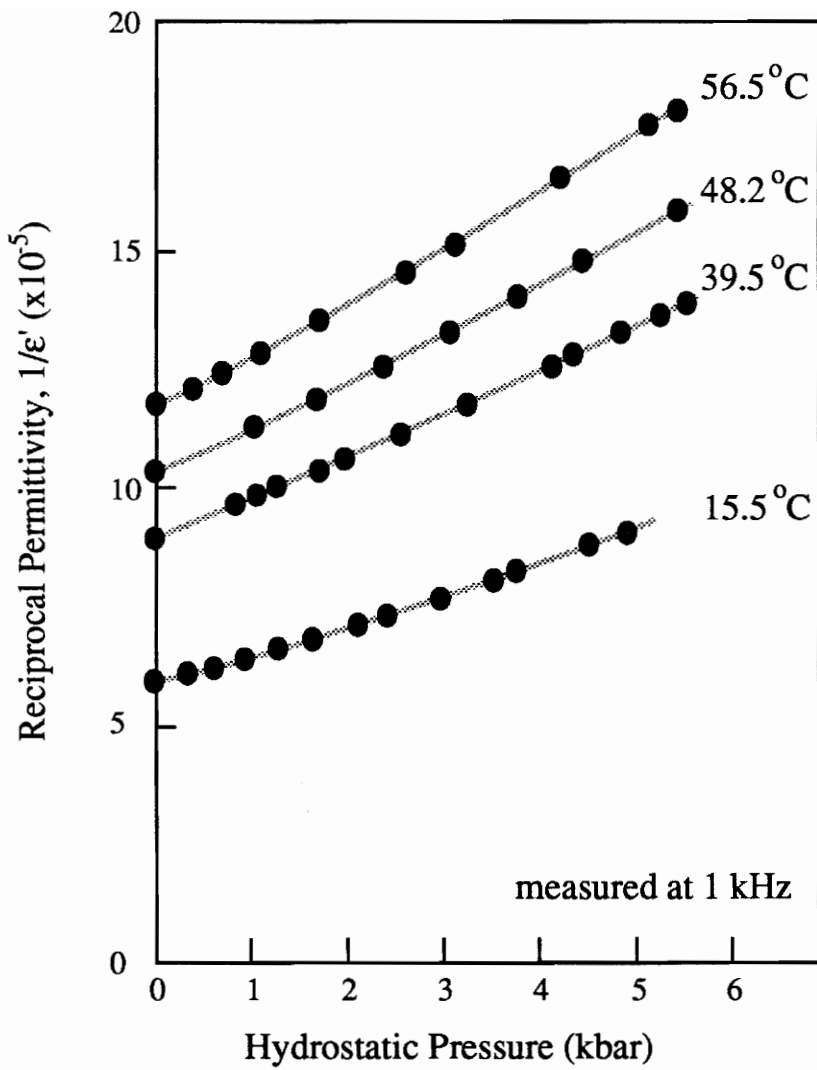
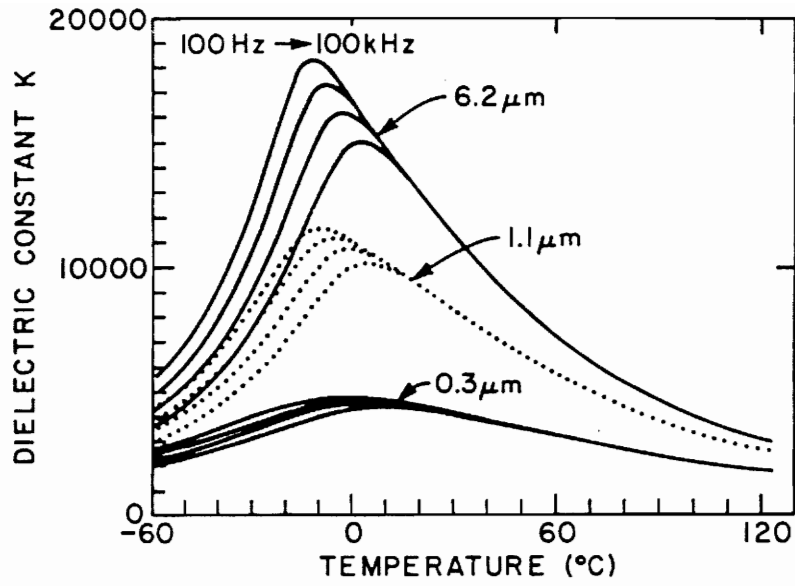


Figure 1.16 Hydrostatic pressure dependence of the reciprocal permittivity of PMN at various temperatures (after Nomura and Uchino, 1982).



(a)

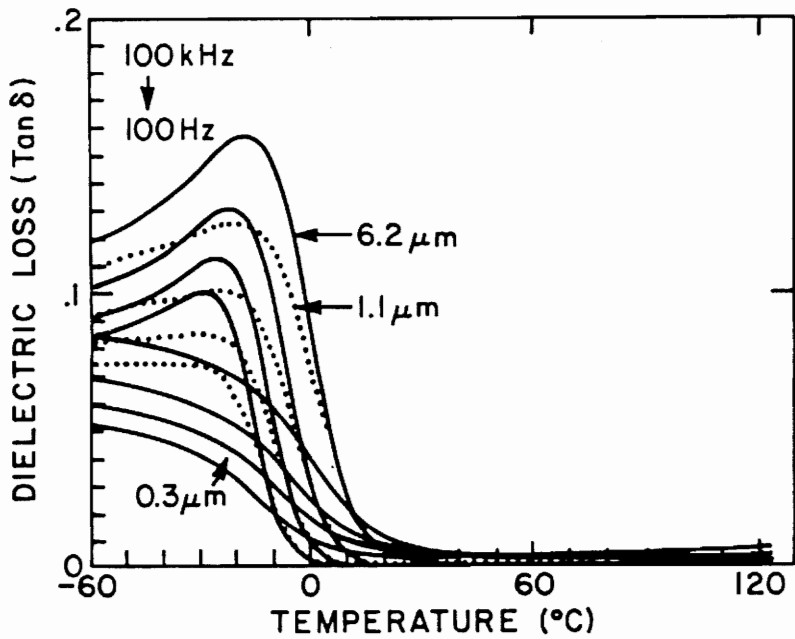
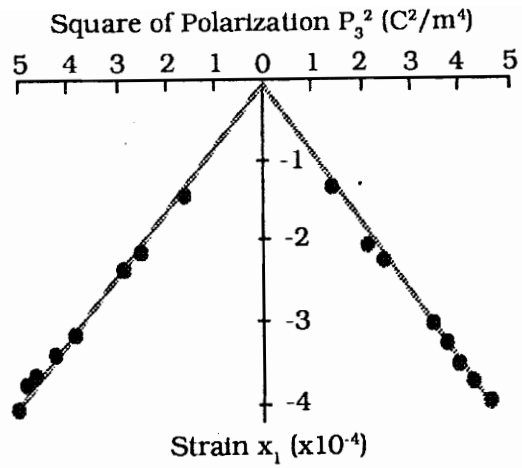


Figure 1.17 Grain size effects on the relative permittivity and permittivity ratio of PMN through its phase transition (after Papet, Dougherty and Shrout, 1990).

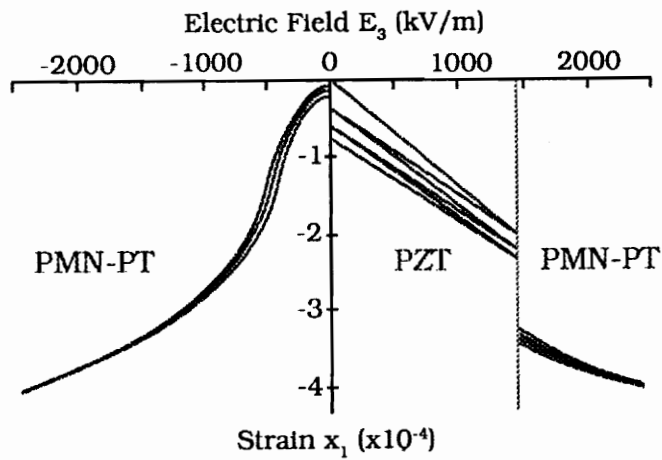
structures display direct electrostriction (Haertling, 1986). In fact, all crystalline materials exhibit small changes in dimension when subjected to an electric field (Moulson and Herbert, 1990). If the developed strain is proportional to the square of the polarization induced by an electric field, then the material is directly electrostrictive. Any polycrystalline material in which the crystal axes of the grains are randomly oriented behaves electrostrictively, regardless of the structural class of crystallites comprising the ceramic.

Relaxor ferroelectrics are such polycrystalline materials. The proportion between free-induced strain and polarization squared is termed the electrostrictive coefficient, and an example of this relation is provided in Figure 1.18 (a). For small fields or small variations in fields, polarization induced in PMN-PT is directly proportional to applied electric field, so that induced strain is proportional to applied field; however, over large fields lattice polarization begins to saturate. Nevertheless, as indicated in the comparisons of Figure 1.18 (b), the electromechanical response of PMN-PT at room temperature is less hysteretic than that of typical ferroelectrics like PZT, whose large hysteresis arises in the electric field-polarization relations.

Cartesian directions and physical origins of electrostriction are illustrated in Figure 1.19. In Figure 1.20, the temperature dependencies of PMN-PT electrostrictive coefficients for strains parallel and transverse to the direction of applied field are indicated. Since strain varies with the square of polarization, free-induced strain is unidirectional, i.e.,

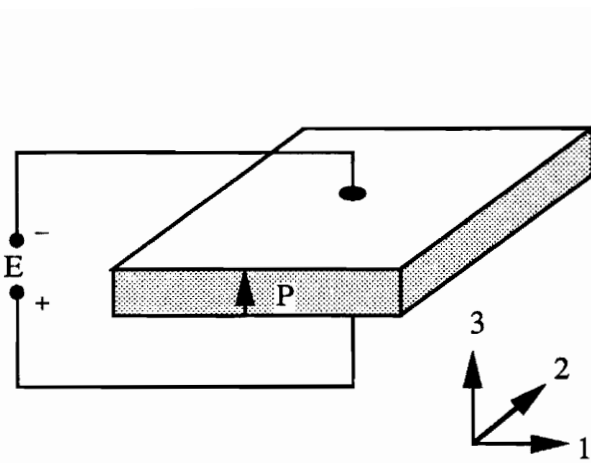


(a)

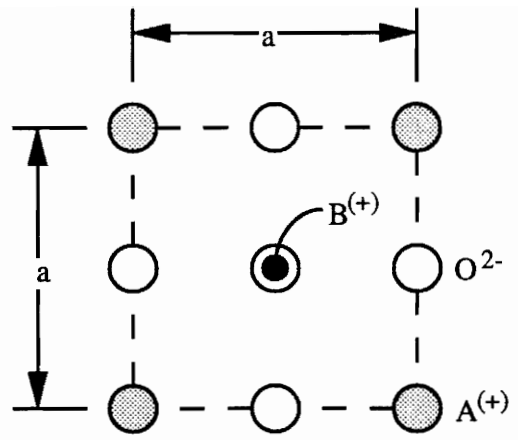


(b)

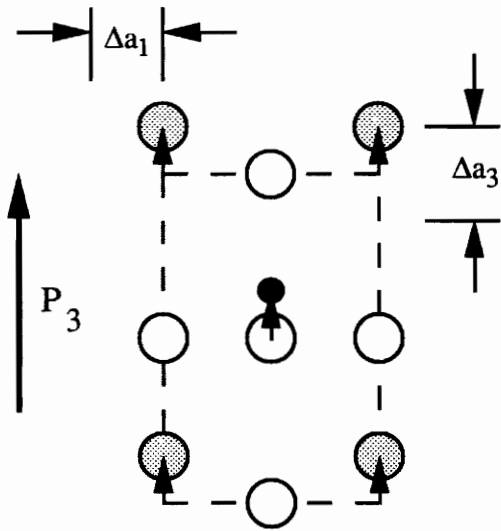
Figure 1.18 (a) Field-induced transverse strain of PMN-PT versus the square of electric polarization and (b) transverse strain in PMN-PT and a typical PZT under slowly varying electric fields (after Nomura and Uchino, 1982).



Electrostrictive Tensor Directions



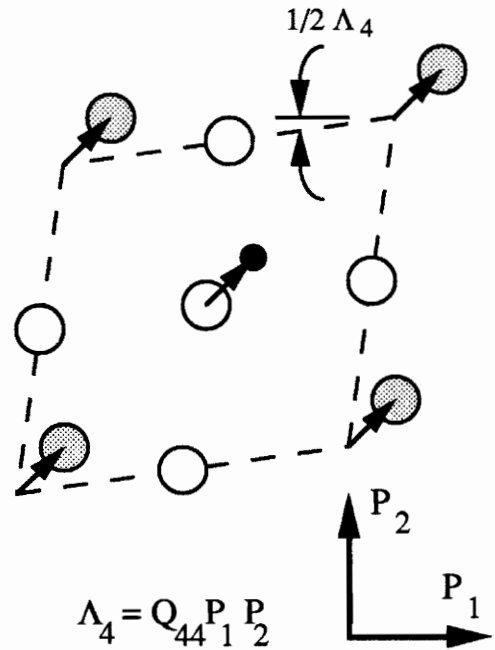
Cubic Perovskite



$$\Lambda_3 = \Delta a_3 / a = Q_{33} P_3^2$$

$$\Lambda_1 = \Lambda_2 = \Delta a_1 / a = Q_{13} P_3^2$$

Parallel and Transverse Strain



$$\Lambda_4 = Q_{44} P_1 P_2$$

Shear Strain

Figure 1.19 Cartesian directions and physical origins of electrostrictive coefficients in a cubic perovskite (after Newnham, 1991).

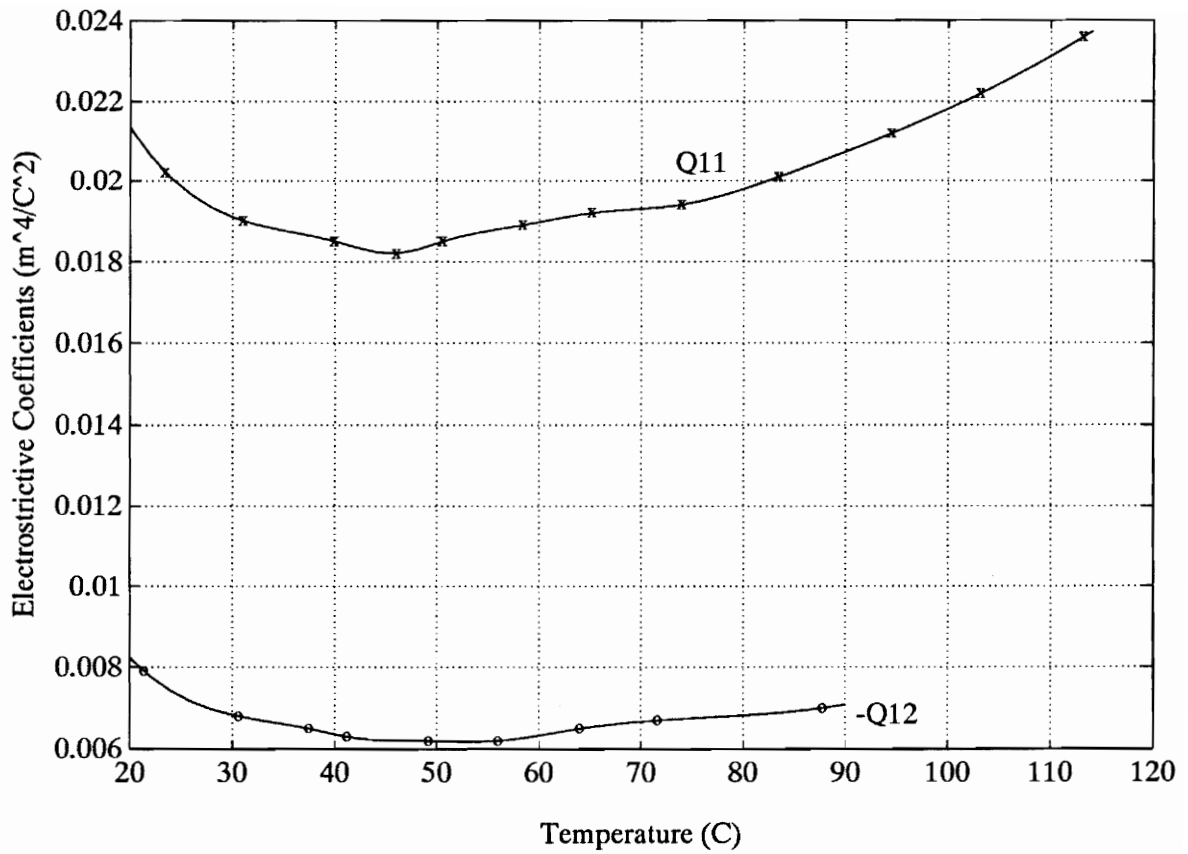


Figure 1.20 Electrostrictive coefficients for PMN-PT, for an electric field amplitude of 190 V/cm at 400 Hz, as a function of temperature (after Zhang et al., 1989).

independent of the direction of polarization, thus applied field. The direction of induced strain depends solely on the sign of the coefficient, so that a PMN-PT electrostrictor expands parallel to and contracts transverse to applied field. Interestingly, the trends in the electrostrictive coefficients oppose the trends in permittivity, as indicated in the field-amplitude dependence curves of Figure 1.21. If one compares curves of Figure 1.20 with those of Figure 1.13, this mirror relationship is also apparent with respect to temperature. Conspicuously missing from the literature on characterization of PMN-PT is the frequency dependence of electrostrictive coefficients.

PMN-PT also exhibits two converse electrostrictive effects, bias field-induced sensing and stress-dependent permittivity. Sensing capabilities were earlier implied in the description of the pulse-echo probe application illustrated by Figure 1.5. Stress-dependent permittivity was intimated in Figure 1.16. Mathematic expressions for these three electrostrictive effects can be derived from LGD thermodynamic phenomenology of solids and will prove most helpful in clarifying these relations.

1.5 Review of Constitutive Modeling for PMN-PT

In this section, models related to the electrostrictive and dielectric behavior of PMN-PT are introduced.

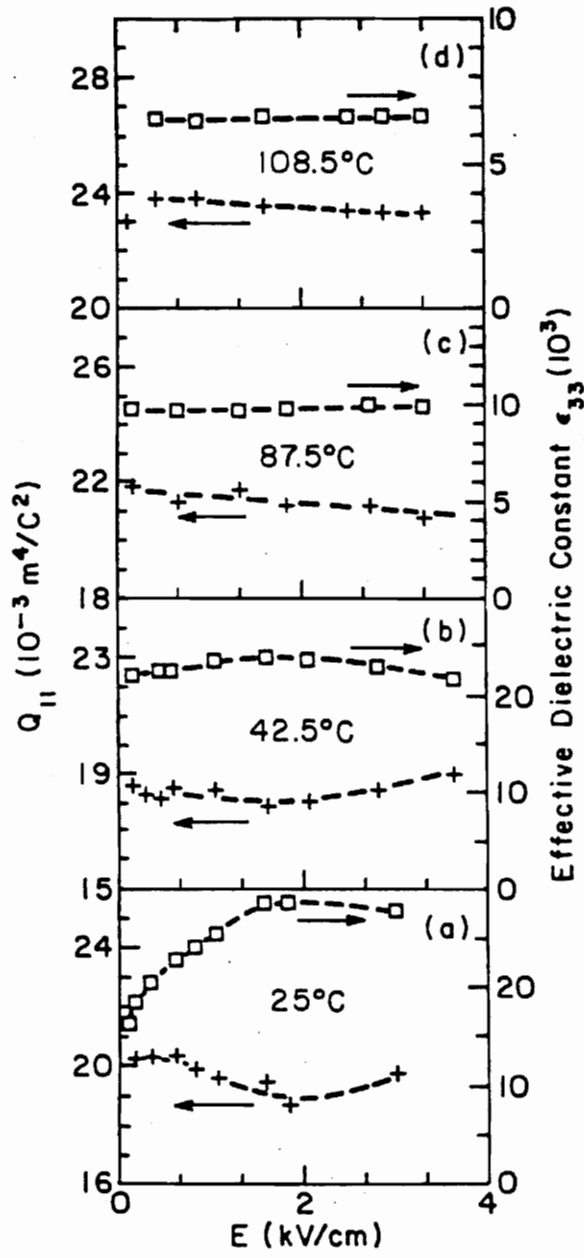


Figure 1.21 Field-amplitude dependence of electrostrictive coefficient parallel to applied field and effective relative permittivity for PMN-PT at (a) 25°C, (b) 42.5°C, (c) 87.5°C and (d) 108.5°C at 200 Hz (after Zhang et al., 1989).

1.5.1 Landau-Ginzburg-Devonshire Thermodynamic Phenomenology for Electrostriction

According to LGD thermodynamic formalism, relating dielectric and elastic properties of solids, electrostriction arises from the free energy terms (Newnham, 1991):

$$F = \dots + Q_{ijk} P_i P_j \sigma_{kl} + \dots \quad (1.14)$$

Three different but equivalent effects arise when the three possible partial derivatives of the terms of equation (1.14) are taken in different orders. In the first case, the direct effect, strain varies with polarization:

$$\frac{\partial}{\partial P_l} \left(\frac{\partial}{\partial P_k} \left(\frac{\partial F}{\partial \sigma_{ij}} \right) \right) = \frac{\partial^2 \Lambda_{ij}}{\partial P_k \partial P_l} = Q_{ijkl} \quad (1.15)$$

A second derivation describes the converse electrostrictive effect in which the reciprocal dielectric susceptibility depends on stress,

$$\frac{\partial}{\partial \sigma_{kl}} \left(\frac{\partial}{\partial P_j} \left(\frac{\partial F}{\partial P_i} \right) \right) = \frac{\partial \beta_{ij}}{\partial \sigma_{kl}} = Q_{ijkl} \quad (1.16)$$

Another converse effect arises from the third possible derivative order:

$$\frac{\partial}{\partial P_l} \left(\frac{\partial}{\partial \sigma_{jk}} \left(\frac{\partial F}{\partial P_i} \right) \right) = \frac{\partial g_{ijk}}{\partial P_l} = Q_{ijkl} \quad (1.17)$$

Integrations of the relations described in equations (1.15)-(1.17) yield three behaviors fundamental to electrostrictive relaxor ferroelectrics. With integrations of equation (1.15) with respect to polarization and reduction of tensor order, the free induced strain for a

relaxor ferroelectric may be described as follows:

$$\Lambda_i = Q_{ijk} P_j P_k + d_{ij}^o P_j + \Lambda_i^o. \quad (1.18)$$

Physically, the piezoelectric coefficient in equation (1.18) relates any effects from spontaneous polarization of an electrostrictor. Integration of equation (1.16) results in the following reduced relation for linear stress dependence of susceptibility:

$$\beta_i = Q_{ij} \sigma_j + \beta_i^o. \quad (1.19)$$

Since the voltage generation coefficient in equation (1.17) describes the electric field developed when an electroceramic is stressed, the field generated by a mechanically stressed electrostrictor, while assuming tensor order reduction for symmetry, follows:

$$E_i = (Q_{ijk} P_k + g_{ij}^o) \sigma_j + E_i^o. \quad (1.20)$$

For practical engineering design and implementation, polarization does not possess the parametric convenience of applied electric field. Conventionally, linear dielectric behavior is assumed and as in equation (1.3), induced polarization is described as the product of dielectric susceptibility and electric field. However, as illustrated in Figures 1.15 and 1.18 (b), dielectric properties of PMN-PT diminish with high electric fields and polarization thus saturates. Typically, engineers want to drive smart material system components to their limits, in order to achieve maximum structural control authority, so that a linear assumption for P-E relations is invalid for most intelligent material system and structure designs.

1.5.2 A Phenomenological Formulation for Ferroelectricity

To eliminate the implication of linear field-polarization relations and to illuminate the fundamental nonlinearity in ferroelectric ceramics, a phenomenological approach has been suggested for modeling ferroelectric behavior (Zhang and Rogers, 1992). The proposed approach calls for a hyperbolic tangent description of induced polarization, namely:

$$\begin{aligned} P_i &= P_i^s \tanh[k(E_i - E_i^c)]; \delta E > 0 \\ P_i &= P_i^s \tanh[k'(E_i - E_i^c)]; \delta E < 0. \end{aligned} \quad (1.21)$$

The hyperbolic tangent description accounts for the nonlinearity of polarization saturation which occurs in ferroelectrics, and the coercivity fields in equation (1.21) model the hysteresis.

Since relaxors have very little P-E hysteresis, especially with ferroelectric phases close to and paraelectric phases beyond the maximum Curie temperature, a curve representing the average between forward and reverse paths can be reliably used, i.e.,

$$P_i = P_i^s \tanh(kE_i). \quad (1.22)$$

This hyperbolic tangent description fits data reported for various frequencies and temperatures very well, as shown in Figure 1.22, and provides an excellent basis for modeling temperature, frequency, stress, and grain-size dielectric dependencies.

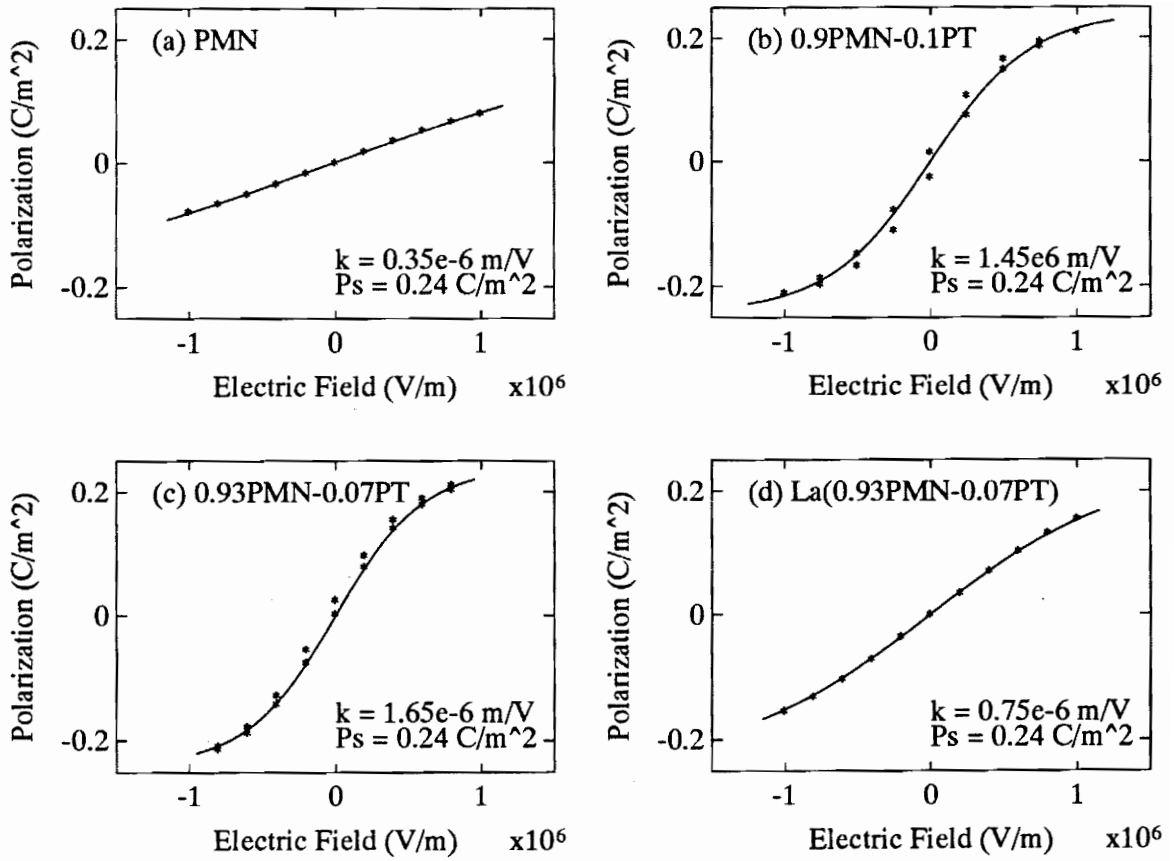


Figure 1.22 Hyperbolic tangent model fits of typical hysteresis loops for polycrystalline electrostrictive ceramics of (a) PMN, (b) 0.9PMN-0.1PT, (c) 0.93PMN-0.07PT and (d) $\text{La}_{0.01}[\text{0.93PMN-0.07PT}]_{0.99}$ (after Zhang and Rogers, 1992; Pan et al., 1989).

1.5.3 Compositional Variation and Grain Size Models for Relaxor Ferroelectric Behavior

Smolenskii (1961), who developed the PMN solid solution and laid the foundation for the discovery of PMN-PT, also originated the idea that compositional fluctuations, ‘submicroscopic structural inhomogeneities,’ which precipitate the relaxor ferroelectric properties of broad and frequency-dispersive transitions to paraelectric phases. He proposed that the diffuse transition arises from a random distribution of cations in their sublattice, while temporal anomalies arise from departures from such a distribution. In other words, the different B-site cations of a solid solution in the perovskite structure of Figure 1.9 are randomly distributed, except for locations where small clusters of similar B-cations form.

Rolov (1965) followed Smolenskii’s experimental observations with an empirical model he used to describe the relaxor phase transition. He proposed that fluctuations in compositions lead to a condition where various regions have different values for local Curie points. On this assumption, Rolov derived a mathematic model based on exponential probability distributions of cations, thus Curie temperatures, in the lattice. In doing so, he essentially smoothed over the discrete clusters proposed by Smolenskii and described a continuum of varying compositions in the lattice. The issue of frequency degeneracy remained.

Swartz et al. (1984) found that dielectric properties for PMN-PT are strongly affected

by sample preparation, both chemically and thermally, which primarily affect grain size. Shrout et al. (1987) supported this conclusion that dielectric and electrostrictive properties of PMN-based ceramics are strongly affected by microstructure, with an emphasis on grain size. Shrout proposed that grain-size dependency of PMN-PT can be attributed to a nanometer-scale amorphous grain boundary phase composed of PbO, which has low dielectric permittivity. With larger grains in the bulk material, the volume fraction of this low permittivity grain boundary is reduced. However, PMN-PT samples of similar grain size can have drastically different maximum permittivities. Shrout explained this behavior as the result of higher weight loss during processing due to PbO volatility and longer sintering times.

Furthermore, Shrout et al. related the wide range of ϵ_{\max} to the level of diffuseness of the phase transition and proposed a mathematic model analogous to that of Curie-Weiss for normal ferroelectrics. Shrout showed that 0.93PMN-0.07PT, a ferroelectric with diffuse phase transition, follows the law $1/\kappa \approx (T - T_{\max})^2$ over a wide range of temperatures. Similar to Rolov's work (1965), Shrout proposed that since the temperature distribution of local Curie temperatures is Gaussian in nature, a level of diffuseness, λ , can be used to relate the dielectric constant to $(T - T_{\max})^2$ with the following expression:

$$\frac{1}{\kappa} \approx \frac{1}{\kappa_{\max}} + \frac{(T - T_{\max})^2}{2\kappa_m \lambda^2}. \quad (1.23)$$

Although Shrout failed to mathematically relate the parameters κ_{\max} , T_{\max} , and λ to grain size or MgO content or to explore frequency dispersion, he did provide experimental

results with 0.93PMN-0.07PT which support equation (1.23), which indicate a converse relation between κ_{max} and λ , and which show evidence of grain size and processing dependence of κ_{max} , T_{max} , λ and Q_{12} , as listed in Table 1.1.

Cross (1987) revived the idea of compositional fluctuations in relaxor ferroelectrics and their effects on the diffuseness of phase transitions and on frequency dispersion of these phase transitions. Cross postulated that small polar micro-volumes in relaxor ferroelectrics could be thermally and dynamically unstable, thus analogous to a superparamagnetic state in which small ordered spin clusters establish an inadequate magnetocrystalline energy to remain stable against thermal motion. Cross set out to explore this potential 'superparaelectric' behavior by examining whether fluctuation in the concentration of B-site cations are responsible for the diffuseness of the phase change in $\text{Pb}[\text{B}'\text{B}'']\text{O}_3$ perovskite relaxor ferroelectrics, whether there is evidence for a substantial RMS polarization well above T_{max} , and if so, whether there are dynamical polar regions responsible for RMS polarization in this temperature range which 'flip' in orientation as with superparamagnets.

Citing work by Setter and Cross (1980) on order-disorder behavior of $\text{Pb}[\text{Sc}_{1/2}\text{Ta}_{1/2}]\text{O}_3$ (PST), Cross concluded that B-site fluctuations are responsible for the diffuse nature of the ferroelectric-paraelectric phase change since PST was a normal ferroelectric in an annealed, ordered state and a relaxor in quenched, disordered state. He also concluded that micro polar regions persist at temperatures above T_{max} through RMS spontaneous

Table 1.1 Experimental processing results for 0.93PMN-0.07PT (after Shrout et al., 1987).

| Firing Conditions | Wt. Loss (%) | ρ (g/cc) | Grain Size (μm) | κ_{max} | T_{max} ($^{\circ}\text{C}$) | λ ($^{\circ}\text{C}$) | Q_{12} ($\times 10^{-2} \text{ m}^4/\text{C}^2$) |
|---------------------------------|--------------|---------------|------------------------------|-----------------------|---|----------------------------------|--|
| 950 $^{\circ}\text{C}$, .5 hr | 0.5 | 7.4 | 1.5 | 11,500 | 24 | 58 | -0.55 |
| 950 $^{\circ}\text{C}$, 4 hr | 0.7 | 7.83 | 2 | 13,000 | 22.8 | 50 | -0.47 |
| 950 $^{\circ}\text{C}$, 48 hr | 0.6 | 7.88 | 2 | 20,300 | - | 39 | -0.59 |
| 1050 $^{\circ}\text{C}$, .5 hr | 0.8 | 7.88 | 2 | 12,600 | 20.6 | 57 | -0.47 |
| 1050 $^{\circ}\text{C}$, 4 hr | 0.5 | 7.91 | 3 | 15,700 | 20.5 | 44 | - |
| 1050 $^{\circ}\text{C}$, 20 hr | 1.1 | 7.89 | 3 | 18,800 | 22.2 | 43 | -0.45 |
| 1150 $^{\circ}\text{C}$, .5 hr | 0.7 | 7.87 | 3 | 13,500 | 19.7 | 48 | -0.59 |
| 1150 $^{\circ}\text{C}$, 4 hr | 1.0 | 7.88 | 3 | 17,800 | - | 43 | -0.56 |
| 1250 $^{\circ}\text{C}$, .5 hr | 1.1 | 7.84 | 5 | 17,500 | - | 44 | -0.53 |
| 1250 $^{\circ}\text{C}$, 4 hr | 1.2 | 7.82 | 6.5 | 20,800 | 18.4 | 42 | -0.60 |
| 1250 $^{\circ}\text{C}$, 20 hr | 1.5 | 7.76 | 9 | 22,800 | 17.9 | 39 | -0.70 |
| 1300 $^{\circ}\text{C}$, 4 hr | 1.1 | 7.82 | 6 | 21,000 | 18.7 | 41 | -0.49 |

polarization studies of the relaxor $[\text{Ba}_{2/5}\text{Sr}_{3/5}]\text{Nb}_2\text{O}_6$ (SBN). Furthermore, he showed indirect evidence for thermally dynamical disorders of these regions in SBN. Transmission electron microscope studies by Hilton et al. (1990) confirm that there is a nanometer-scale partitioning of chemically homogeneous clusters in PMN-PT, as well.

Viehland et al. (1990) suggested that it is the scale of lattice inhomogeneity which underlies the relaxor behavior and that these nanometer scale clusters are thermally dynamical, as with the SBN relaxor. Viehland carried Cross's superparamagnetic analogy for relaxor ferroelectric behavior one step further by proposing that these regions interact. Mathematic models based on a superparaelectric system of clusters with independent localized behavior failed to accurately predict the frequency dependence of T_{max} ; however, Viehland's proposed analogy to what's termed a spin-glass state of interacting superparamagnetic clusters proved more quantitatively viable. With spin-glass behavior, there exists a static freezing temperature, or glass transition temperature, which can be determined from the frequency dependence of the magnetic permittivity.

Viehland has shown, as in Figure 1.14 for PMN-PT, that such a static freezing temperature exists with respect to spontaneous polarization, thus lending credence to a spin-glass model for relaxor ferroelectricity. As such, a relationship for the frequency dependence of T_{max} can be ascertained from the Vogel-Fulcher model of magnetic relaxation in spin-glass systems:

$$T_{\max}(\omega) = -\frac{\alpha}{k_{\text{VF}} \ln(\omega/f_D)} + T_f \quad (1.24)$$

As shown in Figure 1.23, this relation holds very true for PMN-PT data, with an activation energy $\alpha = 0.0407$ eV, a Debye frequency $f_D = 1.03 \times 10^{12}$ Hz, and a freezing temperature $T_f = 18.5^\circ\text{C}$.

Continuing with the analogy to magnetic spin glasses, Viehland et al. (1991a) modeled the temperature dependence of the susceptibility loss—almost identical to the relative permittivity loss, delineated in equations (1.7), (1.11) and (1.12)—as the product of frozen, $r(T)$, and dynamic, $R(u)$, contributions:

$$\chi''(T, \omega) = r(T)R(u), \quad (1.25)$$

where

$$R(u) = \frac{1}{2} [1 + \tanh(u)] \quad (1.26)$$

$$u = c(\zeta - \alpha).$$

u is a scaling variable composed of the frequency-dependent cutoff energy, ζ , and the activation energy derived from equation (1.24). This phenomenological relation, based on Courtens model for magnetic spin glasses, fits thermal data for the susceptibility loss of PMN well; however, Viehland et al. (1991a) did not attempt to model the more important quantity of susceptibility, or relative permittivity, which appears in the electrostrictive relationships.

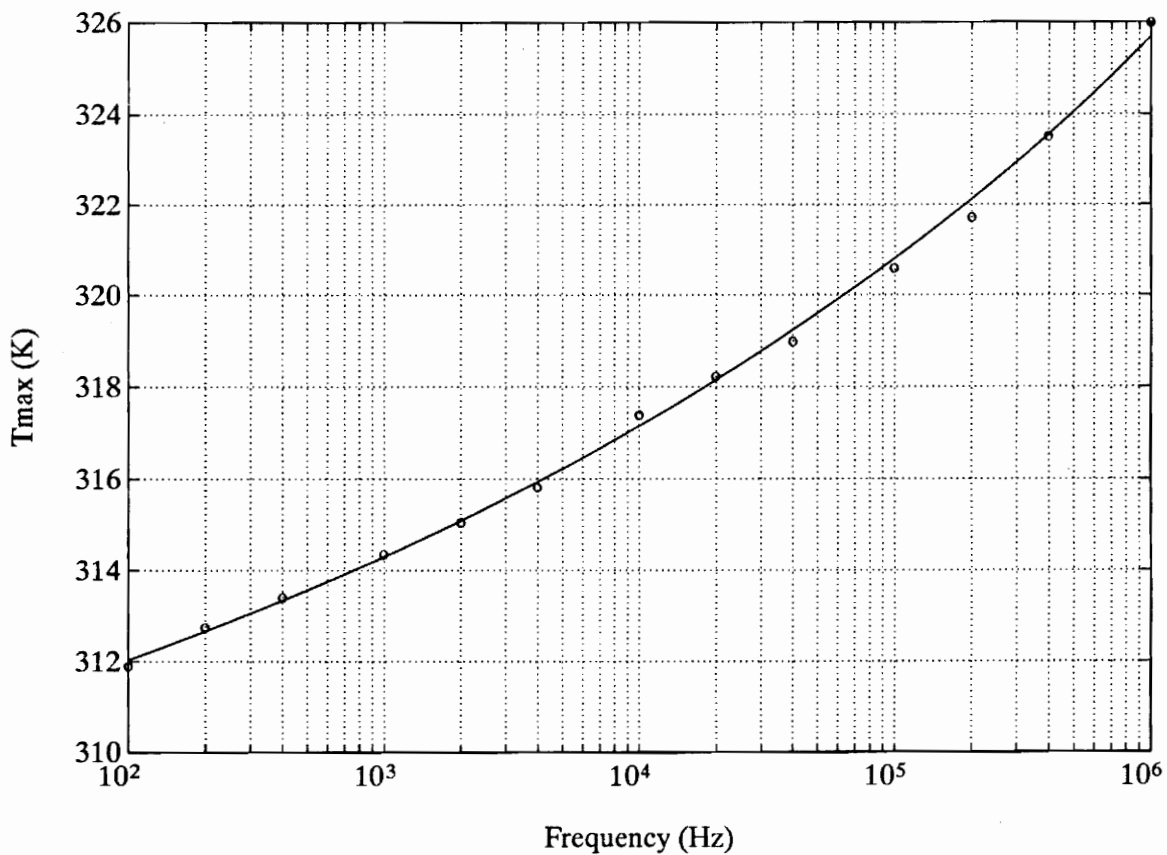


Figure 1.23 Temperature of the dielectric maximum as a function of the measurement frequency (after Viehland et al., 1990).

Although equations (1.25) and (1.26) can be useful for power considerations in design with electrostrictive relaxors, the most useful mathematic modeling results of microscopic studies are in the phenomenological relation of equation (1.23) for the dielectric constant and the spin-glass model relation of equation (1.24) for the temperature of maximum permittivity. By far, the LGD phenomenology of equations (1.18)-(1.20) for electrostriction and the relation of equation (1.22) for ferroelectric polarization will prove most useful to engineering design. Nevertheless, the temperature and frequency dependence of dielectric properties with PMN-PT must be accommodated in these engineering models.

1.6 Summary

Quotes from a prefatory paragraph and an introductory paragraph, respectively, in Moulson's and Herbert's Electroceramics: Materials, Properties, Applications (1990) best summarize Chapter 1 of this text and form the transition to the remaining chapters: "When you can measure what you are speaking about, and express it in numbers, you know something about it; but when you cannot measure it, when you cannot express it in numbers, your knowledge is of a meagre and unsatisfactory kind; it may be the beginning of knowledge, but you have scarcely, in your own thoughts, advanced to the state of science. (Lord Kelvin, 1883)"

"Ceramics comprise crystallites that may vary in structure, perfection and composition as well as in size, shape and the internal stresses to which they are subjected. In

addition, the interfaces between crystallites are regions in which changes in lattice orientation occur, often accompanied by differences in composition and attendant electrical effects. As a consequence it is very difficult, if not impossible, to account precisely for the behaviour of ceramics. The study of single-crystal properties of the principal components has resulted in valuable insights into the behaviour of ceramics. However, the growth of single crystals is usually a difficult and time-consuming business while the complexities of ceramic microstructures renders the prediction of properties of the ceramic from those of the corresponding single crystal very uncertain. Consequently, empirical observation has usually led to the establishment of new devices based on ceramics before there is more than a partial understanding of the underlying physical mechanisms."

Although there has been much characterization of PMN-PT introduced in Chapter 1, these investigations have been conducted primarily within the realm of electronic material science, where processing and its effect on dielectric response reign. In most cases, the electromechanical effects have been viewed as an aside. The objective of the research described in the following chapters is to investigate and model, albeit through 'empirical observation,' the electromechanical behavior of PMN-PT, with an emphasis on utility in engineering design.

Chapter 2

Experimental Design and Procedure

In this chapter, designs of experiments to investigate the actuation, sensing, and dielectric properties of PMN-PT and the fundamental material parameters governing those properties are presented. Since actuation and sensing are valuable capacities for intelligent material systems, the electromechanical characterization of these properties is vital to design of PMN-PT components implemented in such systems and structures. In order to differentiate electrical from mechanical effects on these behaviors, dielectric properties are studied. Finally, grain size dependence of electromechanical properties is investigated for use in material-based modeling efforts.

2.1 PMN-PT Specimen History

To associate experiments herein described with results in the literature, the processing history of PMN-PT samples must first be considered. Specimens of the solid solution $0.9\text{Pb}[\text{Mg}_{1/3}\text{Nb}_{2/3}]\text{O}_3-0.1\text{PbTiO}_3$ (PMN-PT) were manufactured at AVX Corporation using mixed oxides calcined through the two-stage procedure introduced by Swartz et al. (1984). The calcined mixture was milled in a slurry and tape cast. Platinum electrodes were screen printed onto the green cast, and the composite was fired. The specimens were formed in the shape of plates, having dimensions approximately $0.0572\text{ m} \times 0.0127$

m x 0.00043 m; though, there was some curvature observed for most of the plates. Some of these plates were tested as prepared, and some were scribed and fractured to produce smaller specimens. The edges of fractured pieces were sanded with emery paper and cleaned with acetone to ensure there was no short between electrodes.

2.2 Actuation Property Experiments

Actuation with PMN-PT involves the direct electrostrictive effect, described by the derivation of LGD phenomenology in equation (1.18). In this equation, free-induced strain is related to applied polarization; this parabolic relationship is corroborated by the plot of Figure 1.18 (a). However, polarization is not a practical measure; whereas, the applied electric field which induces polarization is. Experimental studies of actuation are thus conducted with respect to applied field, and dielectric studies described later are correlated with actuation results, in order to separate and quantify the electrostrictive coefficient of equation (1.18).

As indicated in equation (1.18), the electrostrictive coefficient is a tensor quantity. Because of symmetry of the cubic perovskite PMN-PT and planar isotropy with respect to polarization direction, this tensor can be described by only two quantities for a unidirectionally applied electric field:

$$Q_{ij} \Rightarrow \begin{bmatrix} Q_{11} & Q_{13} & Q_{13} \\ Q_{13} & Q_{11} & Q_{13} \\ Q_{13} & Q_{13} & Q_{11} \end{bmatrix}. \quad (2.1)$$

From equation (2.1), it should be apparent, in light of equation (1.18), that electric field applied in the direction of one material Cartesian coordinate will result in strain both parallel and transverse to the direction of induced polarization (applied field). Bi-directional transverse strain is uniform because of planar isotropy of dielectric and electrostrictive properties.

In Figures 1.20 and 1.21 (pp. 44 and 46), variations of the coefficient Q_{11} with respect to temperature and bias field, respectively, are indicated. Figure 1.20 also shows thermal effects on Q_{13} ; in fact, the trends for both coefficients are similar. For thin plates, or monomorphs, as in Figure 1.1 (p. 10), the coefficient of primary interest is Q_{13} , since transverse strain causes bending in a bimorph-type configuration or local extensional strain and bending for a monomorph bonded to a substrate. Although the stack configuration of Figure 1.3 (p. 13), which makes use of Q_{11} , proves useful in applications like the printer head of Figure 1.4 (p. 14), the transverse-strain bonded configuration is more typically utilized with intelligent material structural applications of vibration and shape control. Because Q_{13} is more pertinent to structural control, has been less investigated than Q_{11} , and shows variational trends similar to Q_{11} , it was characterized using the experimentally viable strain-gage technique described below.

As illustrated in Figure 2.1, electromechanical properties of PMN-PT were determined by monitoring both the electric field applied across parallel-plate electrodes and the corresponding free-induced strain, measured by a strain gage bonded to the monomorph

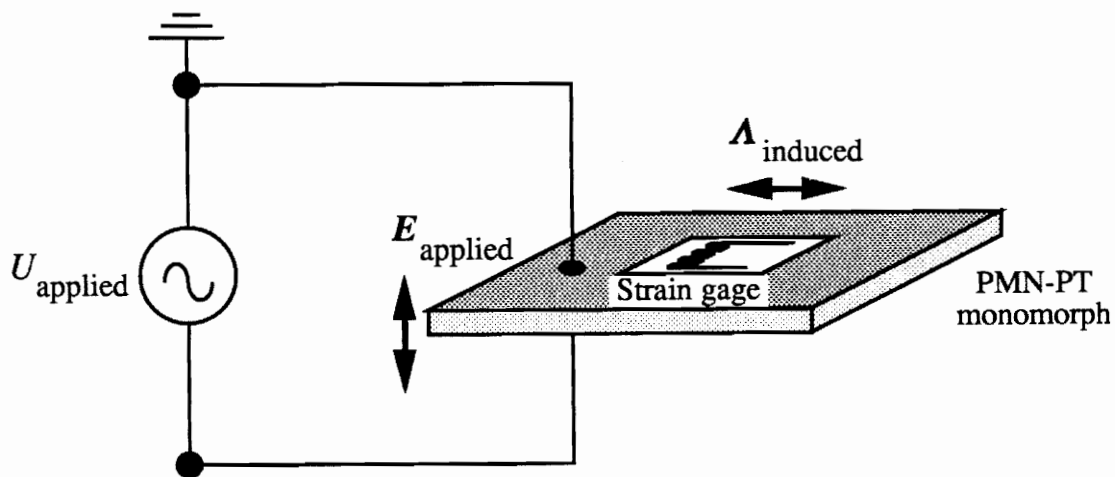
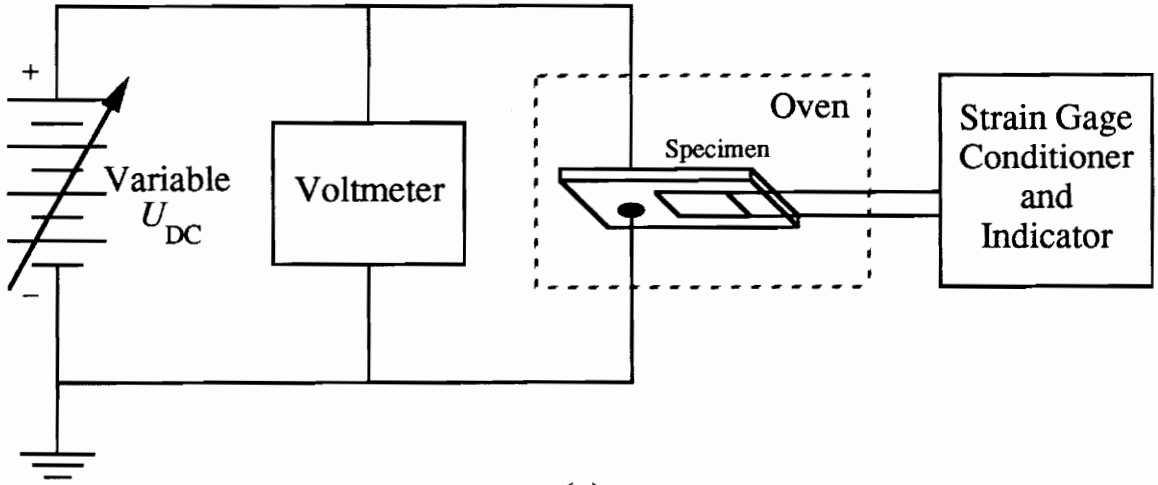


Figure 2.1 Strain-gage technique for observing the transverse direct electrostrictive effect in PMN-PT.

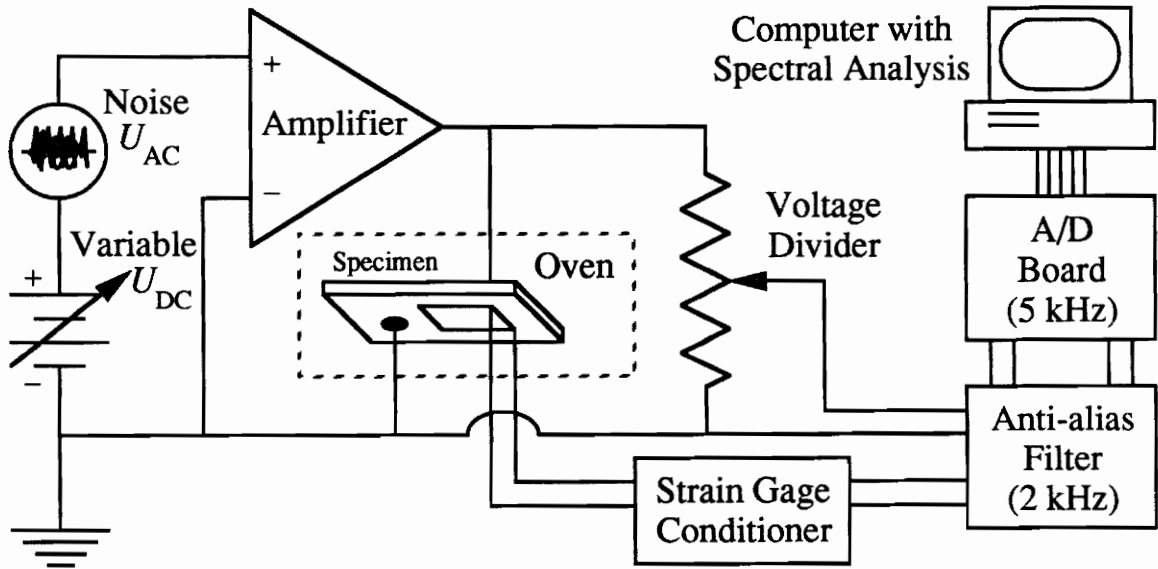
surface. It is important to note that the strain gage was bonded to the grounded electrode of the specimen, to avoid capacitive feed-through of voltage to strain measurements. Since strain gages cannot be bonded to both electrodes, a full or half bridge cannot be used to measure strain at a given cross section. Therefore, a quarter bridge configuration with internal dummy resistance was employed, and a uniform strain-field was assumed. Strain was measured accurately to $\pm 1 \mu\text{m/m}$, according to manufacturer specifications.

Two sets of experimental apparatus, illustrated in Figure 2.2, were utilized for two types of measurement, static and dynamic. As shown in Figure 2.2 (a), static measurements were obtained by stepping DC voltage applied to PMN-PT specimens up and down with a potentiometer and by measuring the steady-state strain response at each step. Frequency response measurements were acquired through digital conversion of voltage and strain signals, as in Figure 2.2 (b), and Fast (Discrete) Fourier Transform spectral analysis of digitized data. High levels of applied voltage were resistively divided for proportional measurement of electric field with a data acquisition board, which is limited to $\pm 10 \text{ V}$ inputs. The input impedance of the voltage divider was carefully selected with respect to the capacitance of PMN-PT specimens to ensure that electrical dynamics were unaffected. AC voltage was measured to an accuracy of $\pm 5 \text{ mV}$ for a $\pm 10 \text{ V}$ range, while DC voltage was measured to $\pm 1 \text{ mV}$.

In both experimental setups, temperature of PMN-PT specimens was varied with an oven



(a)



(b)

Figure 2.2 Experimental apparatus for (a) static and (b) dynamic measurement of the transverse direct electrostrictive effect with PMN-PT.

to investigate thermal (phase transition) effects. Specimens were placed next to the controlling thermocouple of the oven to ensure temperature accuracy within $\pm 0.5^\circ\text{C}$. To simulate free boundary conditions in the transverse plane, specimens were suspended in the oven by their electrode solder connections. Although this configuration created local stress variation near the solder joints, the magnitude of these variations were negligible, because of the PMN-PT ceramic's stiffness and relatively low density.

For dynamic measurements, a moderate AC electric field was used to electromechanically excite the PMN-PT specimens, while a DC bias field was concurrently applied and stepped, so that bias-field effects on PMN-PT behavior could be surmised. The amplifier used in these experiments was capable of providing simultaneous DC and AC high-gain, low-current amplification of voltages supplied to specimens. Broad-band frequency responses were created using a noise generator as the AC input, whose amplified signals were limited to 75 kV/m amplitudes. FFT spectral analysis of electromechanical data from PMN-PT required A/D conversions at 5 kHz to avoid aliasing at 2 kHz.

The thicknesses of all specimens were identical, at around 0.43 mm; however, the electrode areas, thus specimen capacitances, varied. Specimens ranged in dimensions from 0.0589 m x 0.0125 m to 0.0289 m x 0.0126 m. Nevertheless, the lowest fundamental extensional-mode frequency was at 28.4 kHz, well above 2 kHz, such that any modal effects on dynamic measurements were designed to be negligible.

Table 2.1 Specifications for PMN-PT transverse actuation experiments.

| | |
|--------------------------------|--|
| Specimens | 28.9 - 58.9 x 12.5 x 0.43 mm ³ 28.4 - 47.9 kHz first extensional mode 427 - 1,773 Hz first bending mode |
| Strain Gages | 0 $\mu\text{m}/\text{m}$ thermal expansion compensation $\pm 1 \mu\text{m}/\text{m}$ accuracy |
| Strain Gage Conditioner | Quarter bridge configuration 0.496 mV/ $\mu\text{m}/\text{m}$ transduction |
| Oven | 25 - 85°C experimental operating range $\pm 0.5^\circ\text{C}$ accuracy |
| DC Supply | 0 - 400 V (DC tests) 0 - 18 V (AC tests) |
| Noise Generator (AC Supply) | ± 1.5 V maximum amplitude 0 - 20 kHz random noise |
| Amplifier | 20(x) gain 0 - 5 kHz frequency response |
| Voltage Divider | 1:10 ratio 56 k Ω input impedance |
| Anti-alias Filter | 8-pole, 6-zero elliptical 2 kHz cutoff setting 100 - 189(x) gain on strain signal 1(x) gain on voltage signal |
| PC Computer and A/D Board | Two channels 0 - 14 kHz sampling range 1024-point FFT, 60 averages |

Table 2.2 Text matrix for PMN-PT transverse actuation experiments.

| | | Temperature (°C) | | | | | |
|-------------------|-----|------------------|---------|---------|---------|---------|---------|
| | | 25 | 35 | 45 | 55 | 65 | 85 |
| Bias Field (kV/m) | 116 | 0-2 kHz | 0-2 kHz | 0-2 kHz | 0-2 kHz | 0-2 kHz | 0-2 kHz |
| | 233 | 0-2 kHz | 0-2 kHz | 0-2 kHz | 0-2 kHz | 0-2 kHz | 0-2 kHz |
| | 349 | 0-2 kHz | 0-2 kHz | 0-2 kHz | 0-2 kHz | 0-2 kHz | 0-2 kHz |
| | 465 | 0-2 kHz | 0-2 kHz | 0-2 kHz | 0-2 kHz | 0-2 kHz | 0-2 kHz |
| | 581 | 0-2 kHz | 0-2 kHz | 0-2 kHz | 0-2 kHz | 0-2 kHz | 0-2 kHz |
| | 698 | 0-2 kHz | 0-2 kHz | 0-2 kHz | 0-2 kHz | 0-2 kHz | 0-2 kHz |
| | 814 | 0-2 kHz | 0-2 kHz | 0-2 kHz | 0-2 kHz | 0-2 kHz | 0-2 kHz |

To summarize, the actuation experiments were intended to investigate free-induced-strain electromechanical responses of PMN-PT with respect to temperature, bias field, and frequency. Specifications for these experiments are outlined in Table 2.1, and the test matrix is shown in Table 2.2. Thermal effects between 25°C and 85°C, corresponding with the diffuse ferroelectric-paraelectric phase transition of PMN-PT, were studied. Influences of bias field levels between 0 and 814 kV/m were determined, and frequency responses between 0 and 2 kHz were investigated.

2.2 Sensing Property Experiments

Similar to the actuator experiments, the sensor experiments with PMN-PT involved investigation of transverse electrostrictive properties, specifically the charge developed on parallel-plate electrodes resulting from the stress applied transverse to the direction of polarization. As is evident in equation (1.20) on p. 48, the level of electric field generated by a stressed electrostrictor depends on how much the sensor is polarized. Contributions to the transduction sensitivity, the collective terms between applied stress and generated field in equation (1.20), arise from the electrostrictive effect of applied polarization, as well as any piezoelectric effects due to remnant polarization. Since applied polarization varies with applied electric field, there is a bias-field dependence of the electrostrictive sensor transduction sensitivity apparent in the LGD phenomenological derivation of equation (1.20). The experimental arrangement for observing transverse electrostrictive sensing properties using the strain-gage technique is shown in Figure 2.3.

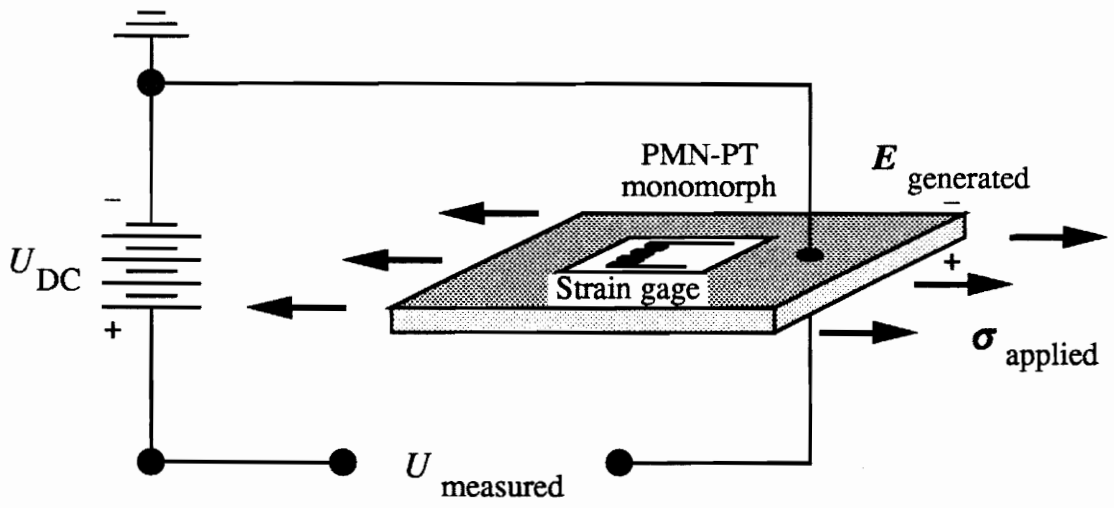


Figure 2.3 Strain-gage technique for observing transverse electrostrictive sensing properties of PMN-PT with respect to applied bias field.

In addition to characterizing properties of PMN-PT with respect to bias field, sensing experiments included observations of PMN-PT behavior with respect to frequency. The difficulty with experiments for sensing behavior involved designing a mechanism to apply uniformly distributed stress/strain fields to excite the sensor over a broad frequency range. Several techniques were investigated, such as bonding a piezo monomorph directly to a PMN-PT specimen and actuating the piezo device to induce stress across the PMN-PT plate; however, problems in measurement arising from local electric and magnetic fields disqualified this and similar techniques.

As indicated in Figure 2.4, PMN-PT monomorphs were bonded to the base of a cantilever beam, which was excited using an electromagnetic shaker with random noise input. Strain gages were attached to the exposed, unbonded surface of a PMN-PT specimen and to the opposite, unbonded surface on the beam. Transfer function analysis was performed for each strain signal with respect to the sensor output, while care was taken to ensure that the strain gage of interest was on an electrically grounded surface. The average of these two analyses for each sensor test was chosen to represent the sensor transduction capabilities; thus, an average, uniform strain field was determined and assumed to represent the input to PMN-PT sensor specimens.

Specifications for sensing experiments are provided in Table 2.3, and the test matrix is listed in Table 2.4. As in the actuation studies, bias fields ranged from 0 to 814 kV/m. Data were digitally collected at 2 kHz, with anti-alias frequency of 500 Hz. Beam

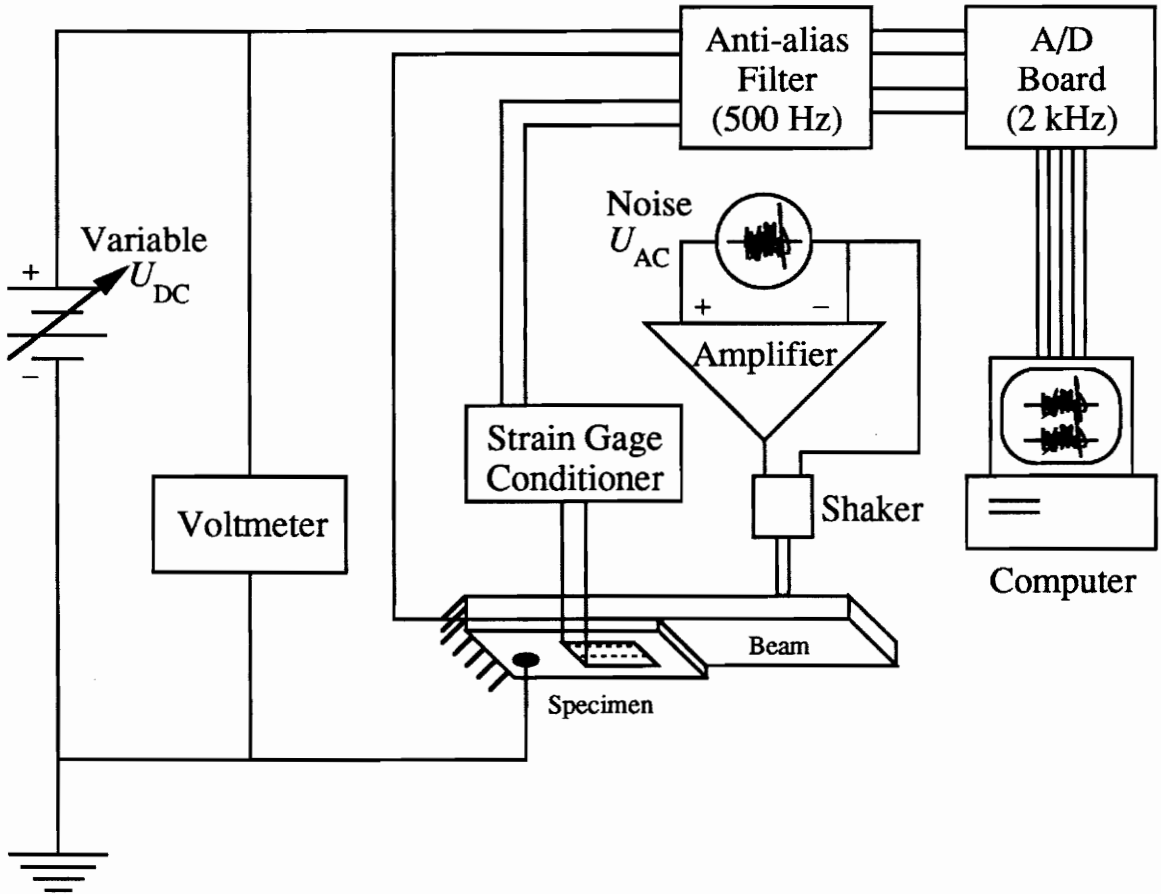


Figure 2.4 Experimental apparatus for measurement of transverse electrostrictive sensing properties of PMN-PT.

Table 2.3 Specifications for PMN-PT transverse sensing experiments.

| | |
|--------------------------------|---|
| Specimens | 23.6 - 57.2 x 12.5 x 0.43 mm ³ |
| Strain Gages | 0 $\mu\text{m}/\text{m}$ thermal expansion compensation $\pm 1 \mu\text{m}/\text{m}$ accuracy |
| Strain Gage Conditioner | Quarter bridge configuration 0.496 mV/ $\mu\text{m}/\text{m}$ transduction |
| DC Supply | 0 - 350 V |
| Voltmeter | $\pm 1 \text{ mV}$ |
| Noise Generator (AC Supply) | $\pm 1.5 \text{ V}$ maximum amplitude 0 - 20 kHz random noise |
| Shaker | 17.8 N force, $\pm 2.50 \text{ mm}$ stroke 0 - 12.5 kHz frequency range |
| Beam | Aluminum, 63.5 x 20.3 x 3.1 mm ³ 4.0 kHz fundamental bending mode |
| Amplifier | 0 - 5 kHz frequency response |
| Anti-alias Filter | 8-pole, 6-zero elliptical 500 Hz cutoff setting 100(x) gain on strain signal 2 - 100(x) gain on voltage signal |
| PC Computer and A/D Board | Two channels 0 - 14 kHz sampling range 1024-point FFT, 60 averages |

Table 2.4 Text matrix for PMN-PT transverse sensing experiments.

| Bias Field (kV/m) | Frequency (Hz) |
|--------------------------|-----------------------|
| 0 | 0 - 500 |
| 116 | 0 - 500 |
| 233 | 0 - 500 |
| 349 | 0 - 500 |
| 465 | 0 - 500 |
| 581 | 0 - 500 |
| 618 | 0 - 500 |
| 814 | 0 - 500 |

dimensions were designed so that the first bending mode was larger than the maximum frequency of interest for the studies, in this case 500 Hz. Since only bending mode vibration occurred in the beam, only flexural stresses were transmitted to the PMN-PT sensing specimens. High frequencies of 2 kHz were not feasibly studied in this configuration, due to the difficulty of exciting structural elements at such high frequencies. Furthermore, thermal effects could not be reliably tested using the shaker-beam configuration, so that thermal and high frequency results on sensing properties were waived for analytical correspondence to actuation and dielectric experiments.

2.3 Dielectric Property Investigations

In order to quantify the individual parameters contributing to the electrostrictive effects, dielectric properties between parallel plates of specimens used for actuation and sensing investigations were distinguished. The dielectric response of PMN-PT monomorphs were examined using an impedance analyzer, which was capable of examining electrical response functions from 100 Hz to 100 MHz. For these experiments, testing frequencies ranged from 100 Hz to 10 kHz, and the parameters investigated included capacitance and permittivity ratio. Relative permittivity was readily determined from capacitance measurements, including analytical adjustments for edge effects.

As exhibited in the test matrix of Table 2.5, temperatures of PMN-PT specimens were varied between 15°C and 85°C, which encompasses the range of the diffuse phase transition. Bias field effects were not examined during this test, mainly because the

Table 2.5 Text matrix for PMN-PT dielectric experiments.

| Temperature (°C) | Frequency (kHz) |
|-------------------------|------------------------|
| 15 | 0.1 - 10 |
| 25 | 0.1 - 10 |
| 35 | 0.1 - 10 |
| 45 | 0.1 - 10 |
| 55 | 0.1 - 10 |
| 65 | 0.1 - 10 |
| 75 | 0.1 - 10 |
| 85 | 0.1 - 10 |

impedance analyzer was not equipped to handle such large DC bias fields. Therefore, the bias field effects on the PMN-PT dielectric constant reported by Pan et al. (1989) were relied upon to correlate dielectric and electrostrictive relations for experimental results and for constitutive modeling.

The stress-dependence of reciprocal susceptibility of equation (1.19) was not explored in these experiments. Studies in the literature (Nomura and Uchino, 1982; Zhang et al. 1989) describe this converse electrostrictive effect thoroughly. The linear relationship illustrated by Figure 1.16 has been established. Nevertheless, this effect is extremely important to constitutive modeling of electrostrictive effects of PMN-PT and will be considered throughout.

2.4 Grain Size Studies

To correlate grain size of specimens used in the experiments described in this document with data reported in the literature (Swartz et al, 1984; Shrout et al., 1987; Papet, Dougherty and Shrout, 1990), the cross-section of a fractured specimen was viewed with a scanning electron microscope (SEM) at 3,000(x) and 5,000(x) magnifications. SEM micrographs were prepared, and an average grain size was ascertained using the intercept method. One-hundred intercept-method measurements from ten different locations on the cross section were calculated from 3,000(x) magnification micrographs and averaged. Measurements from 5,000(x) micrographs were performed to validate results.

Chapter 3

Experimental Results and Discussion

Results from a thorough experimental investigation of properties related to electrostrictive transverse sensing and actuation with polycrystalline PMN-PT are discussed in this chapter. Dielectric results are first introduced, so that more meaning can be derived from actuation and sensing transfer function studies. Results from these three sets of experiments are discussed in the context of the separate properties which contribute to electrostriction. Finally, results from scanning electron microscope examination of grain size are discussed and are correlated to previously published results.

3.1 Dielectric Results

Since polarization is an extrinsic parameter used to describe electrostrictive relations for actuation and sensing in equations (1.18) and (1.20) on p. 48 and since electric field is related and is more practical for engineering design, the dielectric properties which associate field and polarization are essential to a model-based description of electrostriction with the relaxor ferroelectric PMN-PT. For this reason, experimental results for dielectric properties are described prior to actuation and sensing results. Although much of the existing literature pertaining to PMN-PT involves characterization of electric permittivity relations, it was important to identify the relations for specimens

used in the present study, so that electromechanical results can be appropriately interpreted. The test matrix for these studies is listed in Table 2.5 (p. 76).

In Figure 3.1, results for the weak-field (2.3 kV/m) relative permittivity and permittivity ratio of PMN-PT specimens described in Chapter 2 are shown with respect to temperature. The broad and frequency-dispersive thermal phase transition typical of relaxor ferroelectrics is evident in this figure. Values and shapes of curves in Figure 3.1 correspond well with results in Figure 1.13 (p. 34), obtained by Swartz et al. (1984) for PMN-PT with a processing history similar to the specimens in this study. It should be noted here that the standard deviation ranged from 50 to 180 for relative permittivity data and from 0.0001 to 0.0026 for permittivity ratio data.

Characteristically, higher frequency excitations result in a reduced, or dispersed, dielectric constant and increased dielectric loss for the ferroelectric-dominated phases prior to the dielectric maximum. With the onset of paraelectric phases, frequency dependence is negligible. These frequency relations are notable in the dielectric frequency response plots of Figure 3.2. For temperatures past the T_{max} of around 45-50°C, the relative permittivity and permittivity ratio are flat with respect to frequency. For temperatures beneath the dielectric maximum, there is a linear decay of the dielectric constant and an increase in permittivity ratio with respect to the logarithm of frequency. This linear semi-logarithmic relationship will be utilized in the models of Chapter 4.

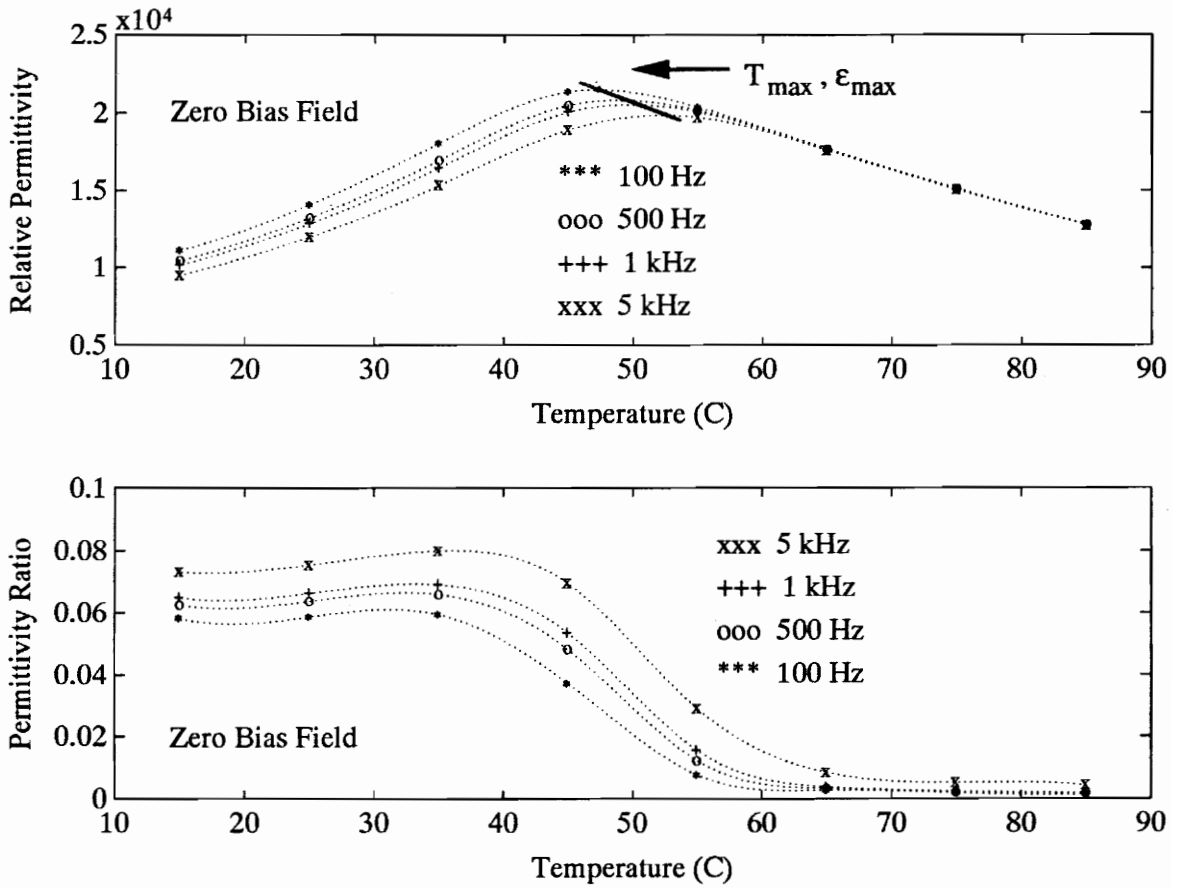


Figure 3.1 Dielectric results versus temperature for various frequencies.

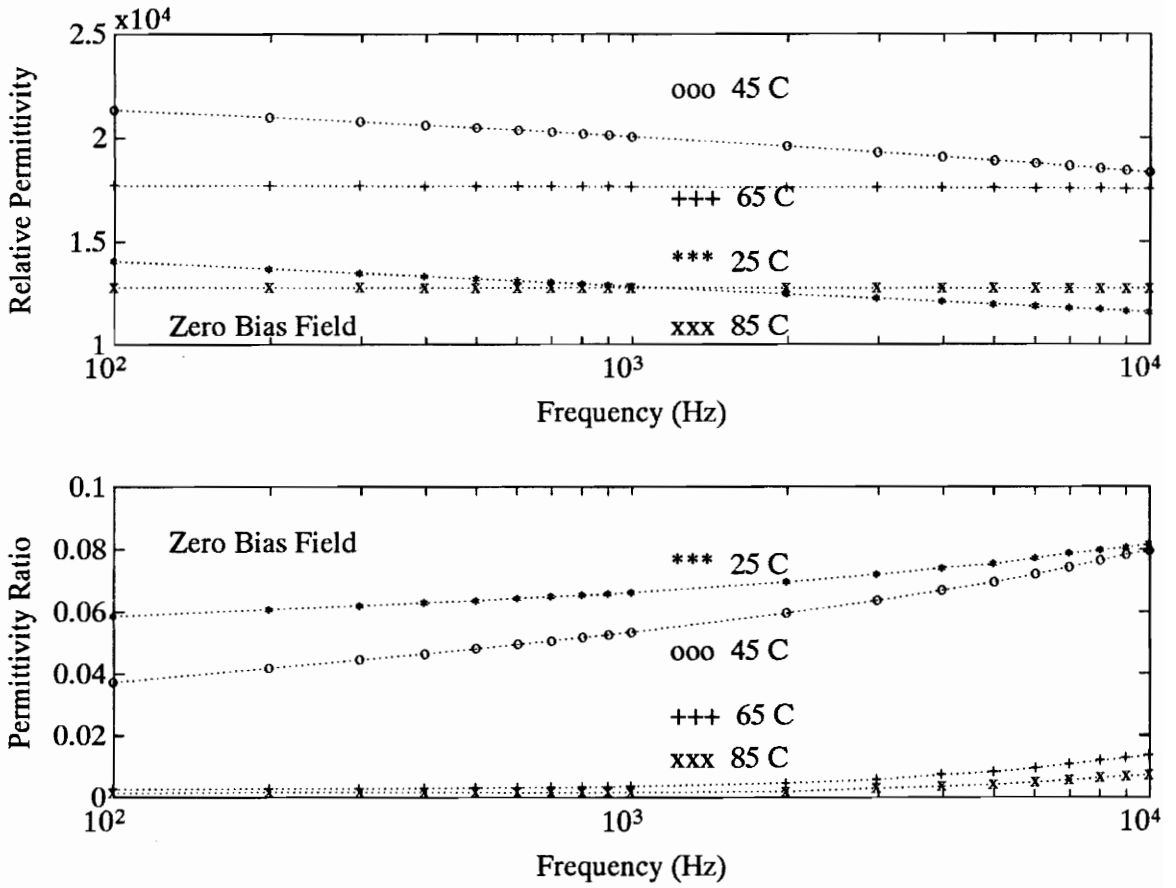


Figure 3.2 Dielectric frequency responses at various temperatures.

Effects of bias field on dielectric properties were not encompassed in this study, since the impedance measuring equipment used was not capable of accommodating large bias fields. Bias-field relations are, however, embedded in the actuation and sensing studies. As such, the bias dependence of permittivity will be determined through analyses of these results and will be described in the modeling of Chapter 4.

Since the consequences of effectively three extrinsic parameters—temperature, bias field, and frequency—are investigated, there are six possible permutations to represent behavior of dielectric properties. Two of these are provided in Figures 3.1 through 3.2 and are direct results of experimental data. In fact, only three of the six permutations are sufficient for co-dependent description, since the other three are simply converse relations; however, the converse results of Figures 3.1 through 3.2 describe only one of the three sufficient relations, temperature-frequency. Frequency-bias field and bias-field-temperature relations remain to be explored. To develop robust constitutive relations for the temperature-frequency-bias field co-dependence of intrinsic parameters, analysis must be performed, with appropriate assumptions, based on comparisons of the results obtained from the three sets of experiments—dielectric, sensing, and actuation. The actuation results will prove to be a good basis, since all extrinsic dependencies were simultaneously investigated. Analyses and modeling are reserved for Chapter 4.

3.2 Actuation Results

In Table 2.2 (p. 68), the test matrix for investigating the actuation response of PMN-PT

specimens shows that electromechanical properties were simultaneously investigated with respect to temperature, frequency, and electric bias field. These investigations have prompted some interesting results, especially when compared with dielectric results previously described. For example, in the plots of Figure 3.3, frequency dispersion is much more pronounced in the actuator transduction thermal responses than in the dielectric thermal responses of Figure 3.1. Furthermore, the maxima of the broad thermal phase transition appear shifted, when comparing the actuator transduction of Figure 3.3 with the dielectric response of Figure 3.1, from between 45°-50°C to between 25-30°C. The actuator transduction sensitivity described in these figures is equivalent to the d -coefficient for piezoelectrics; it is the ratio of induced strain to applied AC electric field.

The apparent shift in the phase transition maxima can be explained by the temperature dependence of the electrostrictive coefficient Q_{13} alluded to in Figure 1.20 (p. 44). The net effect of Q_{13} decreasing, as in Figure 1.20, while the dielectric constant increases to a maximum near 45°C, as in Figure 3.1 (p. 81), is that the maximum electrostrictive actuator transduction is shifted, compared to the maximum permittivity. Pronouncement of the frequency dependence of the actuator transduction sensitivity compared with the frequency dependence of the dielectric response can be explained by examining the LGD phenomenology of equation (1.18) on p. 48. By combining equations (1.3) and (1.18) and by ignoring initial conditions and neglecting contributions from the electrostrictive piezoelectric term, the free-induced strain,

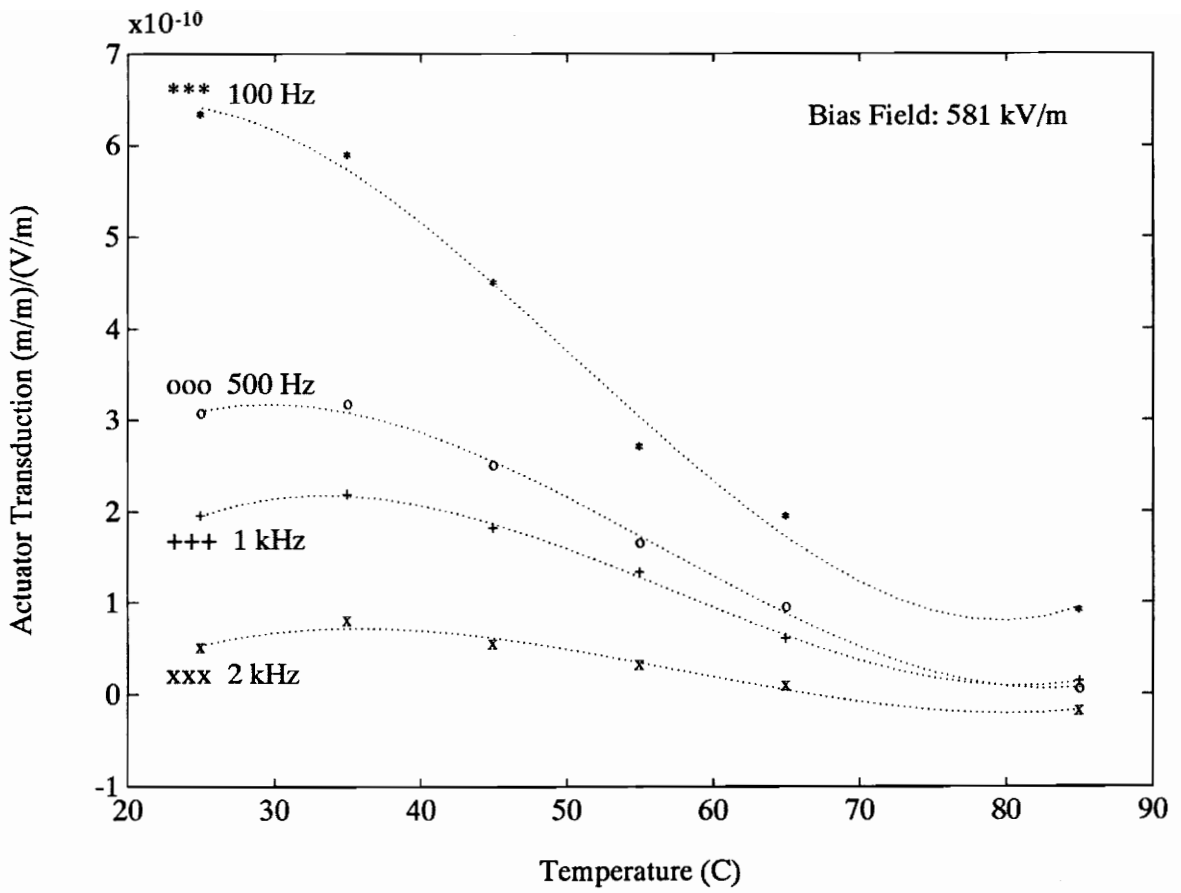


Figure 3.3 Actuator transduction sensitivity versus temperature for various frequencies at constant bias field.

$$\Lambda_i = Q_{ij}(\epsilon \chi_{jm} E_m)^2. \quad (3.1)$$

According to equation (1.7) on p. 29, the relative dielectric susceptibility and relative permittivity are practically identical for high permittivity materials like PMN-PT. In equation (3.1), free-induced strain varies with the square of relative susceptibility, thus the square of relative permittivity. Therefore, variation of dielectric properties due to frequency is more pronounced in the actuator strain transduction curves of Figure 3.3 than the dielectric responses of Figure 3.1. This variation is likewise evident in the frequency response plots of Figure 3.4, which contains results at a different bias field.

In Figure 3.4, the flat response of about 0.1×10^{-10} (m/m)/(V/m) at 85°C corresponds with the flat response for the 85°C dielectric permittivity curve of Figure 3.2 and relates to the introduction of paraelectric material phases. The frequency response plots of Figure 3.5, demonstrating bias-field dependence, have similar shapes to those of Figure 3.4. In both of these figures, the response levels out at higher frequencies. Both figures also indicate anomalous results between 400 and 600 Hz. In Table 2.1 (p. 68), values for the first bending mode of the experimental actuators are indicated. Since some curvature was noted for these specimens and since asymmetric material properties about the neutral axis were introduced by bonding strain gages, the apparent resonant/anti-resonant results between 400 and 600 Hz occur due to bending.

In Figure 3.5, the bias-field dependence of actuator transduction sensitivity is also introduced. Constant frequency plots in Figure 3.6 confirm this dependence and indicate

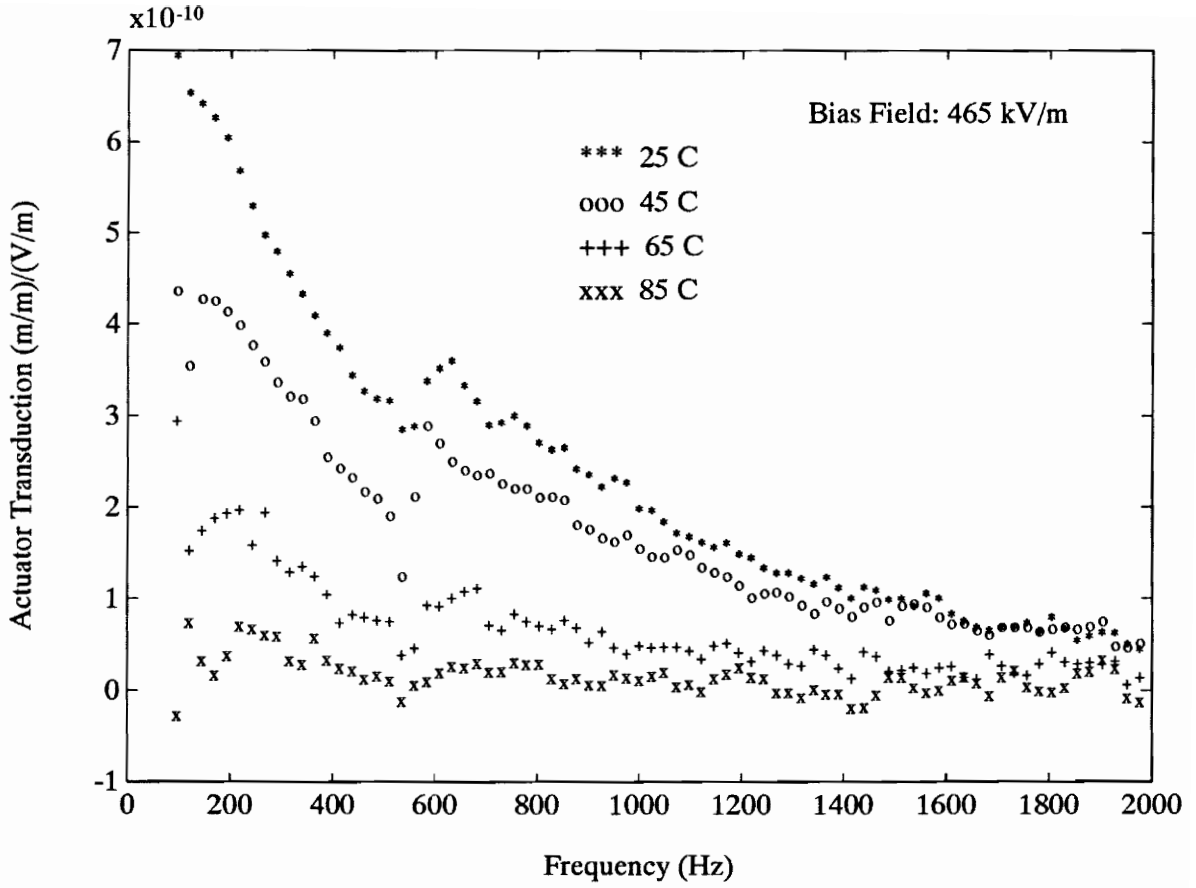


Figure 3.4 Frequency response of actuator transduction sensitivity for various temperatures at constant bias field.

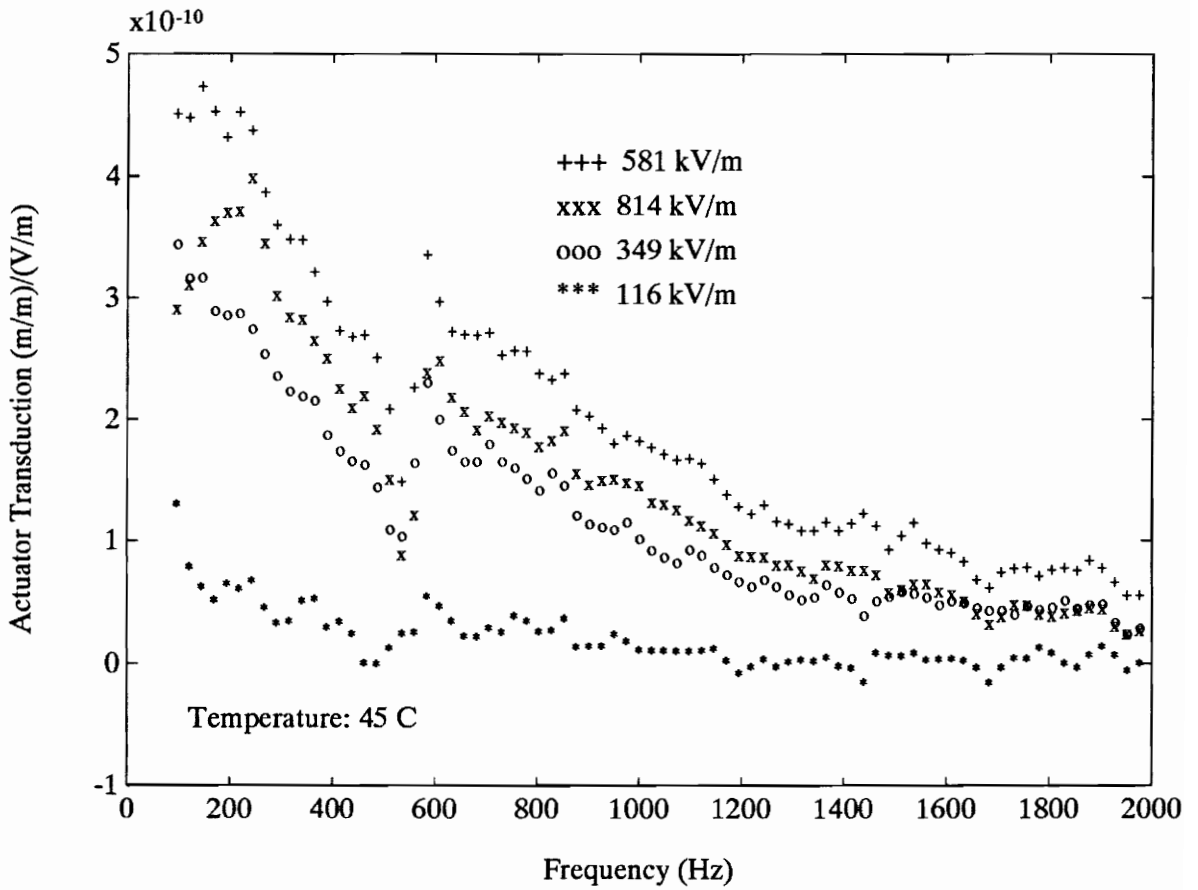


Figure 3.5 Frequency response of actuator transduction sensitivity for various bias fields at constant temperature.

a law of diminishing returns for the transduction sensitivity with respect to higher bias fields. For actuation studies, applied electric field was composed of a DC component, ranging to very large values of 814 kV/m, and a moderate AC component having an amplitude of at most 75 kV/m. If the electric field is algebraically separated into these two components and if the separate effects of field on the dielectric susceptibility are considered, equation (3.1) becomes, after assuming unidirectional field and considering only the transverse strain component,

$$\Lambda_1 = Q_{13} \epsilon_o^2 [(\chi_{33}^{DC} E_3^{DC})^2 + 2\chi_{33}^{DC} E_3^{DC} \chi_{33}^{AC} E_3^{AC} + (\chi_{33}^{AC} E_3^{AC})^2]. \quad (3.2)$$

Actuator transduction sensitivity represents the free strain induced by AC field, or the partial derivative of equation (3.2) with respect to E_{AC} ,

$$\frac{\partial \Lambda_1}{\partial E_3^{AC}} = 2Q_{13} \epsilon_o^2 [\chi_{33}^{DC} \chi_{33}^{AC} E_3^{DC} + (\chi_{33}^{AC})^2 E_3^{AC}]. \quad (3.3)$$

In equation (3.3), both AC and DC components contribute to the actuator transduction. The AC component is constant, except for frequency dependence, so that for each constant frequency plot in Figure 3.6, the DC, or bias field, component evokes change in the sensitivity. According to equation (3.3), a rise in DC field will increase the transduction sensitivity; however, as shown in Figure 1.15 (p. 37), decreased permittivities (susceptibilities) accompany increased bias fields, so that the net effect on actuator transduction is the peak demonstrated by data of Figure 3.6. Frequency effects on the AC permittivity demonstrate shifts in the bias field associated with maximum transduction and variation in transduction amplitudes.

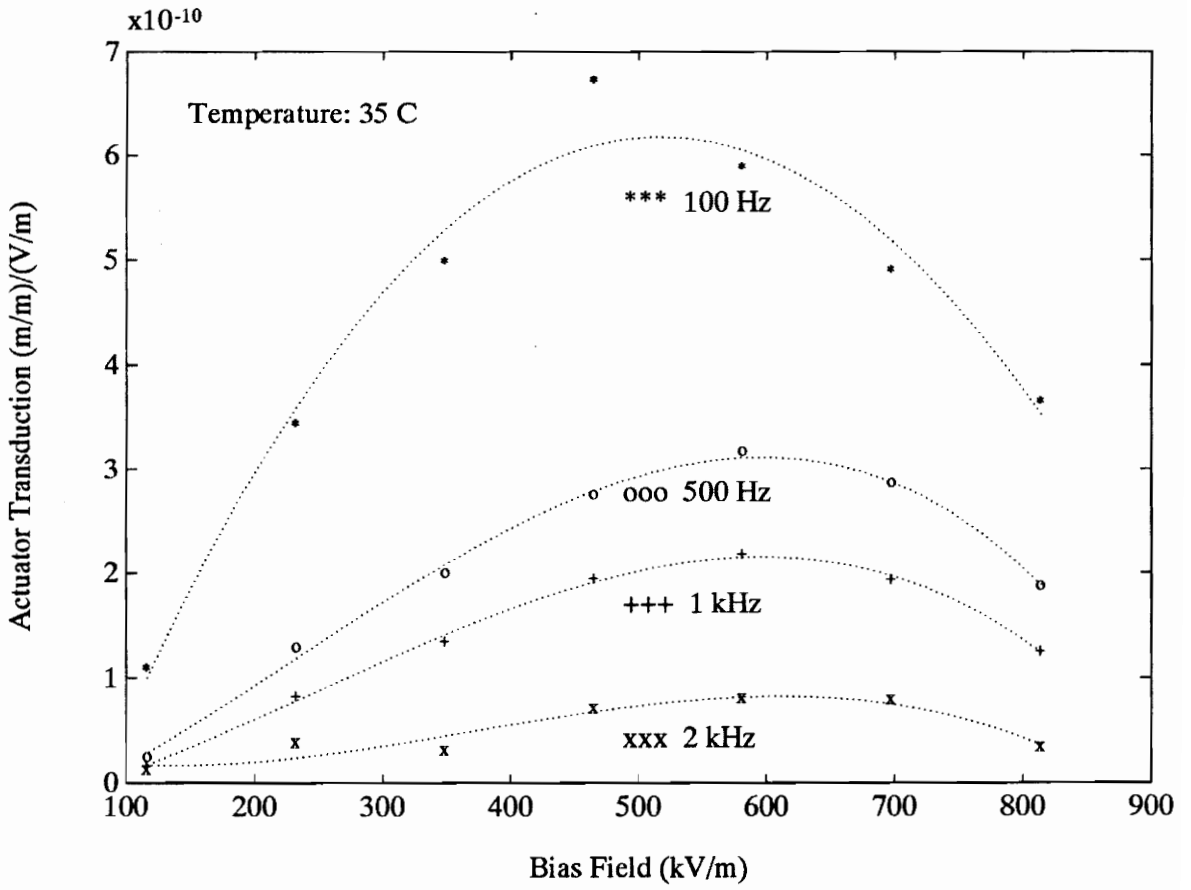


Figure 3.6 Actuator transduction sensitivity versus bias field for various frequencies at constant temperature.

Thermal considerations for bias-field-dependent actuator transduction results are typified by the plots of Figure 3.7. For temperatures above T_{max} , the paraelectric phase dominates behavior, such that the relaxor ferroelectric effects of reversible polarization and direct electrostriction are not revealed until very high fields, at which remaining ferroelectric phases are field-excited enough to induce aggregate strain. Beneath T_{max} , the electrostrictive actuator specimens exhibit different bias-field response shapes and maxima at different temperatures.

Finally, the sixth permutation in the temperature-frequency-bias field co-dependent, direct electrostrictive behavior of PMN-PT is illustrated by the varying bias-field plots in the thermal responses of Figure 3.8. Shape changes of the thermal responses through the phase transition due to bias field differences result from the effective interactions between the bias-field dependent permittivity and the bias field itself. Examination of equation (3.3) indicates that actuator transduction sensitivity relies on this interaction. Data displayed for all dynamic actuation tests represent specimen averages, ranging in standard deviation from 5×10^{-13} to 8×10^{-11} (m/m)/(V/m).

As described in Chapter 2, DC actuation tests were also performed with PMN-PT specimens. Results from these investigations are plotted in Figure 3.9, whose data represent averages consisting of standard deviations between 0 and $20 \mu\text{m/m}$. In Figure 3.9, among the most noticeable characteristics is the decrease in hysteresis, which is considerably less than that of the more commonly used piezoelectric PZT, with increased

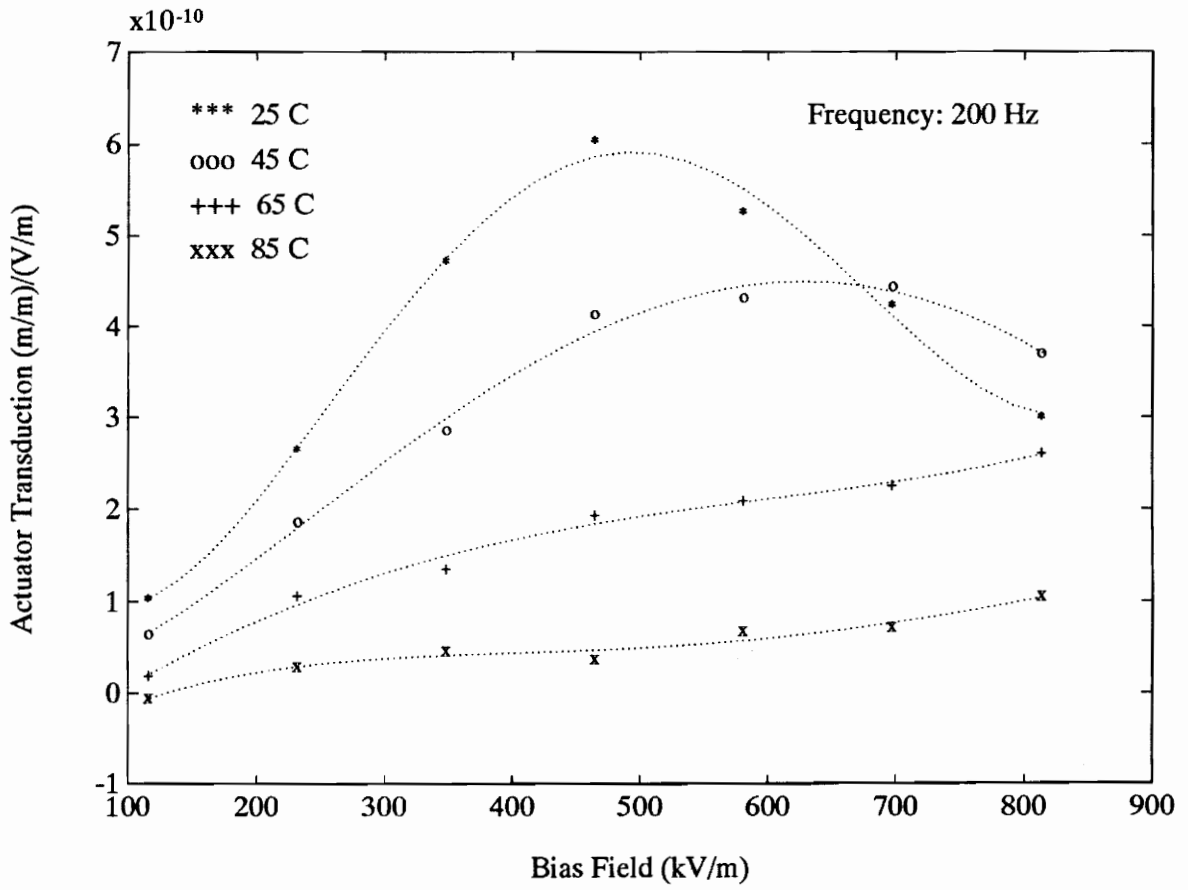


Figure 3.7 Actuator transduction sensitivity versus bias field for various temperatures at constant frequency.

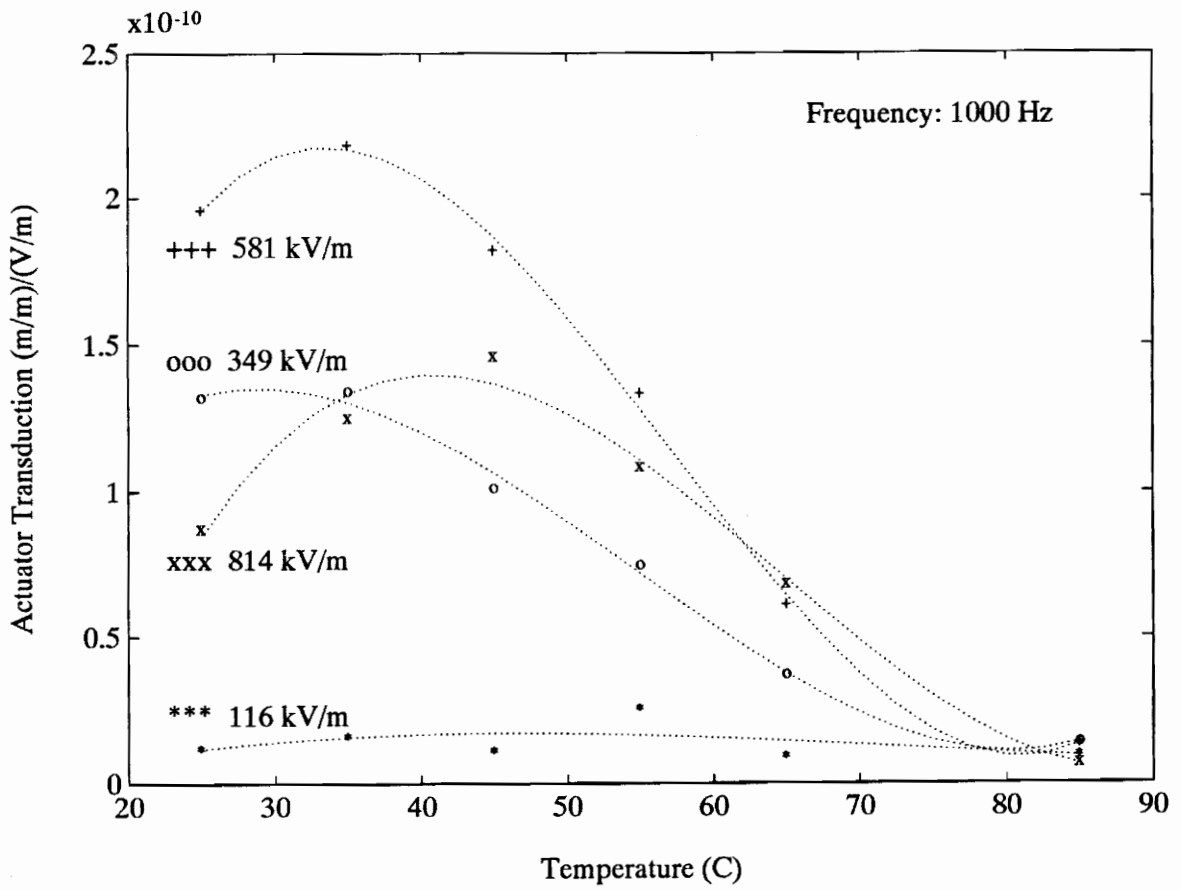


Figure 3.8 Actuator transduction sensitivity versus temperature for various bias fields at constant frequency.

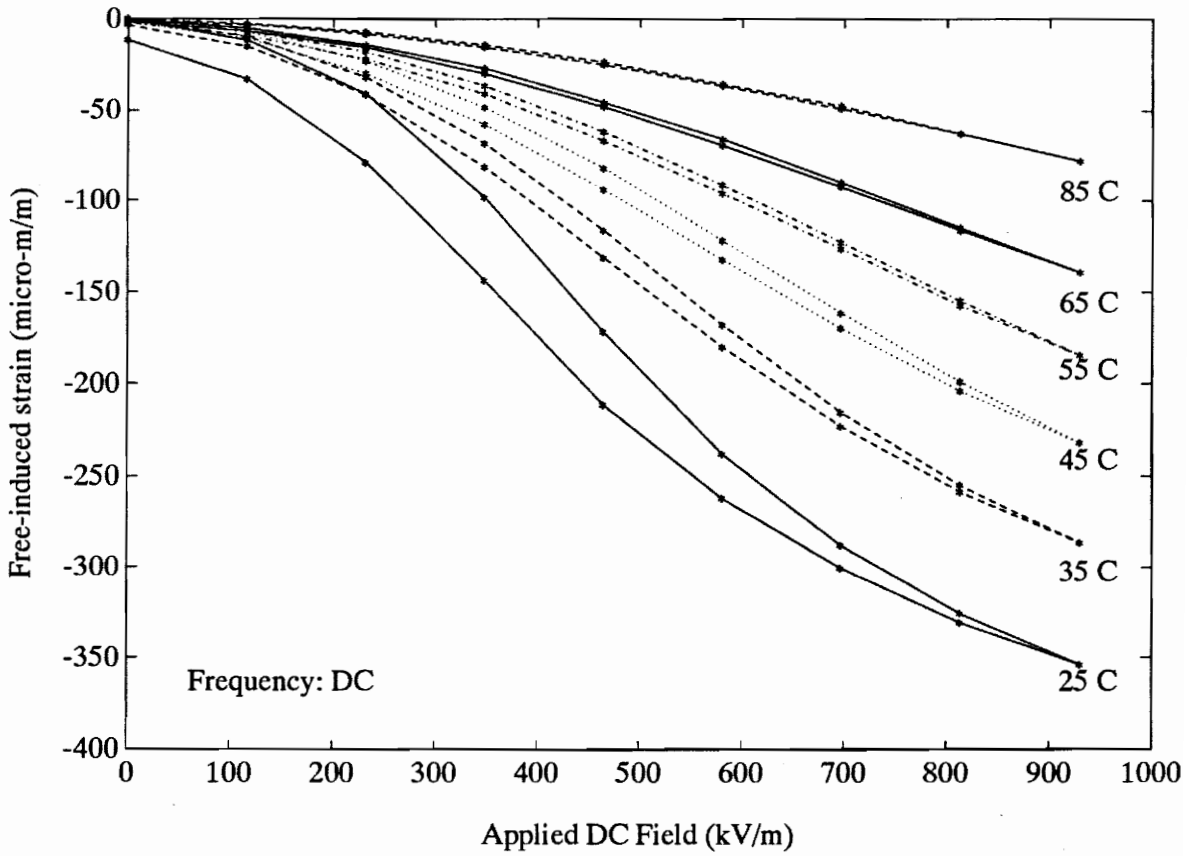


Figure 3.9 Free-induced strain resulting from the application of DC electric fields at various temperatures.

paraelectric material phase (higher temperatures). Another notable characteristic is the nonlinear, yet non-parabolic relation between applied DC field and induced strain.

According to equation (3.3), there is a quadratic relationship between applied field and induced strain; however, there is also a quadratic relationship between susceptibility and induced strain. As described above, the net effect of the product of the square of a permittivity declining with applied field and the square of that field appears in the shapes of the curves in Figure 3.9. As introduced in equation (1.22) and Figure 1.22 on pp. 49-50, the ferroelectric relation between polarization and electric field can be described using a hyperbolic tangent phenomenological model introduced by Zhang and Rogers (1992). The results from and implications of using this model are reserved for discussion in Chapter 4.

3.3 Sensing Results

Results from the sensor experiments with PMN-PT specimens described in Chapter 2 are graphed in Figures 3.10 and 3.11. Differences between using PMN-PT as a sensor and as an actuator are readily apparent in these figures. One noticeable difference is that the frequency responses for the PMN-PT sensors between 0 and 500 Hz are flat, compared with the responses of Figures 3.4 and 3.5 for PMN-PT actuators. The shape of plots in Figures 3.4 and 3.5 are readily explained by the shapes of responses in Figure 3.1 for the dielectric permittivity, a constituent of PMN-PT transduction. The difference in Figure 3.10 is a consequence of the relative levels of induced polarization. For the

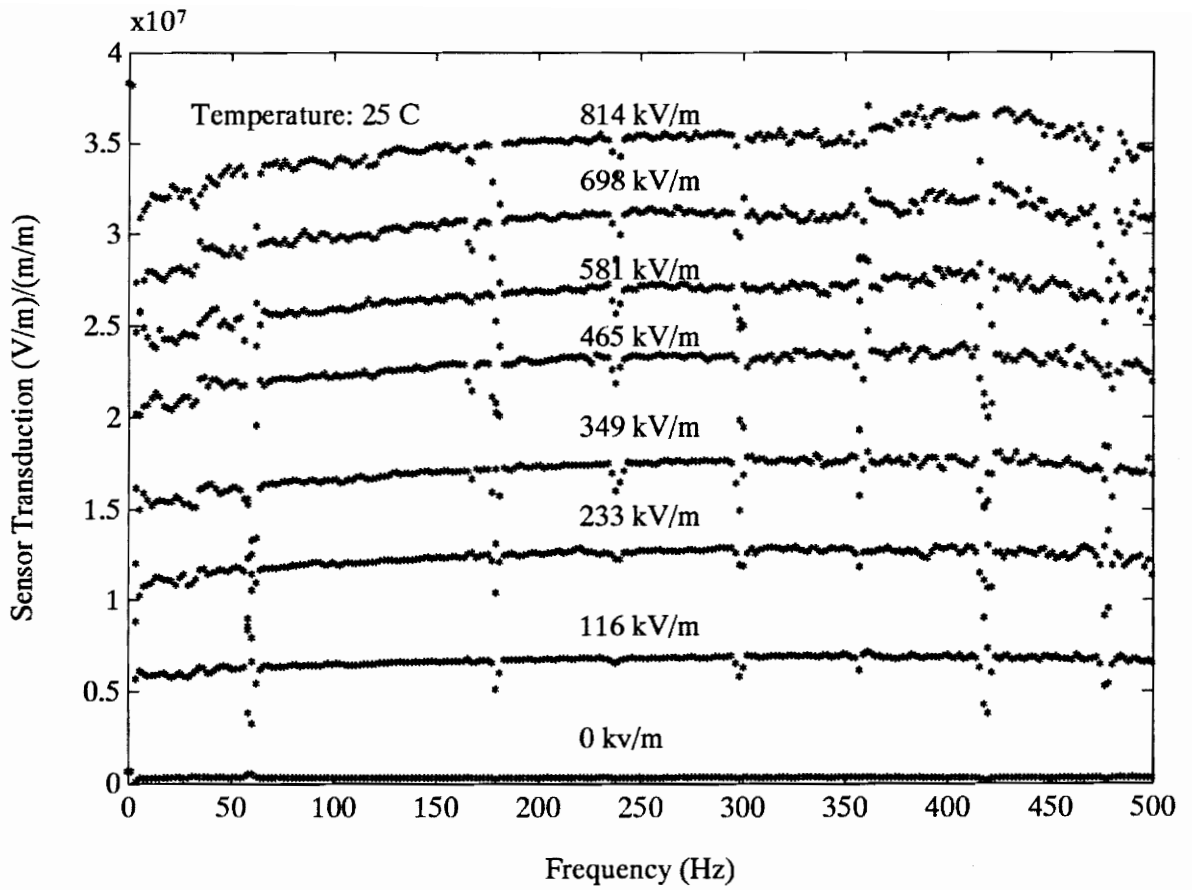


Figure 3.10 Frequency response of sensor transduction sensitivity at various temperatures.

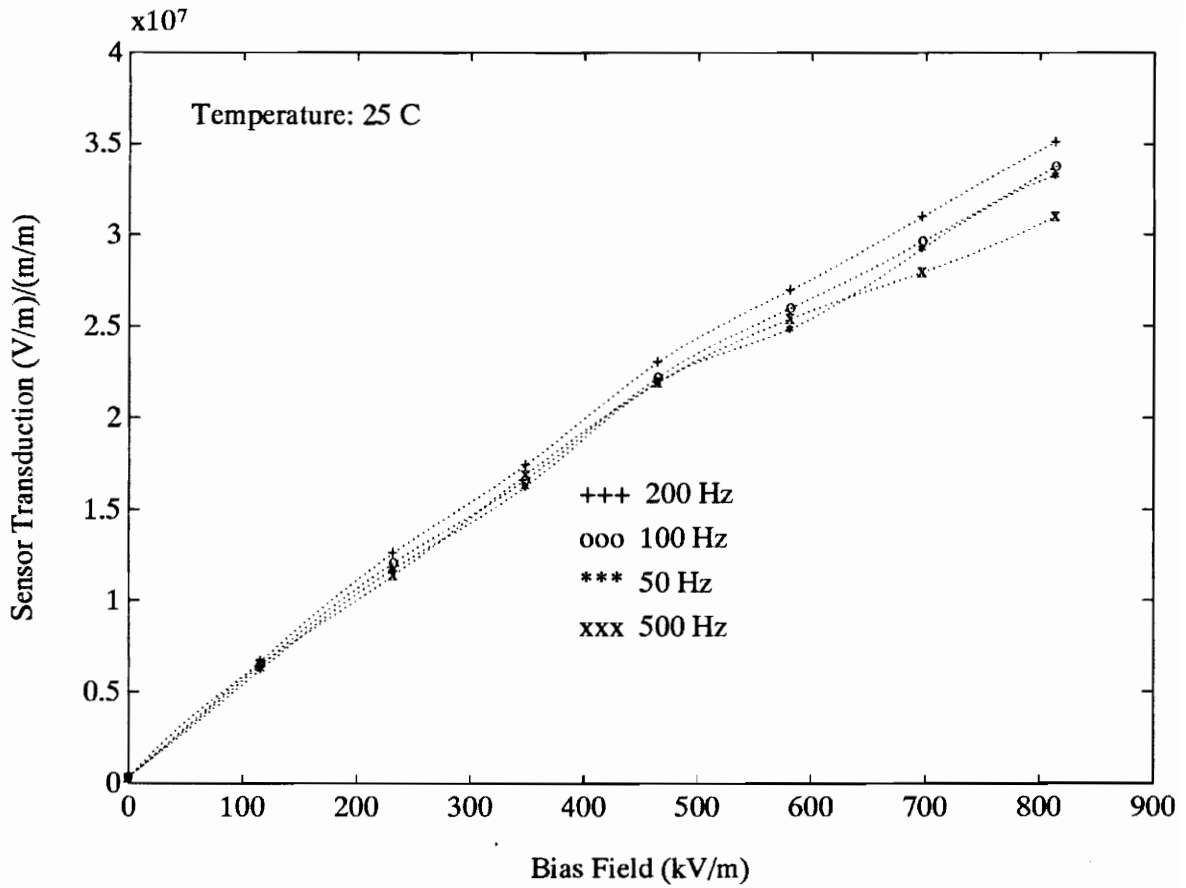


Figure 3.11 Sensor transduction sensitivity versus bias field for various frequencies.

dielectric and actuation studies, moderate levels of AC polarization were induced by electric fields; however, in the PMN-PT sensing studies, the stress-induced polarization levels were millionths-to-billionths of the other two. Because the swings in polarization magnitudes were far less during sensing tests, the frequency of these swings and its effect on dielectric properties were negligible, so that frequency responses appear flat.

The insignificant frequency effects on sensing transduction are again apparent in Figure 3.11, which indicates bias-field dependence. Sensing transduction represents a modified version of terms in the parentheses of equation (1.20) on p. 48, whose collection is equivalent to the piezoelectric g -coefficient. By assuming a linear, symmetric stress-strain law for PMN-PT and neglecting any feed-through or initial conditions represented by E^o , equation (1.20) can be rewritten,

$$E_i = [(Q_{ijk} P_k + g_{ij}^o) Y_{jm}] s_m. \quad (3.4)$$

The bracketed terms of equation (3.4) symbolize the sensor transduction sensitivity depicted in Figures 3.10 and 3.11.

The electrostrictive piezoelectric voltage coefficient g^o of equation (3.4) appears in Figure 3.11 as non-zero transduction values for zero applied bias field. The nonlinearity of the curves of Figure 3.11 arises from P-E nonlinearity. According to LGD phenomenology of equation (3.4), sensor transduction is linearly related to applied polarization. Since electric bias field of the abscissa of Figure 3.11 is used to induce that polarization, the nonlinearity, as previously alluded for other tests, must result from the nonlinear electric

field-polarization relations, which is a subject of the next chapter.

3.4 Grain Size Results

A typical result from SEM studies of the cross-sectional surface of a fractured PMN-PT sample is illustrated in the micrograph of Figure 3.12. Figure 3.12 shows that the sample is composed of hexagonal-shaped grains, whose appearance is a good indication of a material with a low thermal expansion coefficient, as is the case for PMN-PT. Inclusions and voids are evident in the SEM micrograph.

An average grain size, calculated using the intercept method, was determined from such micrographs to be $4.1 \mu\text{m}$, with a standard deviation of $0.4 \mu\text{m}$. Since PMN-PT is a solid solution, the grain size represents an average for grains composed of lead magnesium, lead niobate, and lead titanate. For this reason, the standard deviation represents a rather large percentage of the average, around 10%. Nevertheless, results for the 0.9PMN-0.1PT specimens used in this study compare well with 0.93PMN-0.07PT samples prepared by Shrout et al. (1987), whose results are listed in Table 1.1 (p. 54).

The samples used in this study, prepared by AVX Corporation, were sintered at 1300°C . Results in Figure 3.1 indicate that a maximum 100-Hz permittivity of around 21,500 occurs near 47.5°C . In Table 1.1, the maximum permittivity for a 0.93PMN-0.07PT sample fired at 1300°C is 21,000. Grain sizes compare reasonably well, for Shrout shows a $6 \mu\text{m}$ size for his 1300°C sample. The largest difference between present results

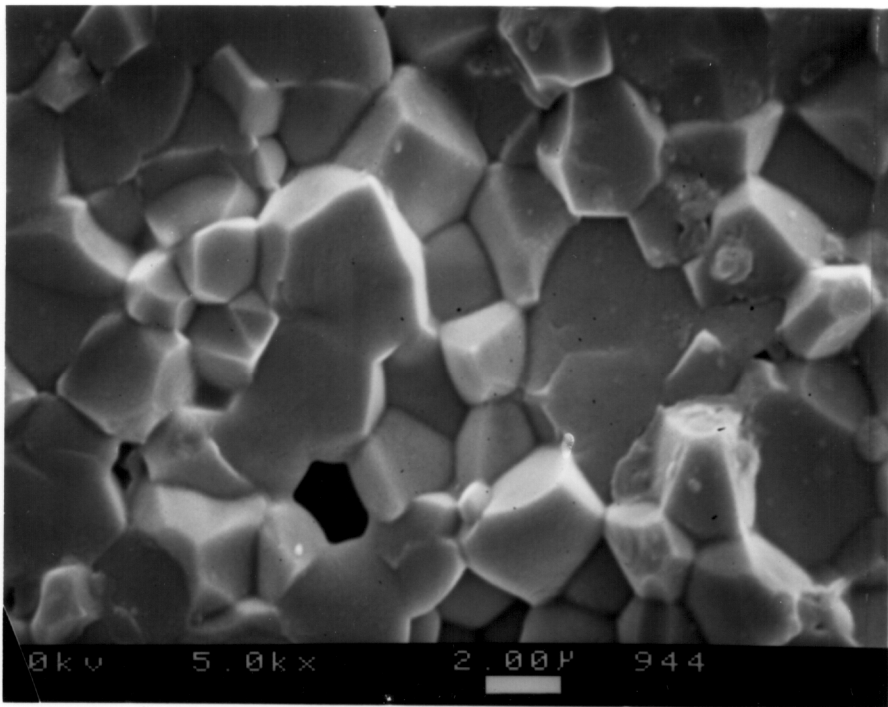


Figure 3.12 SEM micrograph of fractured PMN-PT surface.

and those of Table 1.1 is in the T_{max} , 47.5°C and 18.7°C, respectively. This difference is solely the consequence of dissimilar solid solution compositions, where larger concentrations of PMN result in lower values of T_{max} .

For example, according to Swartz et al. (1984), PMN without any PT dopant has a maximum permittivity at around -15°C. Additionally, the grain size difference between 0.93PMN-0.07PT and 0.9PMN-0.1PT samples having comparable maximum permittivities can be attributed to higher concentrations of lead titanate. In fact, a comparison of results from Swartz, ShROUT, and this study indicates that PT additions lower the average grain size while increasing both ϵ_{max} and T_{max} , as indicated in Table 3.1.

The purpose for determining a grain size for PMN-PT samples investigated for dielectric, sensing, and actuation properties was to ascertain how grain size interrelates to composition and properties. In Table 3.1, correlations with composition are most apparent; moreover, data from Table 1.1 and results from ShROUT et al. (1987) must be utilized to understand the implications of grain size on dielectric properties and modeling. Chapter 4 begins with the analysis of model parameters introduced by ShROUT.

Table 3.1 Macro compositional effects on some properties of PMN-PT fired at 1300°C.

| Composition | Grain Size (μm) | ϵ_{max} [100 Hz] | T_{max} [100 Hz] (°C) |
|-----------------|---------------------------------|------------------------------|-------------------------------|
| PMN* | 8.9 | 16,400 | -16 |
| 0.93PMN-0.1PT** | 6 | 21,000 | 18.7 |
| 0.9PMN-0.1PT | 4.1 | 21,500 | 47.5 |

* Swartz et al. (1984)

** Shrout et al. (1987)

Chapter 4

Analysis and Modeling

The objective to this point has been to experimentally establish dielectric and electrostrictive behaviors of PMN-PT. In this chapter, the ultimate objective for this research, to develop a model which can be used for the electro-mechanical design of intelligent material systems which incorporate PMN-PT electrostrictors, will be fulfilled. As alluded in quotes of the summary of Chapter 1, it is nearly impossible to theoretically account for the precise behaviors of electroceramics. For this reason, an empirical approach to modeling has been undertaken. The chapter begins where Chapter 3 left off, by analyzing and modeling the grain size relations to dielectric properties. A model for the diffuse phase transition behavior is derived from this analysis and from formulations introduced in Chapter 1. Frequency dispersion of dielectric properties is considered in this model. Next, effects of bias field on permittivity are examined and modeled, and the impact of frequency on electrostrictive properties is appraised. The chapter concludes with model results and a procedural summary for modeling PMN-PT electromechanical behavior.

4.1 Grain Size and Phase-dependent Dielectric Behavior

Chapter 3 ended with discussion of grain size and its connection to PMN-PT relaxor

dielectric parameters such as the maximum permittivity and its corresponding temperature. Results from the 0.9PMN-0.1PT specimens of this study were compared to 0.93PMN-0.07PT specimens explored by ShROUT et al. (1987). In his investigations, ShROUT proposed relations between grain size and dielectric properties but failed to develop mathematic models to describe those proposals. Although ShROUT's research involved a different solid solution composition, data from his studies can be analyzed to develop mathematic models which associate grain size with dielectric parameters.

ShROUT aptly suggested that dielectric properties are functions of both processing history (firing temperatures, times) and grain size; however, grain size will be solely considered to simplify models. In fact, as indicated by data for 1250°C-fired specimens in Table 1.1 (p. 54), the grain-size parameter can reflect both processing time and temperatures. Models for grain-size dependence of T_{max} and ϵ_{max} are based on least-mean-square algebraic regression analysis of data from Table 1.1, which represent information about 0.93PMN-0.07PT at a single frequency $\omega_o = 100$ Hz:

$$T_{max}(\omega_o) = \sum_{i=0}^N \tau_i \gamma^i \quad (4.1)$$

$$\chi_{max}(\omega_o) \approx \epsilon_{max}(\omega_o) = \sum_{i=0}^N X_i \gamma^i \quad (4.2)$$

In Figures 4.1 (a) and (b), data from Table 1.1 is compared with models of equations (4.1) and (4.2), respectively. In both cases, the algebraic relations are second-order (N

= 2), where $\tau_0 = 299$ K, $\tau_1 = -1.92$ K/ μm , $\tau_2 = 0.120$ K/ μm^2 , $X_0 = 6700$, $X_1 = 3600/\mu\text{m}$, and $X_2 = -204/\mu\text{m}$ for the 0.93PMN-0.07PT data. Scatter about the model curves in Figures 4.1 (a) and (b) represent the aforementioned processing effects. Evident in these plots, however, is that for larger grain sizes, processing effects are built into the grain size number, so that there is little scatter at these values.

Shrout et al. (1987) advanced a mathematic model for the diffuse phase transition behavior prevalent in the thermal response of relaxor ferroelectric permittivity by drawing analogy to the Curie-Weiss law of equation (1.13) for ferroelectric phase transition and by observing the Gaussian distribution of permittivity with respect to temperature. In equation (1.23), Shrout introduced a diffuseness coefficient, relating the thermal distribution of permittivities, and associated this coefficient with the maximum permittivity. Again, no mathematic model was developed. From Table 1.1, the nature of this relationship is linear,

$$\lambda = \sum_{i=0}^{N=1} L_i \epsilon_{\max}(\omega_o) = \sum_{i=0}^{N=1} L_i \chi_{\max}(\omega_o). \quad (4.3)$$

Data from Table 1.1 and results for the least-mean-square regression for equation (4.3) are plotted in Figure 4.1 (c), where $L_0 = 344$ K and $L_1 = -0.00146$ K for the 0.93PMN-0.07PT data.

From Shrout's relation of equation (1.23), the thermally dependent relative permittivity,

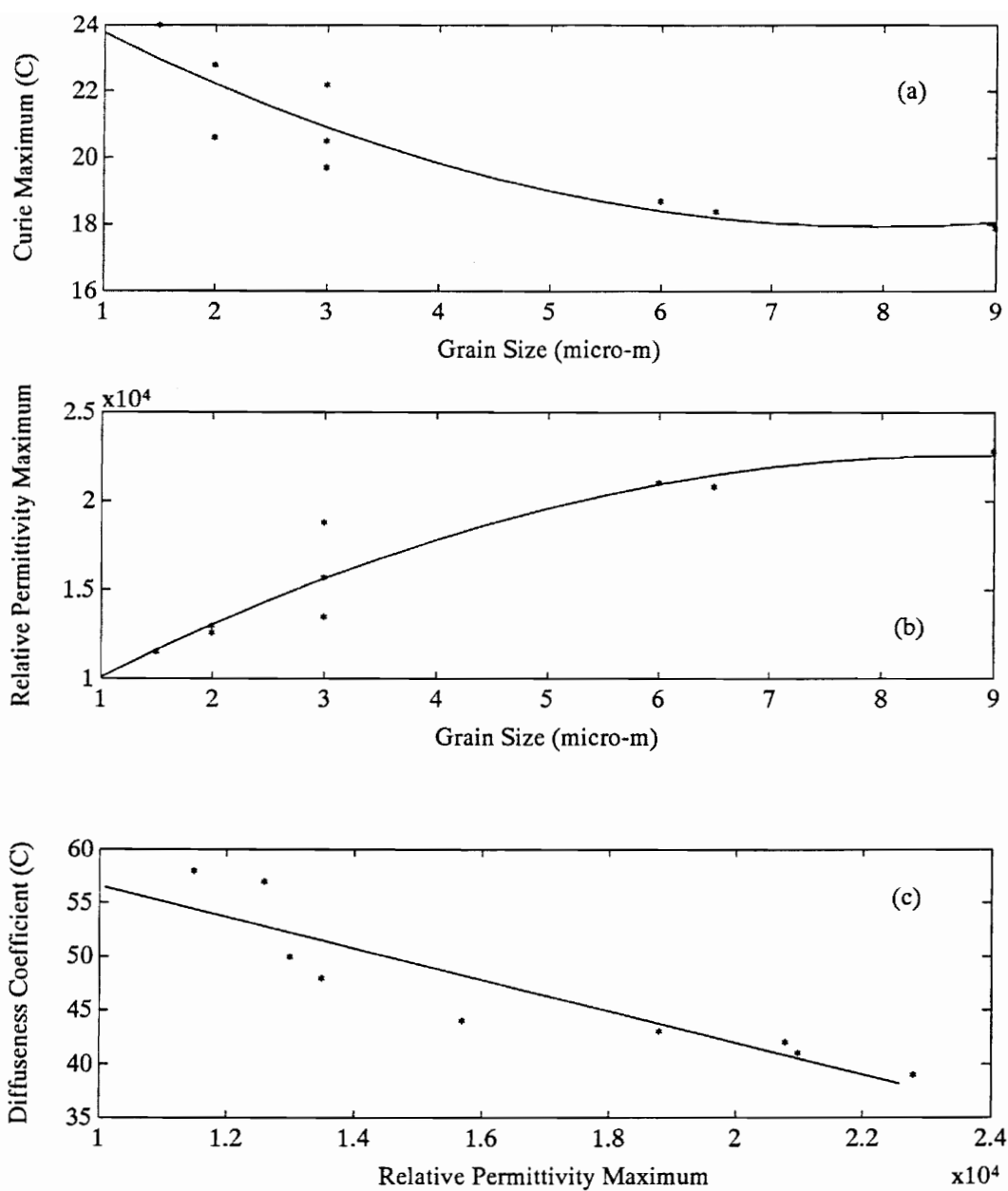


Figure 4.1 Comparison of models with 0.93PMN-0.07PT data for (a) Curie maximum temperatures and (b) maximum permittivities versus grain size and for (c) Shrou's diffuseness coefficient versus maximum permittivity (data after Shrou et al., 1987).

$$\epsilon'(T) = \frac{2\epsilon_{\max}\epsilon_m\lambda^2}{2\epsilon_m\lambda^2 + \epsilon_{\max}[T - T_{\max}]^2}. \quad (4.4)$$

Equations (4.1) through (4.3) provide models for the parameters T_{\max} , ϵ_{\max} , and λ that can all be related to grain size. The only parameter unrealized for the model of equation (4.4) is ϵ_m . No data exist in Table 1.1 to relate ϵ_m to grain size. Regardless, this constant, which represents the integrated mean of relative permittivity across the phase transition, can be determined through equation (4.4) by measuring the permittivity at one temperature, for example 25°C. Thus, the permittivity phase transition (at a given frequency) of a solid solution of PMN-PT can be modeled with equation (4.4) by measuring grain size and permittivity at one temperature.

For the 0.9PMN-0.1PT data of the present experimental study, represented by Figure 3.1, the model of equation (4.4) compares well to data up to and just past the Curie maximum, as shown in Figure 4.2. Values of model parameters for this plot include $T_{\max} = 47.5^\circ\text{C}$ and $\epsilon_{\max} = 21500$, from the 100-Hz data of Table 3.1, and $\lambda = 27^\circ\text{C}$ and $\epsilon_m = 14500$. The Gaussian nature of the model dictates that the distribution be symmetric about the Curie maximum temperature, which is not the case for PMN-PT data of Figures 4.2, 3.1, and 1.13. Although the quadratic, Gaussian model of equation (4.4) represents behavior very well for ferroelectric phases of the thermal transition, the linear, paraelectric behavior past the Curie maximum is not well-modeled. Furthermore, frequency dispersion of permittivity is not incorporated. Both of these problems are the subject of the next section.

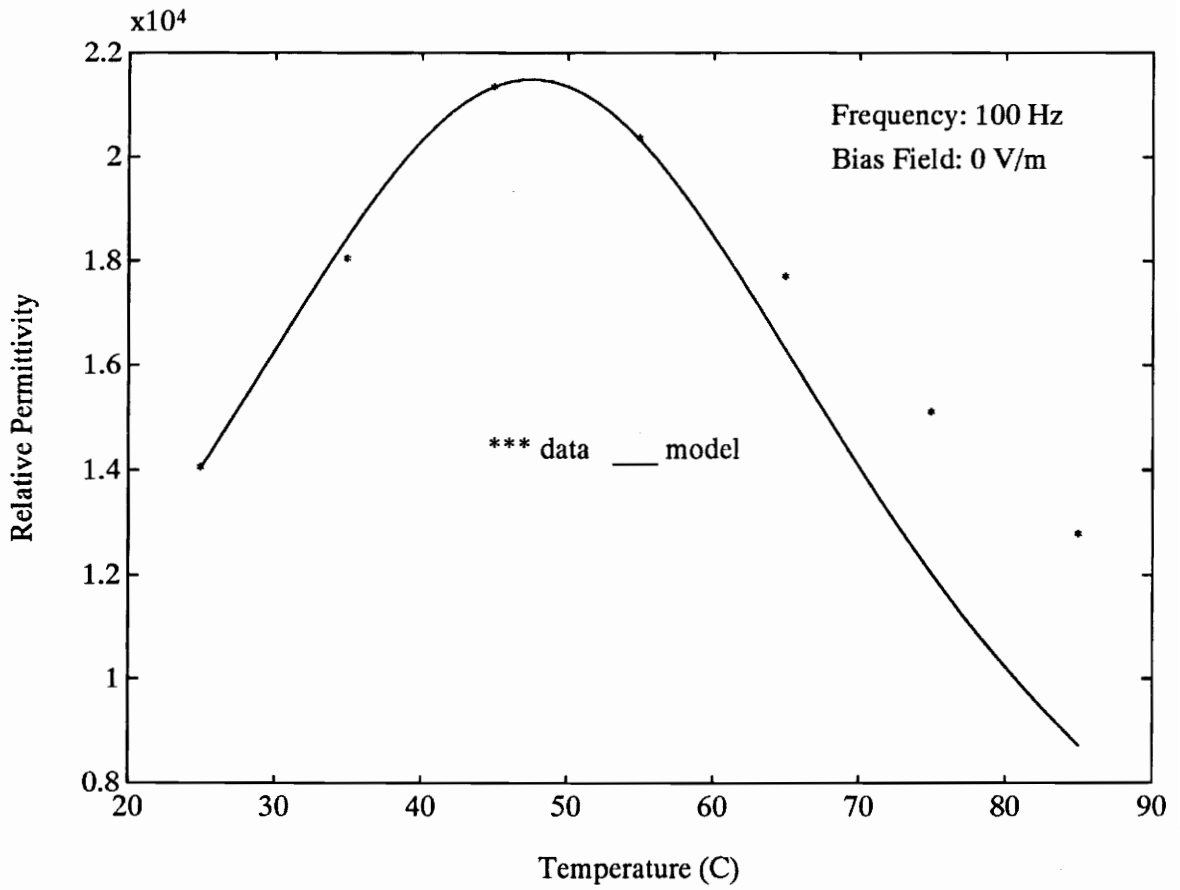


Figure 4.2 Comparison of Shroul's dielectric phase transition model with experimental data.

4.2 Frequency Dispersion of Dielectric Properties

In addition to the insufficiency of representing permittivities past the Curie maximum temperature, the model of equations (1.23) and (4.4) neglects a major contributor to the dielectric response, frequency. Frequency-dependence is prevalent in the experimental results of Figures 3.1 and 3.2 (pp. 80-81). From these curves, one can surmise that the parameters of equation (4.4)— T_{max} , ϵ_{max} , and ϵ_m —vary with frequency. Viehland et al. (1990) observed the similarities of the microscopic compositional fluctuation behavior of relaxor ferroelectrics to the spin-glass behavior of superparamagnetic relaxors and derived the spin-glass-analogous model of equation (1.24) on p. 56, which indicates frequency dependence of T_{max} . In this equation, Viehland proposed a logarithmic relation between the Curie maximum and frequency, supported by experimental data. As noted in Chapter 3, the experimental frequency response of isothermal permittivities also varies linearly with respect to the logarithm of frequency.

In this vein, the Curie maximum and maximum relative permittivity (thus, susceptibility) are proposed as functions of the logarithm of frequency:

$$T_{max}(\omega) = T_{max}(\omega_o) + \tau_{max} \ln(\omega_o/\omega) \quad (4.5)$$

$$\chi_{max}(\omega) = \chi_{max}(\omega_o) + X_{max} \ln(\omega_o/\omega). \quad (4.6)$$

With respect to the model of equation (4.4), three of the four parameters necessary to determine the relative permittivity at a given frequency and temperature are modeled by equations (4.1), (4.2), (4.3), (4.5) and (4.6). In these models, the diffuseness coefficient

is a constant which depends solely on grain size (via χ_{max}).

The remaining parameter, ϵ_m or χ_m , can be determined from the other three and from a known relative susceptibility at a known temperature. However, χ_m will certainly vary with frequency, since it represents an integral mean of susceptibility. To account for this probable frequency dependence, a logarithmic relation similar to those of equations (4.5) and (4.6) is proposed:

$$\chi(T_o, \omega) = \chi(T_o, \omega_o) + X \ln(\omega_o / \omega), \quad (4.7)$$

where $\chi(T_o, \omega_o)$ is a measured susceptibility at a known temperature and interrogation frequency. Again, only the grain size number and one susceptibility measurement are required to use this frequency-dispersive, dielectric phase transition model.

The problem of accuracy for increased paraelectric phase temperatures still remains with the model of equation (4.4), upon which everything is based. In Figures 4.2 and 3.1, these permittivities (susceptibilities) seem to be linearly related to temperature. However, this linear relationship begins at temperatures somewhat past the Curie maximum. Empirically, the onset of linear thermal-permittivity variance occurs at a temperature about 10% greater than the maximum Curie temperature, which is frequency dependent. From equation (4.4) and from these empirical observations, the AC susceptibility can be described by the following equations:

$$T \leq 1.1 T_{max}(\omega),$$

$$\chi^{AC}(T, \omega) = \frac{2\chi_{max}(\omega)\chi_m(\omega)\lambda^2}{2\chi_m(\omega)\lambda^2 + \chi_{max}(\omega)[T - T_{max}(\omega)]^2} \quad (4.8)$$

$$T > 1.1 T_{max}(\omega),$$

$$\chi^{AC}(T, \omega) = \chi^{AC}(1.1T_{max}(\omega), \omega) + X_{AC}[T - 1.1T_{max}(\omega)]. \quad (4.9)$$

By implementing equations (4.5)-(4.7) and presuming $T_o \leq 1.1 T_{max}(\omega_o)$, the term $\chi_m(\omega)$ can be determined, as described above, from the following expression:

$$\chi_m(\omega) = \frac{\chi(T_o, \omega)\chi_{max}(\omega)[T_o - T_{max}(\omega)]^2}{2\lambda^2[\chi_{max}(\omega) - \chi(T_o, \omega)]}. \quad (4.10)$$

Results from this complete frequency-dispersive, dielectric phase transition model are compared with experimental data in Figure 4.3. Model results were generated using the following constants: $T_o = 25^\circ\text{C}$, $\omega_o = 100 \text{ Hz}$, $T_{max}(\omega_o) = 47.5^\circ\text{C}$, $\tau_{max} = -1.3^\circ\text{C}$, $\chi_{max}(\omega_o) = 21500$, $\chi(T_o, \omega_o) = 14063$, $X_{max} = 400$, $X = -532$, $X^{AC} = -255$, and $\lambda = 27^\circ\text{C}$.

The frequency-dispersive, dielectric phase transition model embodied by equations (4.8) and (4.9) has been developed so that only two measurements are required, grain size and permittivity at a known temperature and frequency. With grain size, $T_{max}(\omega_o)$, $\chi_{max}(\omega_o)$, and λ can be determined using equations (4.1) through (4.3), respectively. With these values, $T_{max}(\omega)$ and $\chi_{max}(\omega)$ can be ascertained using equations (4.5) and (4.6). The measurement of relative susceptibility at known temperature and frequency is required

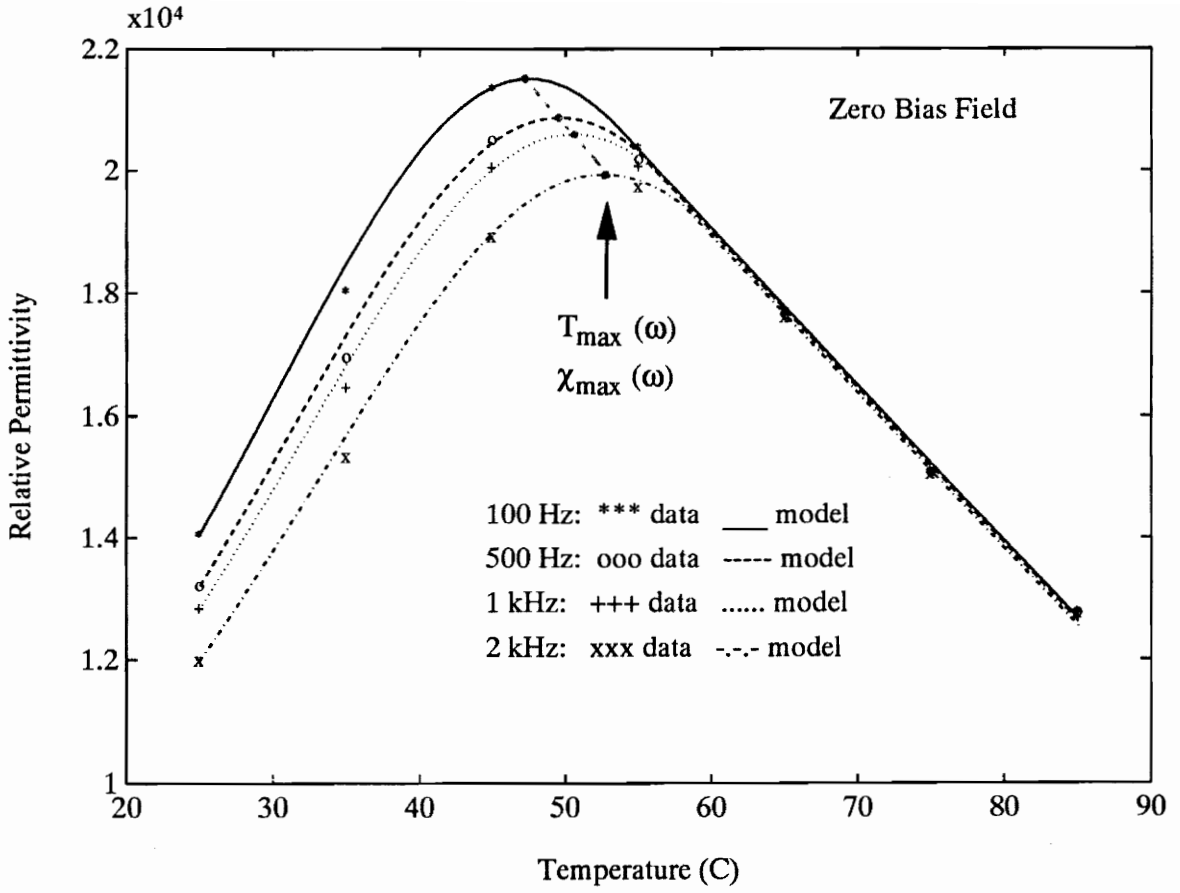


Figure 4.3 Comparison of frequency-dispersive, dielectric phase transition model with experimental data.

to complete the models of equations (4.7) and (4.10), for $\chi(T_o, \omega)$ and $\chi_m(\omega)$, respectively. Finally, the AC relative susceptibility with respect to both frequency and temperature, within the phase transition region, can then be obtained using equations (4.8) and (4.9).

4.3 Bias Field Considerations

Experimental results in Chapter 3 for PMN-PT actuation indicate that applied DC electric bias field contributes significantly to the electrostrictive response of PMN-PT. Equations (3.3) and (3.4) on pp. 88 and 97, based on the LGD phenomenology of equations (1.18) and (1.20) on p. 48, indicate direct influences of DC bias field on transduction sensitivities. Additionally, Pan et al. (1989) suggest an influence of bias field on dielectric properties and support this assertion by the experimental findings of Figure 1.15 (p. 37).

Zhang's and Rogers' (1992) proposed hyperbolic tangent relation for polarization, expressed in equation (1.22) for relatively anhysteretic relaxor ferroelectrics, attempts to model the nonlinear polarization-electric field (P-E) coupling. In Figure 1.22, Zhang's mathematic model fits experimental data for different solid solution compositions of PMN-PT very well. DC actuation investigations described in Chapters 2 and 3 also provide a means for evaluating the expression of equation (1.22) with experimental data from the present study. Although indirect, the P-E relation of equation (1.22) can be compared with free-induced strain data from DC actuation experiments by assimilating it into the LGD phenomenology of equation (1.18):

$$\Lambda_1(E^{DC})=Q_{13}[P^s \tanh(kE_3^{DC})]^2, \quad (4.11)$$

To evaluate equation (4.11), values for the electrostrictive coefficient, the saturation polarization, and the hyperbolic tangent polarization model coefficient must be known. None of these values have been obtained from analysis of the experiments of Chapters 2 and 3. Moreover, there is evidence in Figure 1.21 that the electrostrictive coefficient can vary with bias field. Nevertheless, properties have been determined for 0.9PMN-0.1PT compositions with similar processing histories to the specimens herein investigated. Values for the PMN-PT electrostrictive coefficients in Figures 1.20 and 1.21 vary less than ten percent with respect to temperature and bias field, so a constant value of about $Q_{13} = -0.008 \text{ m}^4/\text{C}^2$ was chosen for the present analyses.

Approximate values for saturation polarization and the hyperbolic tangent polarization model coefficient obtained from results in Figure 1.22 (c) can be used; however, since Q_{13} does not vary greatly with temperature, it appears that either P^s or k must vary thermally, based on a comparison of equation (4.11) and Figure 3.9. Because the shapes of different isothermal plots vary with respect to bias field, it is more likely that k , not the scaling factor P^s of equation (4.11), changes with temperature. A value for the saturation polarization, $P^s = 0.23 \text{ C/m}^2$, and an algebraic expression for the hyperbolic tangent model coefficient temperature dependence,

$$k(T)=\sum_{i=0}^{N=2} k_i T^i, \quad (4.12)$$

have been chosen for comparison of DC actuation data with results from equation (4.11).

Free-induced-strain results from experiments and from the model of equations (4.11) and (4.12) are compared in Figure 4.4. Values for Q , P^s , and k as described above were used, where $k_0 = 3.694 \times 10^{-5}$ V/m, $k_1 = -2.008 \times 10^{-7}$ V/m-K, and $k_2 = 2.768 \times 10^{-10}$ V/m-K². These plots indicate that the hyperbolic tangent model for polarization fits present experimental data very well and can perhaps be relied upon for modeling bias field effects on relative dielectric susceptibility.

By comparing the P-E expression of equation (1.22) with that of the conventional equation (1.3), the hyperbolic tangent polarization model can be related to the relative dielectric susceptibility:

$$\chi^{DC}(T, E^{DC}) = \frac{P^s \tanh[k(T)E^{DC}]}{\epsilon_0 E^{DC}}. \quad (4.13)$$

To correlate this formulation with experimental DC actuation data for further analyses, it is necessary to derive an expression to reduce free-induced strain data in Figure 3.9, for example, to dielectric information. Based on the electrostrictive phenomenology of equation (3.1), the relative susceptibility realized from free-induced transverse strain,

$$\chi_{33}^{DC}(T, E_3^{DC}) = \sqrt{\frac{\Lambda_1(T, E_3^{DC})}{Q_{13} \epsilon_0^2 [E_3^{DC}]^2}}. \quad (4.14)$$

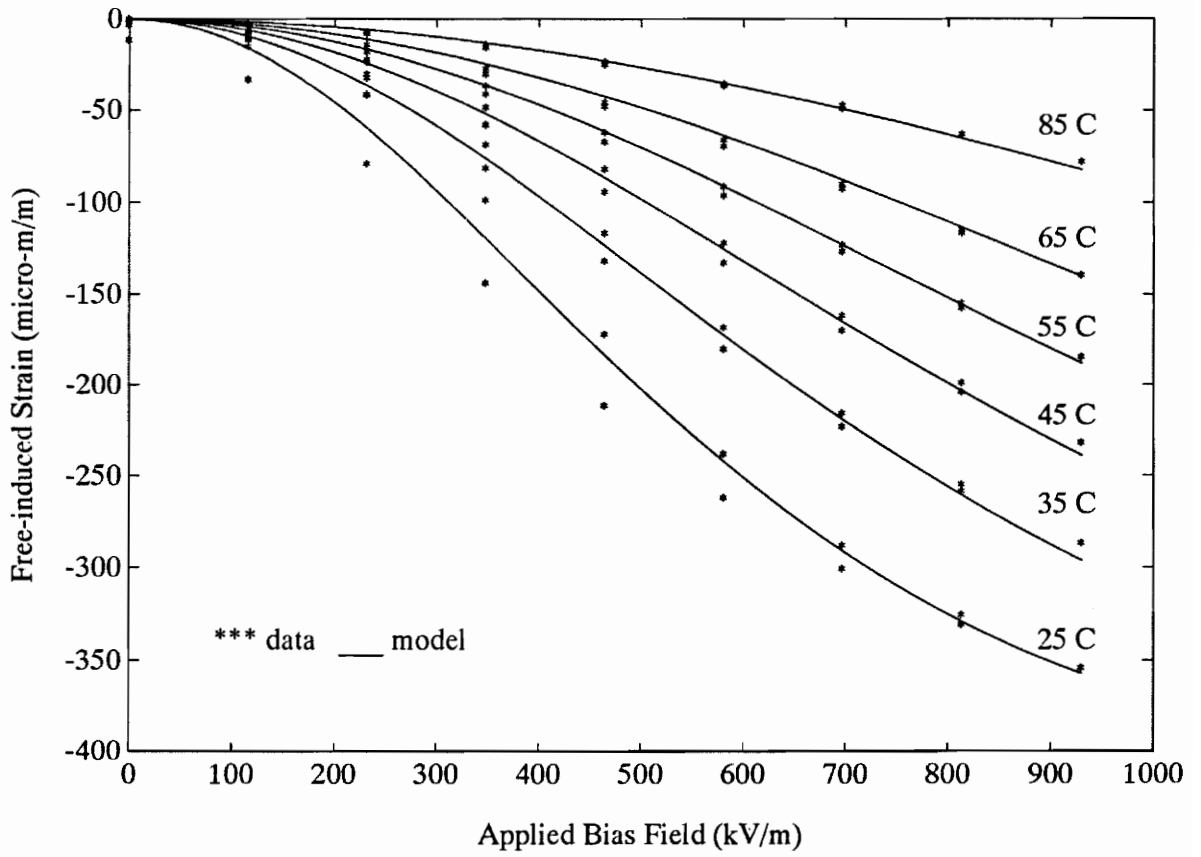


Figure 4.4 Comparison of hyperbolic tangent polarization model with DC free-induced strain experimental data.

Up to this point, models have been proposed in Chapter 4 for the AC dielectric susceptibility dependence on both temperature and frequency and for the DC dielectric susceptibility dependence on bias field and temperature. These models have been corroborated by experimental results described in Chapter 3. Regarding conservative dielectric properties, only one other relation must be addressed to complete the temperature-frequency-bias field co-dependent models for PMN-PT dielectric properties, as proposed in Chapter 1. The AC dielectric susceptibility has not been considered with respect to bias field. A logical conclusion from results with the DC susceptibility is to incorporate the hyperbolic tangent formulation into the AC susceptibility models:

$$\chi^{AC}(T, \omega, E^{DC}) = \chi^{AC}(T, \omega) \frac{\tanh[k(T)E^{DC}]}{X_E E^{DC}}. \quad (4.15)$$

Equation (4.15) will be used in modeling AC actuation with PMN-PT, discussed later in this chapter.

4.4 Electrostrictive Coefficient Relations

The transverse electrostrictive coefficient cited in models introduced by equations (4.11) and (4.14) has been assumed constant with respect to temperature and bias field. Although previous studies have indicated variation with these parameters, the degree is sufficiently minor, less than ten percent, to warrant neglect of their effects. This assumption is supported by the results of Figure 4.4. However, one other parameter considered in this study, frequency, has not yet been affiliated with the electrostrictive coefficient.

The actuator responses of Figures 3.4 and 3.5 show a rather drastic reduction of transduction sensitivity with respect to increased frequency. The large change cannot be explained by the dispersion of relative permittivity. Thus, one might surmise that the electrostrictive coefficient decreases with respect to frequency. It is here proposed that, like the variance of permittivity, Q decreases with the logarithm of frequency:

$$Q(\omega) = Q(\omega_0) + q \ln(\omega_0/\omega). \quad (4.16)$$

Equation (4.16) completes a constitutive model for the electrostrictive response of PMN-PT, so that results from actuation tests can be directly compared.

4.5 Dielectric and Actuator Transduction Responses

In equation (3.3), an expression which models the separate contributions of AC and DC components of applied electric field to the actuator transduction sensitivity was derived from an LGD phenomenological basis. Rewritten to reveal the various dependencies of parameters in this expression, while disregarding vector subscripts, this equation becomes

$$\frac{\partial \Lambda(T, \omega, E)}{\partial E^{AC}} = 2Q(\omega)\epsilon_0^2 [\chi^{DC}(T, E^{DC})\chi^{AC}(T, \omega, E^{DC})E^{DC} + [\chi^{AC}(T, \omega, E^{DC})]^2 E^{AC}]. \quad (4.17)$$

Equations (4.14) through (4.16) model how dielectric susceptibility and electrostrictive parameters vary with temperature, frequency, and bias field. Equations (4.1) through (4.13) support these models and accentuate relations buried in the three equations.

Using equation (4.17), results from the actuation experiments provided in Chapter 3 can

be directly compared with constitutive models introduced in this chapter. In Figure 4.5, the DC relative susceptibility model of equations (4.12) and (4.13) is compared with DC free-strain actuation data reduced by equation (4.14). Values for constants used to evaluate these expressions are given earlier in this chapter. Data and model results are plotted with respect to temperature at a given bias field. Frequency does not pertain to DC relative permittivity.

As compared with AC results of Figure 3.1, most notable in Figure 4.5 are the extremely large values of relative permittivity, derived from both DC free-induced strain data and from the constitutive model. Another difference is that the thermal response of DC susceptibility does not have the characteristic Gaussian shape in the range of temperatures that the AC susceptibility of Figure 3.1 does. In Figure 3.1, the experimental data do indicate, as does the model of equation (4.5), that for lower frequencies, the Curie maximum shifts to lower temperatures. An extrapolation of plots in Figure 3.1 to DC, however, would not reveal the shape and low T_{max} of Figure 4.5. Nevertheless, reduced data based on the electrostrictive phenomenology-derived expression of equation (4.14) corroborate the high permittivity values and thermal response shape for DC electric field stimuli. The discernment of relative susceptibility in experimental results of Figure 3.1 arises from AC field inputs. According to the differences between Figures 4.5 and 3.1, frequency dispersion of dielectric properties excited by any AC source drastically reduces the realized permittivity of DC-induced polarization.

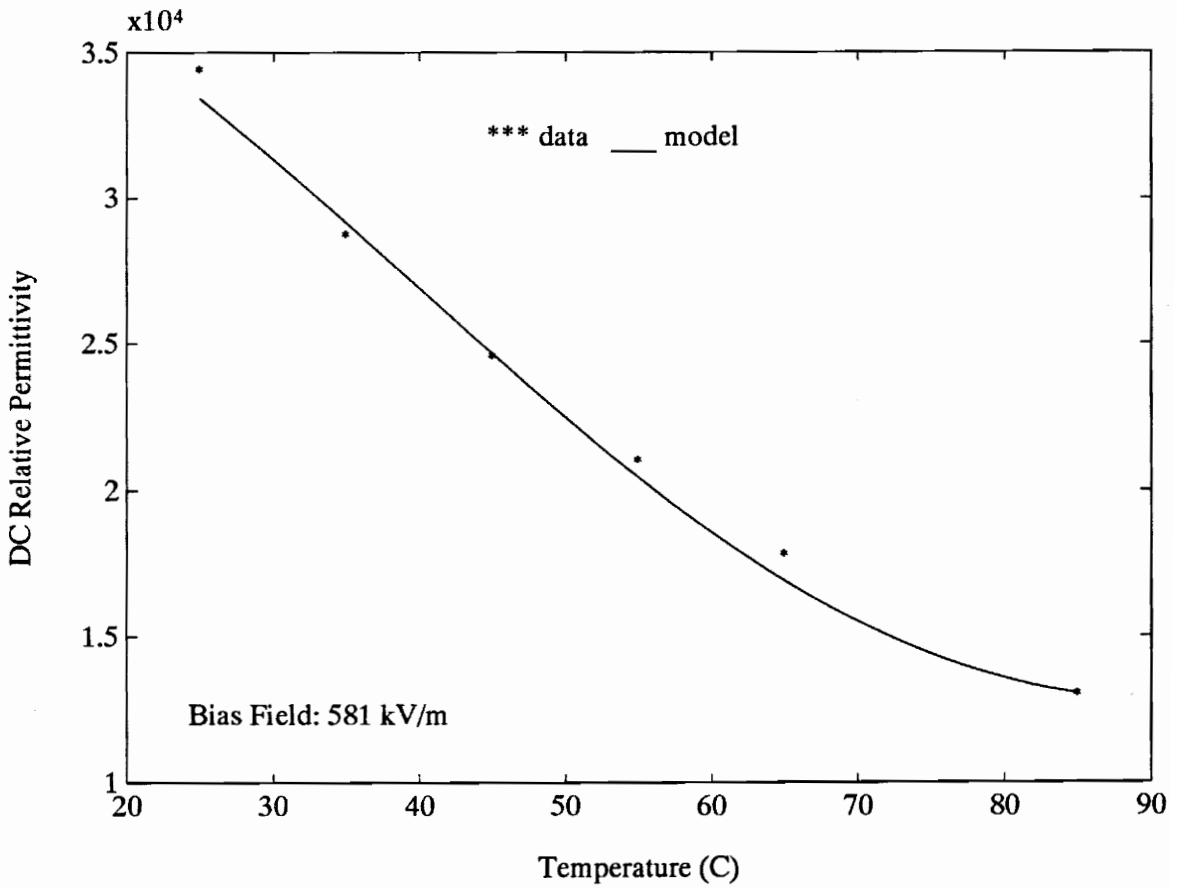


Figure 4.5 Comparison of DC relative susceptibility model results with reduced data from DC free-induced strain response experiments versus temperature.

In Figure 4.6, the AC relative susceptibility for constitutive models embodied primarily by equations (4.8), (4.9), and (4.15) are compared with experimental results of Chapter 3. It should be noted here that data in Figure 4.6 have been reduced by equation (4.15), since bias field effects could not be implemented in dielectric experiments. All constants for the constitutive models illustrated in plots of Figure 4.6 are identical to those introduced earlier. Again, there is very strong correspondence between experimental and model results for the thermal AC permittivity responses, both in shape and amplitude.

A final test of empirical, phenomenological modeling introduced in this chapter with respect to temperature variation is to compare model results with PMN-PT AC actuator experimental data. This comparison requires the use of equations (4.16) and (4.17), in addition to the permittivity model equations. In Figure 4.7, actuator transduction sensitivity experimental data is plotted with respect to temperature at various frequencies and is compared with constitutive model results, which incorporate results of Figures 4.5 and 4.6. All constants used to formulate values for actuator transduction have been introduced, except for those of equation (4.16), which are $Q(100 \text{ Hz}) = -0.014 \text{ m}^4/\text{C}^2$ and $q = 4.0057 \times 10^{-3} \text{ m}^4/\text{C}^2$. The shapes and amplitudes of formulated plots in Figure 4.7 fit data remarkably well. Based on these results, the constitutive models of this chapter appear to successfully relate the behavior of PMN-PT relaxor ferroelectrics as electrostrictive actuators.

As described in Chapter 3, since the co-dependent effects of three extrinsic

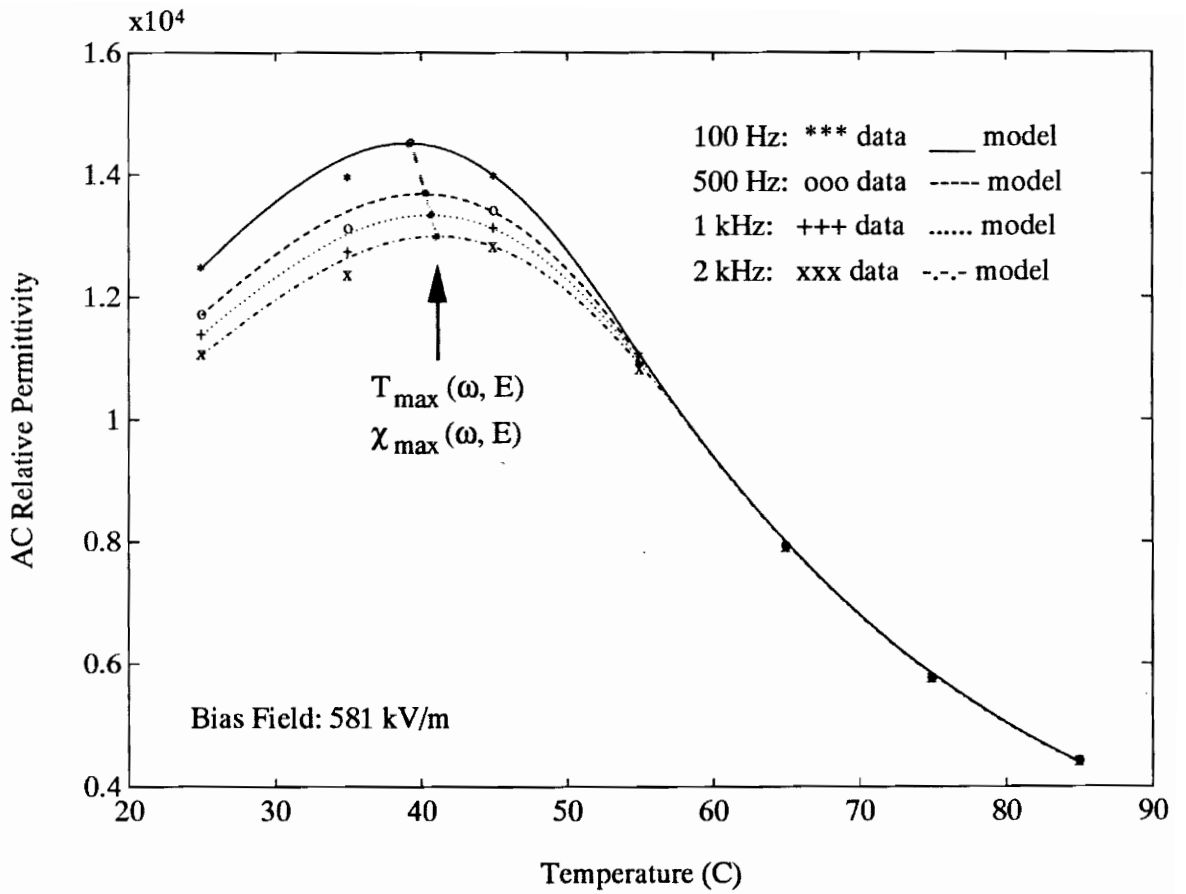


Figure 4.6 Comparison of AC relative susceptibility model results with reduced data from permittivity response experiments versus temperature at various frequencies.

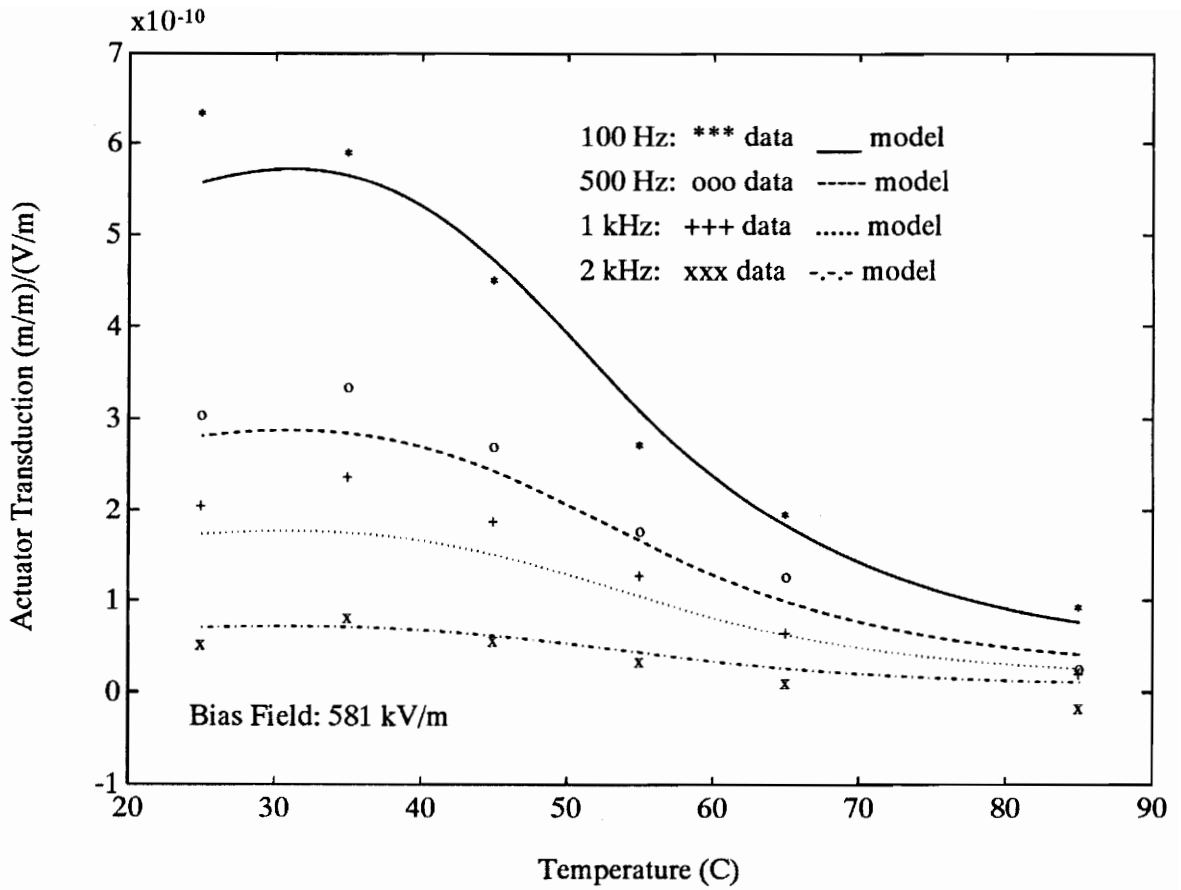


Figure 4.7 Comparison of electrostrictive constitutive model results with data from AC actuator response experiments versus temperature at various frequencies.

parameters—temperature, frequency, and bias field—on dielectric and electrostrictive performance of PMN-PT are studied, there are six permutations to describe the material behaviors. However, only three of these are necessary to fully comprehend the responses since the other three are simply converse relations. One of these three, the thermal response at different frequencies and constant bias field, is illustrated for DC susceptibility, AC susceptibility, and actuator transduction in Figures 4.5 through 4.7, respectively. The other two responses must be examined to completely compare constitutive modeling of Chapter 4 with experimental actuation results of Chapter 3.

One of these two, frequency response at different bias fields and constant temperature, precludes the DC permittivity, since it cannot vary with frequency. Nonetheless, the AC relative susceptibility certainly varies with respect to frequency, and plots comparing experimental and model results are provided in Figure 4.8. The model, which is based on linear variation of permittivity parameters with respect to the logarithm of frequency, compares exceedingly well to data from dielectric experiments. Again, all constants used to evaluate model equations have been provided earlier in this chapter.

Amplitudes of frequency response plots in Figure 4.9 for model results do not compare so favorably with actuator transduction experimental data. However, shapes of model curves do correspond with the data trends in this figure, and relative amplitudes for different bias fields match reasonably well. If the maximum standard deviation of 8×10^{-11} (m/m)/(V/m) for actuator transduction sensitivity data, as presented in Chapter 3, is

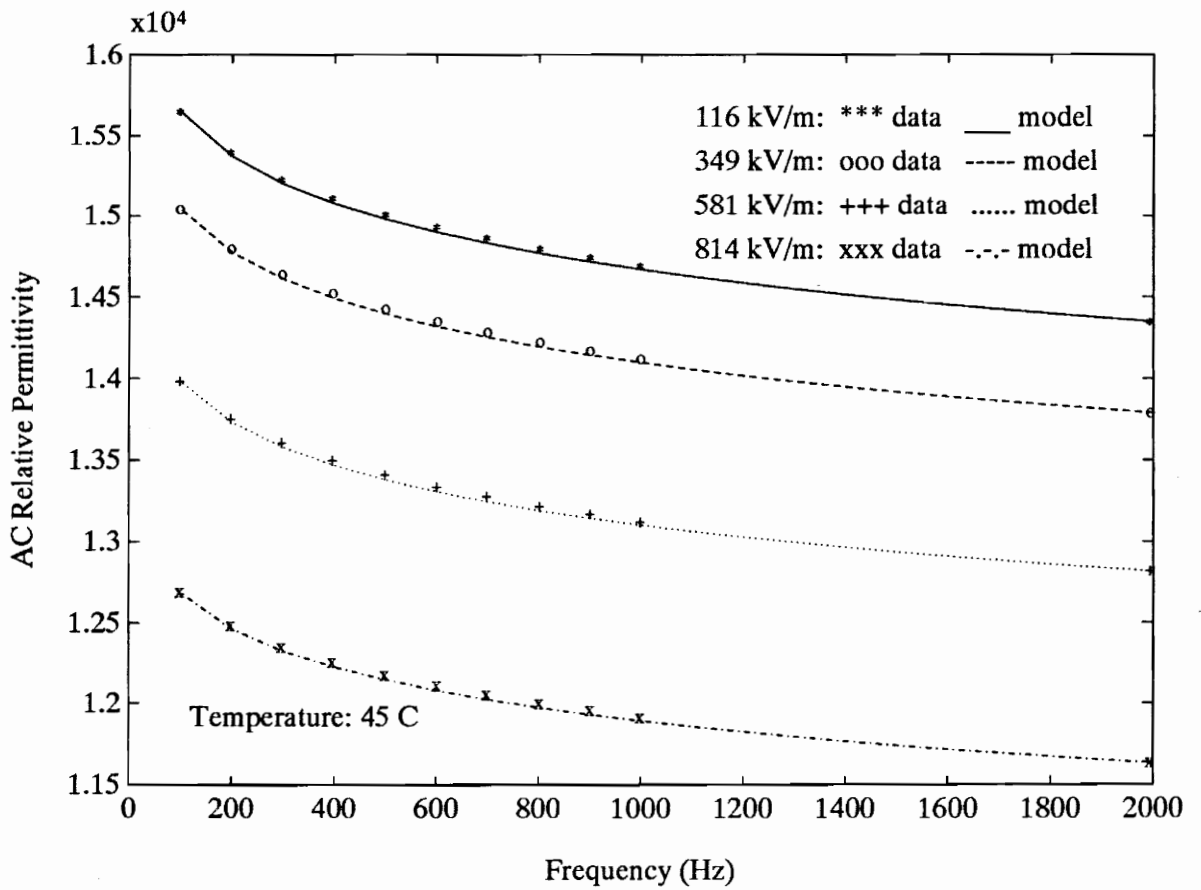


Figure 4.8 Comparison of AC relative susceptibility model results with reduced data from permittivity response experiments versus frequency at various bias fields.

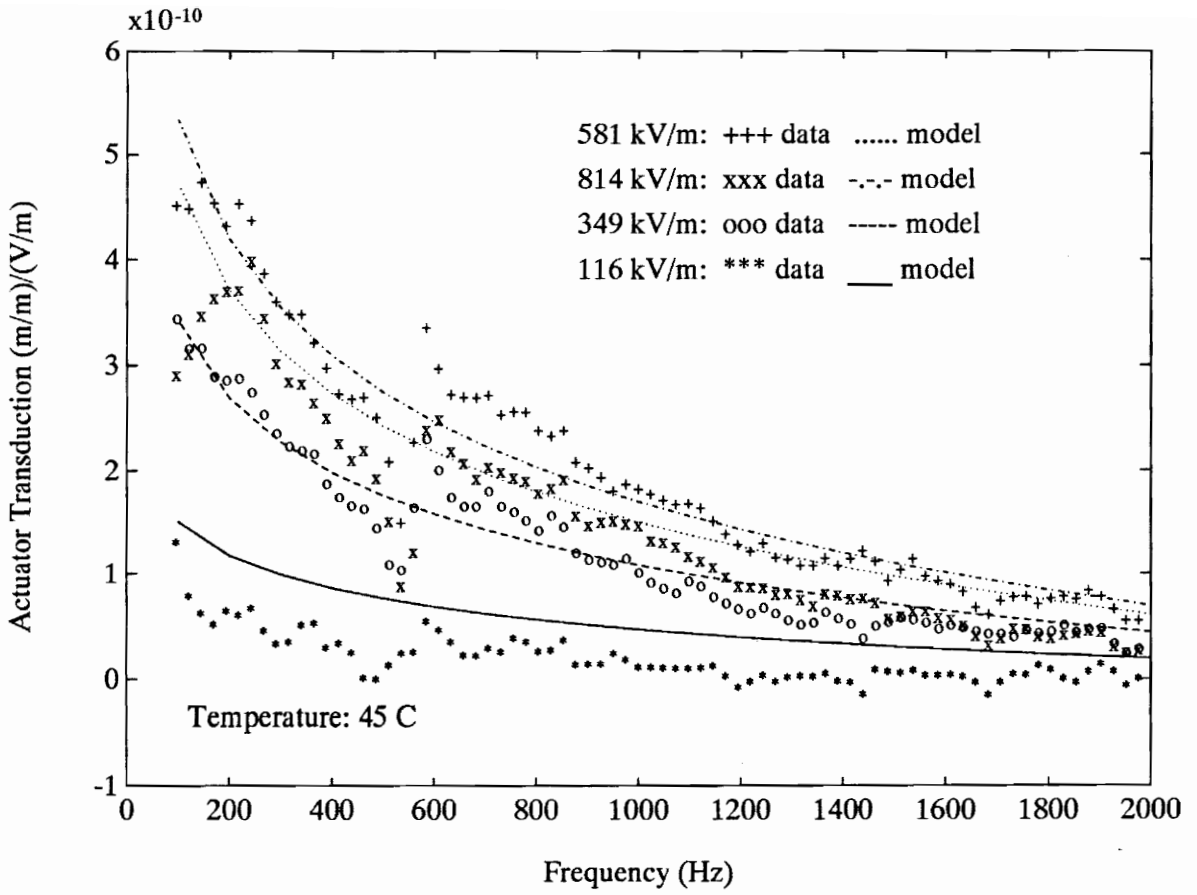


Figure 4.9 Comparison of electrostrictive constitutive model results with data from AC actuator response experiments versus frequency at various bias fields.

considered, plots representing the model are well within empirical variation. Regardless, shapes and relative amplitudes, both of which are satisfactory in Figure 4.9, are the two most important aspects of model responses with regard to mechanical and control design.

A final comparison of experimental results with formulations introduced in this chapter involves variation of PMN-PT material properties with respect to applied bias field. In Figure 4.10, relations for the DC relative permittivity are plotted against bias field at different temperatures. The differences between experimental data and model results for relatively low bias fields illustrates a failing of the hyperbolic tangent polarization model. According to DC free-induced strain data reduced by equation (4.14), the relative susceptibility is much larger for low bias fields than predicted by the hyperbolic tangent model of equation (4.13). The shape of responses with respect to smaller bias fields is ill-represented by the model. One other problem with this model is that values for zero applied DC field do not exist. Nevertheless, for larger values of bias field the model is sufficiently accurate, according to Figure 4.10.

In Figure 4.11, experimental and model results for AC relative susceptibility are displayed with respect to bias field at different temperatures and constant frequency. This figure and Figure 4.10 both illustrate the reduced effects of bias field with increased temperatures, or the onset of the paraelectric phase of PMN-PT. Slopes of isothermal plots decrease drastically with higher temperatures; in fact, at 85°C the susceptibility is almost constant versus bias field. Again, it should be noted that data from dielectric

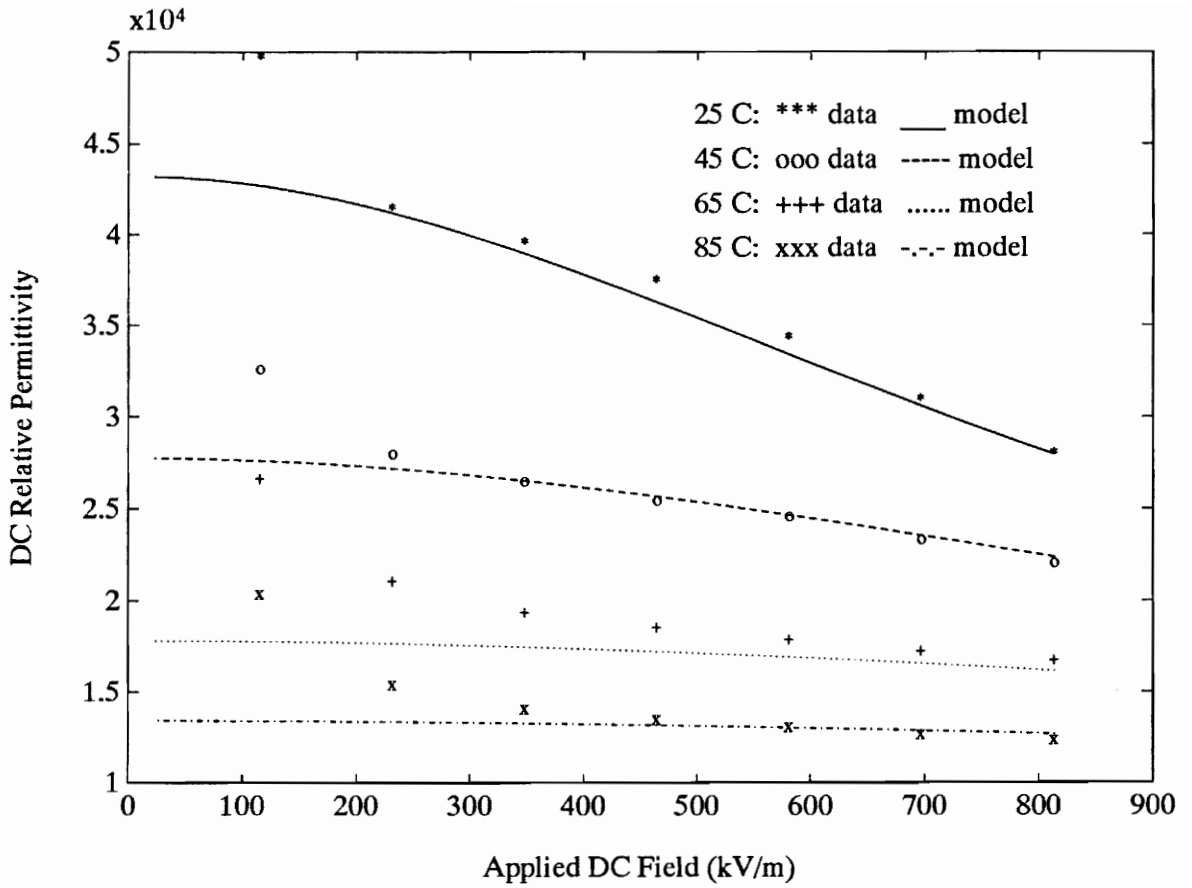


Figure 4.10 Comparison of DC relative susceptibility model results with reduced data from DC free-induced strain response experiments versus bias field.

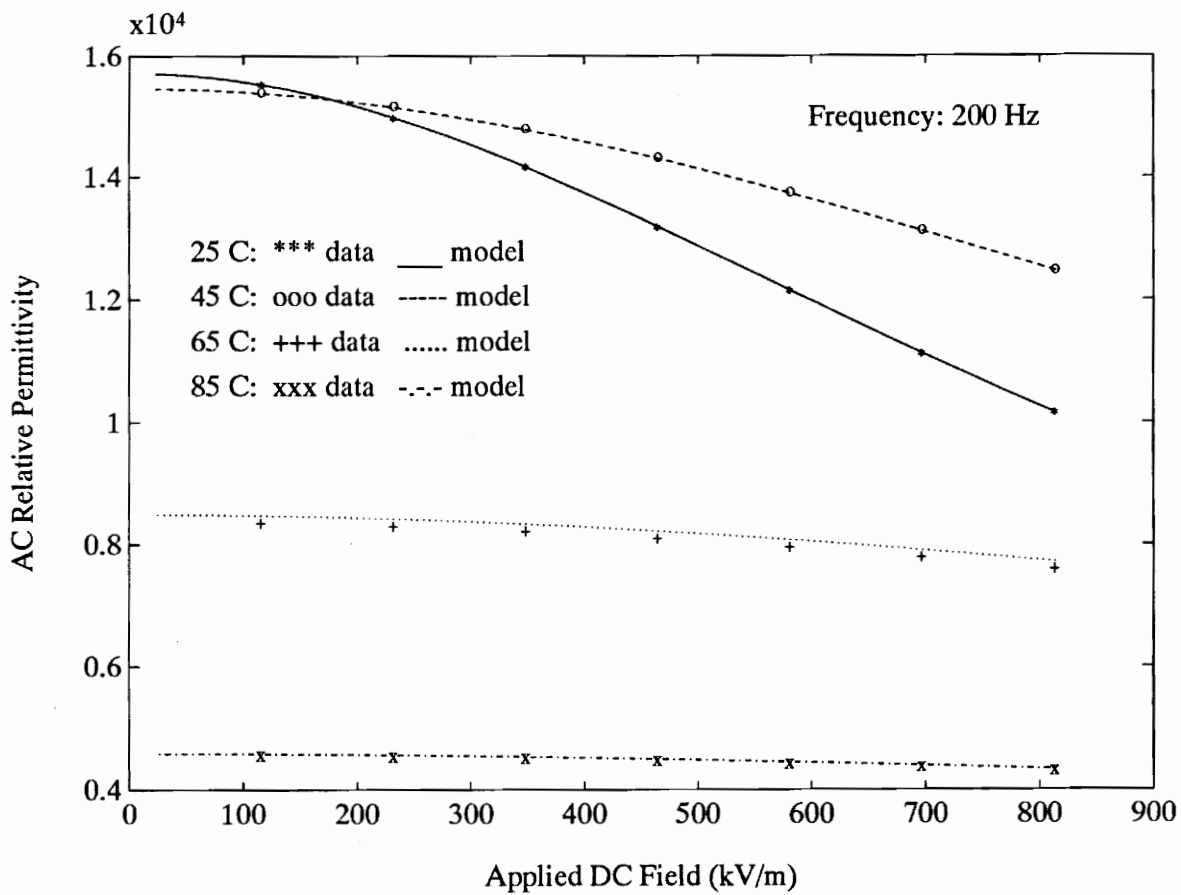


Figure 4.11 Comparison of AC relative susceptibility model results with reduced data from permittivity response experiments versus bias field at various temperatures.

experiments have been adjusted by bias field, as in equation (4.15), since such data were not experimentally obtained. This step was necessary to contrast model results and data.

The plots of Figure 4.12 complete the comparison of actuator transduction data with values from constitutive models. Plots in this figure truly exemplify the accuracy and utility of the dielectric and electrostrictive models introduced earlier in this chapter. Although formulated amplitudes do not match exactly with experimental data, trends illustrated by model plots with respect to bias field are notably consistent with data.

Figures 4.5 through 4.12 illustrate the utility of the temperature-frequency-bias field co-dependent models for DC susceptibility, AC susceptibility, and AC actuator transduction sensitivity embodied in equations (4.1) through (4.17). Although amplitudes for these material behaviors do not correspond precisely with experimental values, these models illustrate trends exceedingly well, within the ranges of data. Amplitude differences can be the result of many factors, such as improper selection of model constants, variation of experimental conditions and procedure, and material property variation due to processing. However, the correspondences of response shapes and relative amplitudes are important with regard to mechanical design of PMN-PT actuators for intelligent material systems. Design and performance optimization really precludes absolute values in favor of relative improvements. Constants are of little consequence; although, the ratio of constants can be extremely important. These ratios are reasonably portrayed by the models and constants presented in this chapter for PMN-PT electrostrictive behavior.

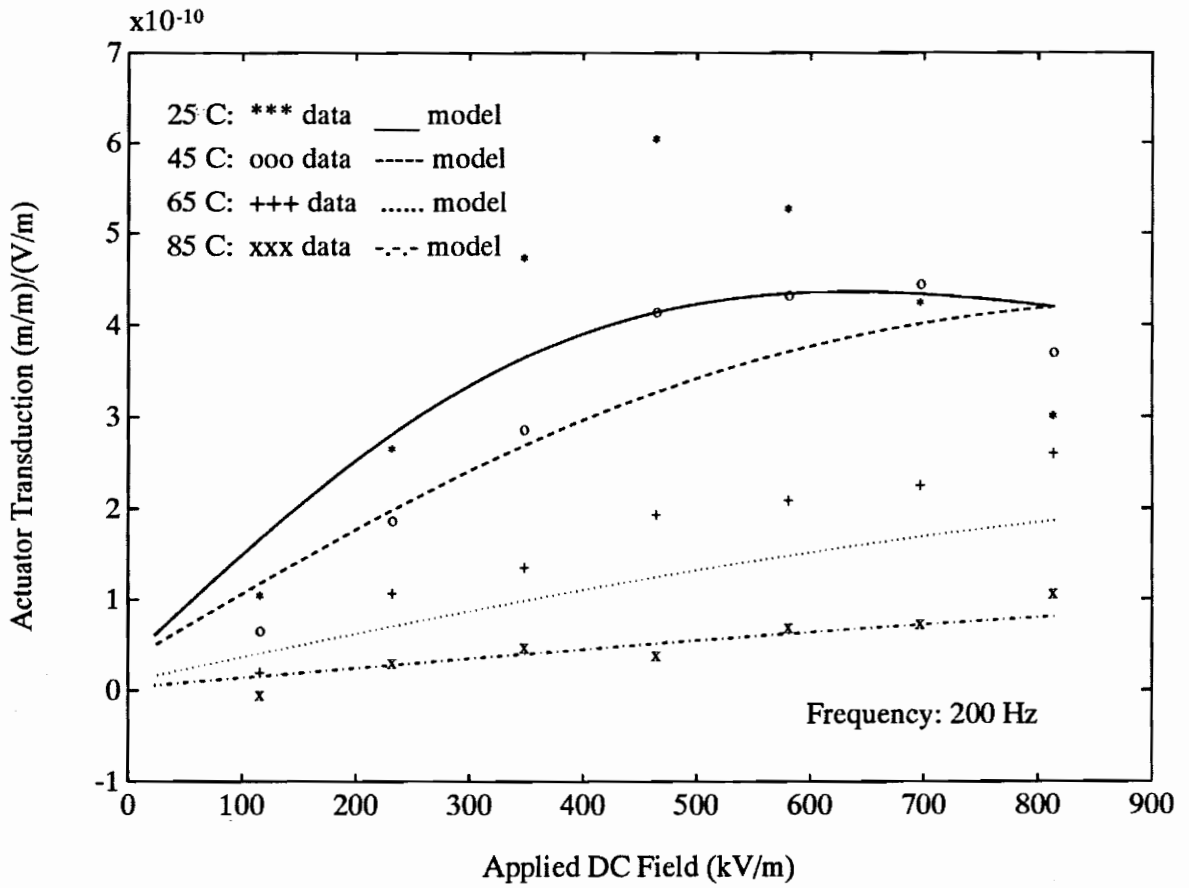


Figure 4.12 Comparison of electrostrictive constitutive model results with data from AC actuator response experiments versus bias field at various temperatures.

4.6 Sensor Transduction Response

In the discussion of Chapter 3, there was attention given to fundamental differences between employing PMN-PT as an actuator and using it as a sensor. It was noted that for sensing application, the extent of polarization is minute. Since stress-induced polarization amplitudes are very small, the unlikelihood that frequency affects polarization reversal was recognized theoretically and observed experimentally in Figures 3.10 and 3.11. This insignificance must be reflected in the modeling of PMN-PT behavior, as well.

All of the tools for modeling sensing behavior, even most of the material constants, have been introduced. Essentially, the polarization model of equation (1.22), including the temperature relations of equation (4.12), are incorporated into the electrostrictive phenomenology for sensing in equation (3.4). As such, by taking the derivative of equation (3.4) with respect to applied strain, an expression for the sensor transduction sensitivity, disregarding tensor subscripts, is derived:

$$\frac{\partial E(T, E^{DC})}{\partial s} = QP^s Y \tanh[k(T)E^{DC}] + g^o(T)Y, \quad (4.18)$$

where $k(T)$ is described by equation (4.12).

Most of the constants of equation (4.18)— Q , P^s , Y , k_i , and g^o —have been appraised for PMN-PT used in the present investigations, except for Young's modulus and the electrostrictive piezoelectric voltage coefficient. Technical specifications from AVX

Corporation (Galvagni and Duprè, 1990) show values for the compressive Young's modulus as high as 112 GPa for stack geometries of their PMN-PT solid solution. However, present studies empirically indicate that for the monomorph configuration, the tensile modulus of elasticity is far less, at $Y = 20$ GPa. For ceramic materials, this large difference between tensile and compressive moduli is not unusual.

The empirically derived value for the transverse electrostrictive piezoelectric term of equation (4.18) is around $g^o(25^\circ\text{C}) = 2 \times 10^{-5}$ V-m/N. Actually, this value is related to the spontaneous polarization of PMN-PT, illustrated in Figure 1.14 (p. 35), and thus depends on temperature. Viehland et al. (1990) have suggested a model for spontaneous polarization that relates to the freezing temperature, highlighted in Figure 1.14 and analogous to polar spin-glass magnetic behavior. However, electrostrictive piezoelectric-spontaneous polarization relations are beyond the scope of this thesis, so that the empirical value provided above suffices for modeling efforts.

Based on these constants, the model of equation (4.18) compares fairly well in Figure 4.13 with data from experimental sensing results of Chapter 3. Scatter in data results from 60-Hz noise and FFT aliases of that noise. Since frequency was not modeled as influential on dielectric properties, it was also considered to have a negligible effect on electrostrictive properties, so that a constant value of $Q = -0.008$ m⁴/C² was chosen. In these plots, the independence of frequency is illustrated by both experimental and model results. Furthermore, relative amplitudes of the hyperbolic tangent model of

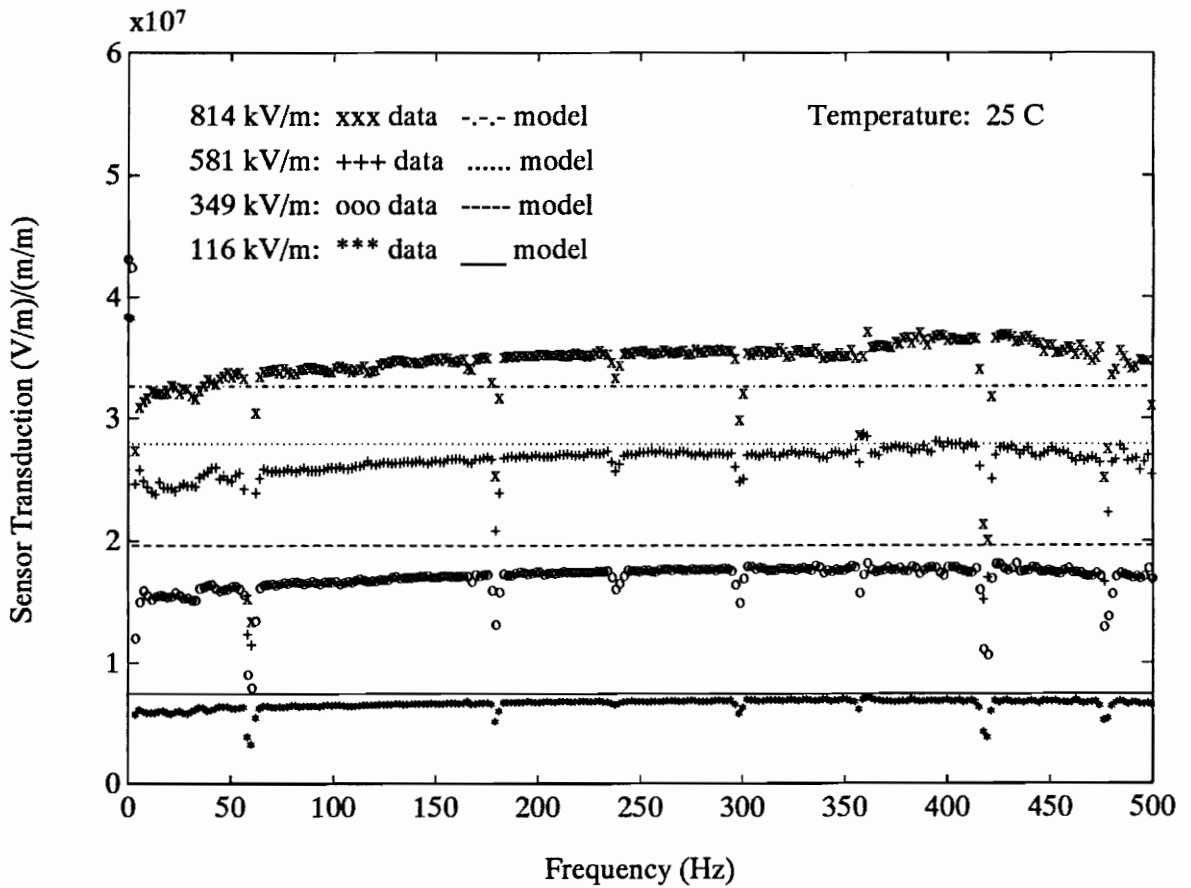


Figure 4.13 Comparison of electrostrictive constitutive model results with data from AC sensor response experiments versus frequency at various bias fields.

equation (4.18) compare favorably with data. Thermal responses for PMN-PT sensing were not investigated, but the temperature-dependent coefficient k of equation (4.12) can be confidently used to model sensor transduction, based on results previously obtained. However, the temperature-dependent constant g^o must be considered in such modeling.

4.7 Summary: A Constitutive Model for PMN-PT

Since the order of model equations in this chapter does not necessarily best fit the order with which a designer might employ them, the following summary is offered as somewhat of a procedure for using the proposed models for PMN-PT transduction.

4.7.1 Sensing with PMN-PT

The model proposed for sensing is completely independent of the separate descriptions for DC and AC relative susceptibility. Furthermore, there is no frequency dependence for either dielectric or electrostrictive terms in this model. As such, if PMN-PT is used as a sensor only, there is no reason to bother with models for such terms. Equation (4.18) models the transduction sensitivity of PMN-PT sensors, which is the voltage generated per unit of applied alternating strain. This transduction sensitivity varies with applied bias field and with temperature. In this equation, the electrostrictive, saturation polarization, and elastic modulus coefficients are assumed constant. The hyperbolic tangent polarization model coefficient k varies with temperature by the relation of equation (4.12). The electrostrictive piezoelectric term varies with spontaneous polarization, or temperature, and has not been modeled, since no experiments were

designed to investigate its behavior.

4.7.2 Servo Actuation with PMN-PT

The other electrostrictive effect involving use of PMN-PT with intelligent material systems and structures is actuation. Three types of actuation have been classified in Chapter 1—servo, on/off, and AC. As with sensing, servo actuation with PMN-PT does not necessitate modeling frequency dependence of dielectric and electrostrictive terms. Instead, a relation identical to equation (4.11), without tensor subscripts and including temperature variation, is all that is required:

$$\Lambda(T, E^{DC}) = Q[P^s \tanh[k(T)E^{DC}]]^2, \quad (4.19)$$

where Q and P^s are constants, and $k(T)$ is given by equation (4.12).

4.7.3 DC Dielectric Susceptibility

Since DC dielectric susceptibility pertains to bias fields with both on/off and AC actuation with PMN-PT, its appraisal is a reasonable first step in realizing a model for frequency-dependent actuator behavior. Equation (4.13) represents the temperature and bias field dependence of the DC dielectric susceptibility. Again, the temperature variation of k is described by equation (4.12).

4.7.4 AC Dielectric Susceptibility

If the design involves implementation of PMN-PT as a servo actuator, this section is of

little consequence, and the designer can skip to the next section on actuator transduction, unless there are dynamic concerns. If an on/off or AC actuator is considered, the procedure in this section should be consulted to model the temperature-frequency-bias field co-dependent AC dielectric susceptibility. The proposed model begins with equation (4.15), which really just describes the bias field variation. The k polarization parameter comes from equation (4.12), and X_E is a constant.

To evaluate the variable $\chi^{AC}(T,\omega)$ of equation (4.15), equations (4.8) and (4.9) need to be consulted. Variables arising in these equations which must be accounted include χ_m , χ_{max} , T_{max} , and λ ; χ^{AC} is a constant. Equations (4.8) and (4.9) are designed so that grain size and a permittivity at known temperature and frequency are the only material measurements required, in addition to realizing values for constants. For the frequency-dependent χ_m , equations (4.10) and (4.7) are utilized. $\chi(T_o,\omega_o)$ describes the value of susceptibility measured at a known temperature and frequency, and X is a constant.

The frequency dispersive relations for T_{max} and χ_{max} are provided by equations (4.5) and (4.6) respectively. τ_{max} and X_{max} are constants in these relations. $T_{max}(\omega_o)$, $\chi_{max}(\omega_o)$, and λ are related to grain size by equations (4.1), (4.2), and (4.3), respectively. λ of equation (4.3) is indirectly related to grain size by $\chi_{max}(\omega_o)$ of equation (4.2). Evaluation of these equations with their appropriate constants completes models for the AC permittivity, so that dynamic actuation with PMN-PT can be perceived.

4.7.5 Dynamic Actuation with PMN-PT

The transduction sensitivity for cyclic driving of a PMN-PT actuator with a moderate alternating electric field is modeled in equation (4.17). Dielectric parameters in this model are found from relations described above. Additionally, for moderate to large AC driving fields, the frequency-dispersive electrostrictive coefficient is modeled by equation (4.16). As with dielectric terms, this relation involves a linear decay of the coefficient with respect to the logarithm of frequency.

Chapter 5

Conclusions and Recommendations

In this thesis, electromechanical behavior of the relaxor ferroelectric PMN-PT was experimentally characterized and phenomenologically modeled. Dielectric, sensing, and actuation behaviors of PMN-PT monomorphs were investigated. Dielectric properties were compared with previous findings and were correlated with grain size studies. Based on Landau-Ginzburg-Devonshire (LGD) phenomenology for electrostrictive effects, the relative susceptibility is of utmost importance, since electrostriction is related to polarization. As such, aspects of polarization, including dielectric susceptibility, were carefully considered and modeled for electrostrictive sensing and actuation constitutive relations with PMN-PT. These models, based on empirical equations, agree very well with data acquired from experiments with the PMN-PT monomorphs. Highlights of results discussed in the previous chapters are presented below:

- Phenomenology based on LGD thermodynamic formalism, which relates transduction sensitivity with applied DC bias field, was developed for electrostrictive sensing. A hyperbolic tangent model was introduced to relate bias field with polarization and to include temperature variation of sensor transduction sensitivity. Comparison of experimental data with PMN-PT monomorphs showed that results with this model conform very well.

- LGD phenomenology for DC, or servo, actuation with electrostrictors was again related to the hyperbolic tangent polarization model. Temperature and bias field dependencies of PMN-PT servo actuation were experimentally demonstrated and were well represented by constitutive models.
- Relations for DC dielectric susceptibility of PMN-PT were derived from the hyperbolic tangent polarization model and included temperature dependencies. The model agreed very well with experimental data, except at low bias fields values. It underpredicted DC susceptibility for bias fields less than 250 kV/m.
- Temperature-frequency-bias field co-dependence on the AC dielectric susceptibility was documented experimentally and modeled phenomenologically. The model embodies hyperbolic tangent polarization relations for bias field described above, Gaussian relations for the primarily ferroelectric phases of the thermal transition, linear relations with respect to temperature for the paraelectric phases after the Curie maximum temperature, and logarithmic frequency relations to account for dispersion of dielectric properties. The co-dependent model fit data extremely well.
- Logarithmic frequency dispersive relations similar to those modeled for AC susceptibility were incorporated in models for the electrostrictive coefficient associated with moderate cyclic-field driving of PMN-PT actuators.

- Models for the frequency-dependent electrostrictive coefficient, temperature- and field-dependent DC susceptibility, and temperature-frequency-field co-dependent AC susceptibility were tested by coupling them with LGD actuator phenomenology and comparing the model results with experimental data. The constitutive model for cyclic actuation of PMN-PT compared favorably with experimental results. Response shapes and relative amplitudes were very accurate.
- Finally, since an objective for the research was to develop models for PMN-PT which can be readily utilized by intelligent material system designers, a procedural summary for using the constitutive relations was included in the text.

Although results from this research include models which account for the behaviors of PMN-PT very well, these models describe only transverse transduction, i.e., only actuation and sensing perpendicular to applied or measured electrical quantities. Furthermore, there are other aspects of the findings and models in this thesis which require further investigations. Approaches discussed herein for modeling PMN-PT behavior could be generalized and improved by the following suggestions:

- Processing effects on grain size should be studied for 0.9PMN-0.1PT specifically, to realize constants for the algebraic relations between grain size and dielectric properties.

- Frequency dependence of the electrostrictive coefficient should be further characterized and validated, since there are no other research endeavors in the literature to confirm this behavior.
- The electrostrictive piezoelectric coefficients developed from LGD phenomenology require better understanding. For example, the relation of the electrostrictive piezoelectric voltage coefficient to spontaneous polarization could be researched.
- The tensor behavior should be robustly investigated and modeled, like the transverse transduction studies of this thesis, for design of PMN-PT sensors and actuators in configurations utilizing other tensor properties, for example, a stack geometry.
- Finally, constitutive equations introduced in this thesis and perhaps augmented by future studies should be applied both computationally and experimentally to control and mechanical design of smart material systems, in order to better evaluate their utility.

Glossary

Bimorph: composite of at least two monomorphs which can be used to induce either free-induced extensional strain (like monomorphs) or free-induced bending, depending on the shape of electrodes and direction of applied fields.

Centrosymmetric: non-polar class of single crystals possessing a center of ionic symmetry.

Curie Maximum Temperature: for relaxor ferroelectrics, the temperature corresponding to the maximum value of dielectric permittivity during the diffuse ferroelectric-paraelectric phase transformation.

Curie Temperature: the temperature corresponding to the transformation from a ferroelectric to a paraelectric material phase and coinciding with the maximum value of dielectric permittivity of an electroceramic.

Dielectric: a material which, when subjected to an applied electric field, exhibits a limited rearrangement of charges (unlike the long transport of conductors) and is thus polarized.

Electrostriction: capacity of a material to develop changes in dimensions proportional to the square of the polarization induced by an electric field; converse electrostrictive effects include linear stress dependence of reciprocal susceptibility and linear polarization dependence of the piezoelectric voltage coefficient.

Ferroelectric: subgroup of pyroelectric crystalline materials whose spontaneous polarization can be reversed by an electric field; lower temperature material phase associated with reversible pyroelectric behavior.

Monomorph: relatively thin dielectric plate having opposite (parallel-plate) electrodes for application of electric field and possessing significant mechanical stiffness.

Noncentrosymmetric: class of polar single crystal material not exhibiting a center of ionic symmetry.

Paraelectric: higher-temperature phase of ferroelectric materials for which there is no spontaneous polarization.

Permittivity: a measure of the capacity for polarization of a dielectric medium which includes effects of electrodes; the **relative permittivity** (same as the **dielectric constant**) of a dielectric material is the ratio of permittivity of that material to the permittivity of free space (vacuum).

Permittivity/Susceptibility Ratio (Dielectric Loss or Dissipation Factor): a ratio of the capacity for long range transport of charges in a dielectric medium (**capacitive resistance**) to the permittivity of the medium; the ratio energy loss to energy stored in a dielectric material.

Perovskite: crystalline structure having composition $A^{(+)}B^{(+)}O_3^{(2-)}$ and structure depicted in Figure 1.9 on p. 25.

Piezoelectric: class of noncentrosymmetric single crystals which can be polarized by the application of stress (**piezoelectric voltage coefficient**) and conversely be deformed by the application of an electric field (**piezoelectric strain coefficient**).

Polarization: the limited rearrangement of charges into dipole moments, or sets of equally opposite charges which store energy, in a material subjected to an electric field; dipole moments store energy since they represent a balanced displacement of charges.

Pyroelectric: class of piezoelectric single crystals which develop a spontaneous polarization that varies with temperature.

Relaxor Ferroelectric: a ferroelectric whose phase transition to a paraelectric state occurs over a relatively broad range of temperatures and whose dielectric properties vary with frequency before and during this phase transition.

Relaxor Phase Transition (or **Diffuse Phase Transition):** thermally-induced material transition from ferroelectric to paraelectric ceramic phases occurring over a relatively wide range of temperatures and exhibiting frequency dispersion of dielectric properties.

Spontaneous Polarization: under certain thermal conditions, the crystalline lattice polarization can produce local fields which control individual atoms and/or ions and which tend to stabilize the polarization, in a feedback-like mechanism, so that the aggregate structure is polarized without the application of an electric field.

Susceptibility: a measure of the capacity for polarization of a dielectric medium, as compared with that of free space; for materials with a relative permittivity greater than 1000, the relative permittivity and susceptibility are virtually identical.

References

- von Cieminski, J. and H. Beige, 1991. "High-signal electrostriction in ferroelectric materials," *Journal of Physics D* **24**[7], 1182-1186.
- Cross, L.E., 1987. "Relaxor Ferroelectrics," *Ferroelectrics* **76**, 241-267.
- Cross, L.E., S.J. Jang, R.E. Newnham, S. Nomura and K. Uchino, 1980. "Large electrostrictive effects in relaxor ferroelectrics," *Ferroelectrics* **23**, 187-192.
- Damjanovic, D. and R.E. Newnham, 1992. "Electrostrictive and piezoelectric materials for actuator applications," *Journal of Intelligent Material Systems and Structures* **3**, 191-209.
- Ealey, M.A. and P.A. Davis, 1990. "Standard SELECT electrostrictive lead magnesium niobate actuators for active and adaptive optical components," *Optical Engineering* **29**[11], 1373-1382.
- Galvagni, J. and D. Duprè, 1990. "Electrostrictive actuators, precision electromechanical components," Technical Information, AVX Corporation, Myrtle Beach, SC.

Grindlay, J., 1970. An Introduction to the Phenomenological Theory of Ferroelectricity, Pergamon Press, New York, New York.

Haertling, G.H., 1986. "Piezoelectric and electrooptic ceramics," Ceramic Materials for Electronics, 140-222.

Hilton, A.D., D.J. Barber, C.A. Randall and T.R. ShROUT, 1990. "On short range ordering in the perovskite lead magnesium niobate," *Journal of Material Science* **25**, 3461-3466.

Moulson, A.J. and J.M. Herbert, 1990. Electroceramics: Materials, Properties, Applications, Chapman & Hall, New York, New York.

Namboodri, C.G. and C.A. Rogers, 1992. "Tunable Vibration/Strain Sensing with Electrostrictive Materials," *Proceedings of the Conference on Recent Advances in Adaptive and Sensory Materials and their Applications*, Blacksburg, VA, 285-297.

Newnham, R.E., 1991. "Tunable transducers: nonlinear phenomena in electroceramics," *NIST Special Publication 804, Chemistry of Electronic Ceramic Materials*, Proceedings of the International Conference, Jackson, WY.

- Newnham, R.E. and G.R. Ruschau, 1991. "Smart electroceramics," *Journal of the American Ceramic Society* **74**[3], 463-480.
- Nomura, S. and K. Uchino, 1982. "Electrostrictive effect in $\text{Pb}(\text{Mg}_{1/3}\text{Nb}_{2/3})\text{O}_3$ -type materials," *Ferroelectrics* **41**, 117-132.
- Pan, W., E. Furman, G.O. Dayton and L.E. Cross, 1986. "Dielectric aging effects in doped lead magnesium niobate: lead titanate relaxor ferroelectric ceramics," *Journal of Materials Science Letters* **5**, 647-649.
- Pan, W.Y, W.Y. Gu, D.J. Taylor and L.E. Cross, 1989. "Large piezoelectric effect induced by direct current bias in PMN:PT relaxor ferroelectric ceramics," *Japanese Journal of Applied Physics* **28**[4], 653-661.
- Papet, P., J.P. Dougherty and T.A. Shrout, 1990. "Particle and grain size effects on the dielectric behavior of the relaxor ferroelectric $\text{Pb}(\text{Mg}_{1/3}\text{Nb}_{2/3})\text{O}_3$," *Journal of Materials Research* **5**[12], 2902-2909.
- Rogers, C.A. and S.C. Stein, 1992. "Recent advances in structural control using intelligent materials systems," Center for Intelligent Material Systems and Structures, Blacksburg, VA.

- Rolov, B.N., 1965. "Effect of composition fluctuations on unsharp ferroelectric phase transitions," *Soviet Physics Solid State* **6**[7], 1676-1678.
- Setter, N. and L.E. Cross, 1980. "The role of B-site cation disorder in diffuse phase transition behavior of perovskite ferroelectrics," *Journal of Applied Physics* **51**[8], 4356-4360.
- Shrout, T.S., U. Kumar, M. Megherhi, N. Yang and S.J. Jang, 1987. "Grain size dependence of dielectric and electrostriction of $\text{Pb}(\text{Mg}_{1/3}\text{Nb}_{2/3})\text{O}_3$ -based ceramics," *Ferroelectrics* **76**, 479-487.
- Smolenskii, G.A. and A.I. Agranovskaya, 1959. "Dielectric polarization of a number of complex compounds," *Soviet Physics Solid State* **1**, 1429-1437.
- Smolenskii, G.A., V.A. Isupov, A.I. Agranovskaya and S.N. Popov, 1961. "Ferroelectrics with diffuse phase transitions," *Soviet Physics Solid State* **2**[11], 2584-2594.
- Swartz, S.L., T.R. Shrout, W.A. Schulze and L.E. Cross, 1984. "Dielectric properties of lead-magnesium niobate ceramics," *Journal of the American Ceramic Society* **67**[5], 311-314.

- Takeuchi, H., H. Masuzawa, C. Nakaya and Y. Ito, 1989. "Medical ultrasonic probe using electrostrictive-ceramics/polymer composite," *Proceedings of the IEEE Symposium on Ultrasonics*, 705-708.
- Uchino, K., 1986. "Electrostrictive actuators: materials and applications," *Ceramic Bulletin* **65**[4], 647-652.
- Viehland, D., S.J. Jang, L.E. Cross and M. Wuttig, 1990. "Freezing of the polarization fluctuations in lead magnesium niobate relaxors," *Journal of Applied Physics* **68**[6], 2916-2921.
- Viehland, D., S.J. Jang, L.E. Cross and M. Wuttig, 1991a. "The dielectric relaxation of lead magnesium niobate relaxor ferroelectrics," *Philosophic Magazine B* **64**[3], 335-344.
- Viehland, D., S.J. Jang, L.E. Cross and M. Wuttig, 1991b. "Anelastic relaxation and internal strain in lead magnesium niobate relaxors," *Philosophical Magazine A* **64**[4], 835-849.
- Zhang, Q., W. Pan, A. Bhalla and L.E. Cross, 1989. "Electrostrictive and dielectric response in lead magnesium niobate-lead titanate (0.9PMN:0.1PT) and lead lanthanum zirconate titanate (PLZT 9.5/65/35) under variation of temperature and

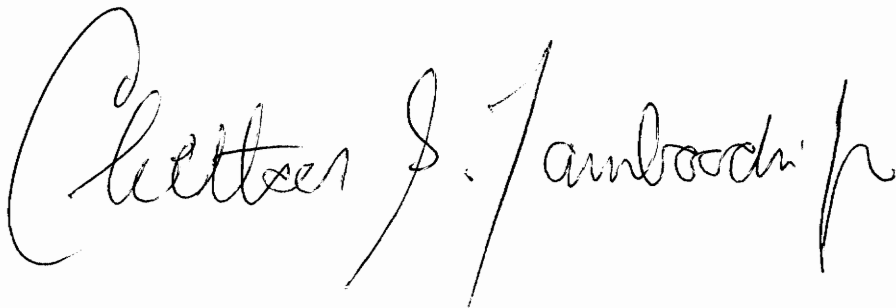
electric field," *Journal of the American Ceramic Society* 72[4], 599-604.

Zhang, Q.M., W.Y. Pan, S.J. Jang and L.E. Cross, 1988. "The pressure dependence of the dielectric response and its relation to the electrostriction," *Ferroelectrics* 88, 147-154.

Zhang, X.D. and C.A. Rogers, 1992. "A macroscopic phenomenological formulation for coupled electromechanical effects in piezoelectricity," *Proceedings of the Conference on Recent Advances in Adaptive and Sensory Materials and their Applications*, Blacksburg, VA, 183-203.

Vita

Chettoor Govindan Namboodri, Jr. was born in Greensboro, North Carolina on November 1, 1968. He grew up in North Augusta, South Carolina and graduated salutatorian from North Augusta High School in 1986. In the fall of that year, he enrolled in Clemson University, South Carolina, where he majored in mechanical engineering. While at Clemson, he participated in the cooperative education program, working five co-op sessions at the Savannah River Site in Aiken, South Carolina, for both E.I. du Pont de Nemours and Company and Westinghouse Savannah River Company. In the fall of 1990, he graduated summa cum laude with a Bachelor of Science in Mechanical Engineering and started graduate work at Virginia Tech in the area of intelligent material systems and structures. He completed his Master of Science degree in the Mechanical Engineering Department during the fall of 1992 and has accepted a position in the Manufacturing Management Program with General Electric Corporation in Salem, Virginia, where he will begin in January of 1993.

A handwritten signature in black ink that reads "Chettoor S. Namboodri Jr." The signature is written in a cursive style with a large initial 'C' and a long, sweeping underline.